



UNIVERSITÀ DEGLI STUDI DI TRIESTE

**XXXIII CICLO DEL DOTTORATO DI RICERCA IN
NANOTECNOLOGIE**

**Development of avalanche photodiodes with engineered
band gap based upon III-V semiconductors**

Settore scientifico-disciplinare: FIS/03 FISICA DELLA MATERIA

**DOTTORANDA
CAMILLA NICHETTI**

**COORDINATORE
PROF. ALBERTO MORGANTE**

**SUPERVISORE DI TESI
DR. GIORGIO BIASIOL**

**CO-SUPERVISORE DI TESI
DR. GIUSEPPE CAUTERO**

ANNO ACCADEMICO 2019/2020

UNIVERSITÀ DEGLI STUDI DI TRIESTE

Department of Physics



Doctoral Programme in Nanotechnology - XXXIII Cycle

DEVELOPMENT OF AVALANCHE
PHOTODIODES WITH ENGINEERED BAND
GAP BASED UPON III-V
SEMICONDUCTORS

Ph.D student

CAMILLA NICHETTI

Supervisor

GIORGIO BIASIOL

Co-supervisors

GIUSEPPE CAUTERO

RALF HENDRIK MENK

MATIAS ANTONELLI

Academic year 2019/2020

Camilla Nichetti: Development of avalanche photodiodes with engineered band gap based upon III-V semiconductors , 2019/2020

Dedicated to my loving parents, Mariella and Alessio.

ABSTRACT

This thesis describes in the development and performance assessment of GaAs/AlGaAs avalanche photodiodes (APDs) with separated absorption and multiplication regions, which complement existing silicon detectors providing higher efficiency for X-ray detection. During the course of this thesis several APDs were fabricated utilizing molecular beam epitaxy and lithography and subsequently have been thoroughly characterized. This thesis is subdivided into six chapters. It starts with a general description of APD structures and their functionalities highlighting the advantages of the developed APDs, which are fabricated on mesas with a diameter of 200 μm and consist of an absorption and multiplication region separated by a thin p-doped layer of carbon. In particular the benefits on impact ionization and charge multiplication when using a superlattice of several (6, 12, 24) nanometric layers of GaAs/AlGaAs hetero-junctions are described, which enhances the charge amplification of electrons while reducing the multiplication of holes thus lowering the overall detector noise. The second chapter deals with device simulation and points out the limitations of the established local model to describe impact ionization in thick multiplication regions. In order to simulate APDs with narrow intrinsic areas a new and improved nonlocal history-dependent model for gain and noise based on the energy balance equation has been developed and is thoroughly described at the end of this chapter. The materials and method section provides in the third chapter a comprehensive description of the techniques and machinery employed during the device manufacturing, while in the fourth chapter the experimental setups, which were utilized to test the devices are outlined. Both, the readout and acquisition electronics and the light/particle sources are thoroughly described. In chapter 5 the different measurements and associated datamining are presented and discussed. In particular the role of different doping levels in the p-doped layers has been investigated revealing that a planar doping with the maximum effective acceptor density is favored as it maximized the potential drop in the multiplication region thus enhancing the impact ionization. Furthermore, measurements and associated results of the time resolution of the APDs utilizing visible table-top lasers and X-rays are described in this section, revealing a rise time of 80 ps for the 24-step device. A study of the noise versus gain behavior is present as well and is compared to the results of the simulation. Moreover, utilizing a charge sensitive amplifier both the spectroscopic capabilities and the charge collection efficiency of the APDs could be determined by means of a

pulsed table-top laser and an Americium source. The thesis finishes with the conclusions in chapter 6.

ABSTRACT

Questo lavoro si occupa di sviluppare e valutare le prestazioni di fotodiodi a valanga basati su GaAs/AlGaAs caratterizzati dall'aver due regioni separate, una di moltiplicazione e una di assorbimento (SAMAPD). Questi sono stati sviluppati per sostituire i rivelatori già esistenti (principalmente realizzati in silicio) nella rilevazione di fotoni di alte energie, quando questi ultimi non sono più efficienti.

Negli ultimi tre anni molti dispositivi sono stati realizzati tramite crescita epitassiale, fabbricati mediante litografia e caratterizzati elettricamente. Nel primo capitolo di questo elaborato viene data una visione generale delle strutture APD e del loro meccanismo di ionizzazione da impatto e vengono spiegati i vantaggi del super reticolo insieme alla descrizione e all'analisi dei nostri dispositivi. I dispositivi cresciuti sono caratterizzati da una regione di moltiplicazione, che contiene un numero specifico di ripetizioni (6,12 e 24) di alcuni strati nanometrici costituiti da eterogiunzioni di GaAs/AlGaAs, separati dalla regione di assorbimento mediante un sottile strato di carbonio drogato p. La regione di moltiplicazione è progettata per migliorare il meccanismo di ionizzazione d'impatto (II) degli elettroni ostacolando la moltiplicazione delle lacune, riducendo così il rumore complessivo del rivelatore. La regione di assorbimento è inserita per avere condizioni ideali di iniezione di elettroni, ovvero facendo in modo che gli elettroni siano gli unici ad entrare nella regione di moltiplicazione. Il secondo capitolo si occupa della simulazione del dispositivo e sottolinea i limiti del modello locale usato per descrivere la ionizzazione da impatto nelle regioni di moltiplicazione spesse. Al fine di simulare gli APD con aree intrinseche strette, è stato sviluppato un nuovo modello non locale per il guadagno e il rumore che dipende anche dalla storia dei portatori di carica, basato sull'equazione del bilancio energetico. La sezione "materiali e metodi" fornisce nel terzo capitolo una descrizione completa delle tecniche e della strumentazione impiegata durante la fabbricazione del dispositivo, mentre nel quarto capitolo vengono descritti i setup sperimentali, che sono stati impiegati per testare i dispositivi. Nel capitolo 5 vengono presentate e discusse le diverse misure. In particolare, il ruolo dei diversi livelli di drogaggio negli strati drogati p è stato studiato a fondo e si è giunti alla conclusione che un drogaggio planare con la massima densità di accettori effettiva è quello da preferirsi in quanto massimizza la caduta di tensione nella regione di moltiplicazione, migliorando così la ionizzazione dell'impatto. Inoltre, in questa sezione vengono descritte le misure e i risultati associati alla risoluzione temporale degli APD,

fatti utilizzando laser visibili da tavolo e raggi X, rivelando un tempo di salita di 80 ps per il dispositivo a 24 gradini. È presente anche uno studio che confronta il rumore in funzione del guadagno con i risultati della simulazione. Inoltre, utilizzando un amplificatore di carica, sia le capacità spettroscopiche che l'efficienza di raccolta della carica degli APD sono state determinate, mediante un laser da tavolo pulsato e una sorgente di americio. La tesi termina con le conclusioni del capitolo 6.

ACKNOWLEDGMENTS

I would like to be able to write those heartbreaking pieces that move so much, unfortunately I do not possess this gift. Thus I will spend the next few lines thanking all the people that have helped and assisted me during these past three years. I would really like to acknowledge so many of them that one thesis would not be enough; but since the thesis is already quite long I will try to be brief.

First of all, I would like to express my special thanks of gratitude to all my colleagues without whom this work could not have been carried out. They have offered assistance when I was in need and supported me when nothing seemed to work. In particular, just to mention some of them: I would not have survived the long days spent in the clean room without Tereza Steinhartova and I could not have performed various tasks without all the insightful advises of Matias Antonelli, who made me laugh so much with his reviews of this work.

I really appreciate and I am grateful for all the discussions and suggestions that Ralf Hendrik Menk, Giorgio Biasiol and Giuseppe Cautero offered me. And I have to thank specially Giuseppe for the opportunity he gave me when asking me to join this project.

Of course, the whole research team that participated to the PRIN project 2015WMZ5C8 has to be thanked: particularly, the collaborators from the University of Udine, Alessandro Pilotto, Pierpaolo Palestri and Francesco Driussi.

Secondly, I have to thank all my friends and family too. They have helped me a lot in finalizing this project. They have been my foothold in moments when some problems seemed impossible to overcome, giving me the strength to move forward. Giulia and Elisa, especially. But many others should be named, making this list quite long.

So since I know that I would forget someone, I sincerely thank everyone who has been by my side, always or just for a short period of time, who has helped me and cared. You know very well who you are anyway.

Camilla

CONTENTS

	INTRODUCTION	xxi
1	AVALANCHE PHOTODIODES	1
1.1	Radiation-matter interaction	1
1.2	Photodiodes	4
1.2.1	p-n junction	4
1.2.2	Avalanche photodiode	6
1.2.3	Heterostructure	8
1.3	General aspects of semiconductor materials	11
1.3.1	III-V compound semiconductors	13
1.4	Basics of Impact-Ionization	15
1.4.1	Drift and Diffusion	15
1.4.2	Generation and Recombination	15
1.4.3	Impact Ionization	16
2	IMPACT IONIZATION MODELS	21
2.1	Local model	21
2.1.1	SNR analysis	26
2.2	Nonlocal models	27
2.2.1	Energy-balance history-dependent model	28
3	MATERIALS AND METHODS	37
3.1	Molecular beam epitaxy	37
3.1.1	MBE building blocks	37
3.1.2	MBE growth process	41
3.1.3	Growth rate calibration	42
3.2	Fabrication techniques	47
3.2.1	Spin coater	47
3.2.2	Litography	47
3.2.3	Etching	49
3.2.4	Metal evaporation	50
3.2.5	Profilometer	51
3.2.6	Bonding machine	51
3.3	Realization of the devices under study	52
3.3.1	Wafer growth	52
3.3.2	Device fabrication	57
4	EXPERIMENTAL SETUP	63
4.1	Light sources	63
4.1.1	Synchrotron radiation	63
4.1.2	Table-top lasers	67
4.1.3	Munich Compact Light Source	70
4.1.4	Americium-241	70
4.2	Readout and acquisition electronics	70
4.2.1	Instrumentation	71
4.2.2	Setups	77

4.3	Virtual Instrumentation	84
5	EXPERIMENTAL RESULTS	87
5.1	EBHDM simulations	87
5.2	Different δ -doping concentrations	89
5.2.1	Dark characteristics	89
5.2.2	Light response	95
5.3	Different number of steps	97
5.3.1	Noise measurements	98
5.3.2	Time response	101
5.3.3	Spectroscopic measurements	103
5.4	X-ray response	106
5.4.1	Soft X-rays	106
5.4.2	Hard X-rays	110
5.5	Americium measurements	114
5.6	Dielectric layer	116
6	CONCLUSIONS	117
I APPENDIX		
A	FORMULA VALIDATION	123
A.1	Local model	123
A.1.1	Derivation of equation 2.2	123
A.1.2	Derivation of equation 2.10	124
A.1.3	Equation 2.16	124
A.2	Non-local model	125
A.2.1	History-dependent with local coefficients	125
B	ROAD TO THE CLEANROOM: TIPS AND TRICKS	131
B.1	Fabrication: a step-by-step description	131
B.1.1	Back side cleaning & polishing	131
B.1.2	Mesa lithography	132
B.1.3	Etching mesa	134
B.1.4	Al ₂ O ₃ layer	134
B.1.5	P-contact metalization	135
B.1.6	N-contact metalization	136
B.1.7	Final structure	136
BIBLIOGRAPHY		137

LIST OF FIGURES

Figure 1.1	Abrupt p - n junction in thermal equilibrium.	5
Figure 1.2	Staircase structure band diagram.	7
Figure 1.3	Energy-band diagram of the superlattice multi-quantum-well APD.	8
Figure 1.4	Staircase structure band diagram.	9
Figure 1.5	Sketch of the structure adopted in this work.	11
Figure 1.6	Partial view of the periodic table regarding semiconductors. The different colors highlight the form the elements take at room temperature: solid, gas and liquid.	12
Figure 1.7	Zinblende structure of GaAs.	13
Figure 1.8	Comparison between transmittance of a bulk region of $4.5\ \mu\text{m}$ and attenuation length of GaAs and Si.	13
Figure 1.9	Bandgap energy and wavelength versus lattice constant are represented.	14
Figure 1.10	Electron drift velocity-field referring to some intrinsic semiconductor materials.	16
Figure 1.11	Impact ionization caused by a photon.	17
Figure 1.12	The photocurrent induced in a photodetector circuit comprises the superposition of current pulses, differently multiplied, each associated with a detected photon. The illustrated individual pulses are decaying step functions. Their superposition constitutes the shot noise.	19
Figure 2.1		22
Figure 2.2	Schematic for the spatial notation used for holes and electrons.	29
Figure 2.3	Spatial discretization of the variables N_e and N_h and indication of the boundary conditions (in red).	33
Figure 3.1	Schematic drawing of a generic MBE system.	37
Figure 3.2	Schematic of an effusion cell.	38
Figure 3.3	High Mobility MBE at IOM-CNR at Trieste.	41
Figure 3.4	Schematic representation of the origin of RHEED diffraction patterns. The intersections of the Ewald sphere with the features of the reciprocal lattice define diffracted spots and streaks visualized on the fluorescent screen.	44

- Figure 3.5 2x and 4x diffraction patterns from a (2x4)-reconstructed (001) GaAs surface. 44
- Figure 3.6 Growth mechanism with corresponding RHEED intensity oscillations as a function of growth time. The periodic variation of concentration of surface steps influences the intensity of the oscillations. In fact, the steps behave as scattering centers for incident electrons 45
- Figure 3.7 A reflectivity measurement with two different wavelengths for thickness control ($\lambda_1 = 950$ nm and $\lambda_2 = 470$ nm) as a function of the time in seconds. 46
- Figure 3.8 Schematic representation of a generalized positive and negative resist process: exposure, development, and pattern transfer. Positive resists develop in the exposed region. Negative resists remain in the exposed region. 48
- Figure 3.9 Lift-off process. 48
- Figure 3.10 Schematic of an e-beam evaporator. 51
- Figure 3.11 Wire bonding. 52
- Figure 3.12 Sketch of the fabricated avalanche photodiode with separated absorption and multiplication regions. Scheme of the structure grown by MBE. Band diagram under reverse bias. 53
- Figure 3.13 Aluminum concentration profile of a portion of the staircase structure and detail of a single step. 54
- Figure 3.14 XRD spectra of a SAM-APD structure grown on a (001) GaAs n-doped substrate having a multiplication region of 12 steps. 55
- Figure 3.15 The structure utilized to calibrate the p-doping density and the C acceptor density as a function of the 2D-density of carbon deposited atoms. 56
- Figure 3.16 The main steps performed during fabrication. 57
- Figure 3.17 Pictures of the different utilized dielectric layers. 59
- Figure 3.18 Masks used to define the p-contact. 60
- Figure 3.19 Bonded devices on the dedicated PCB, and a detail of such bond. 61
- Figure 4.1 Schematic representations of a synchrotron radiation facility: its planar vision and the view of its storage ring, where some of its main elements are visible. 63
- Figure 4.2 Illustration of the BEAR beamline arrangement. 64

Figure 4.3	Photon flux as a function of the photon energy for different gratings; and the bandwidth and photon flux as a function of the slit width, measured at 867 eV. 66	66
Figure 4.4	Illustration of the XRD2 beamline arrangement. 66	66
Figure 4.5	Optical scheme of the TwinMic beamline. 67	67
Figure 4.6	Elements that can be studied with the energies available at TwinMic. 68	68
Figure 4.7	Absorption coefficient of GaAs versus photon energy from 1 eV to 25 eV. 68	68
Figure 4.8	Oscillator and amplifier scheme for the ytterbium-doped fiber laser, built at the Laser Laboratory situated at Elettra-Sincrotrone in Trieste. 69	69
Figure 4.9	Front and back side of the PCB board where the devices must be accommodated in order to perform the measurements. 71	71
Figure 4.10	First prototype of a transimpedance amplifier using a LTC6268 and the preamplifier prototype on the basis of an OPA656. 73	73
Figure 4.11	TIA circuit. 74	74
Figure 4.12	Linear-region equivalent circuit. 75	75
Figure 4.13	TIA's equivalent circuits with independent noise sources. 75	75
Figure 4.14	Upper-side of the PCB dedicated to the placement of the CUBE and actual bonded CUBE. 77	77
Figure 4.15	PIT wideband amplifier and its gain up to 4 GHz. 78	78
Figure 4.16	Views of the laser setup. 78	78
Figure 4.17	Noise setup. 79	79
Figure 4.18	Noises detected with the spectrum analyzer. 80	80
Figure 4.19	Block diagram of the setup for the spectroscopic measurements. 81	81
Figure 4.20	Some elements positioned at the XRD2 beamline. 81	81
Figure 4.21	Some elements positioned at the CiPo beamline. 82	82
Figure 4.22	Design and illustrative photo of the PCB prepared to interface the sample holder used in the BEAR beamline and the one where the devices are glued to read their signals. 83	83
Figure 4.23	Device holder built ad-hoc for the TwinMic beamline (in black) where the PCB is embedded. 84	84
Figure 4.24	Am setup. 84	84

- Figure 4.25 Main panel of the virtual instrument developed in LabVIEW to control the electronics to perform IV scans. 85
- Figure 5.1 Band diagram of the multiplication region of our device when a bias of 0 V is applied; and comparison between experimental and simulated CV characteristics of the staircase SAM-APD. 87
- Figure 5.2 Simulated and measured gain versus voltage and excess noise factor versus gain for the staircase APD. 88
- Figure 5.3 Dark current density value for a device of the E type. 90
- Figure 5.4 Capacitance and corresponding depletion width versus reverse bias for different devices. 90
- Figure 5.5 Comparison between experimental and simulated CV curves for devices characterized by different concentrations of carbon in the separation layer between the absorption and multiplication region. 91
- Figure 5.6 Conduction band diagrams of devices A, C, E and F for 5 different reverse biases. 92
- Figure 5.7 Experimental CV characteristics of samples with a δ separation layer with a planar acceptor density of $2.5 \cdot 10^{12} \text{ cm}^{-2}$ and a 50-nm separation layer with a planar acceptor density of $6.0 \cdot 10^{12} \text{ cm}^{-2}$; and the respective depletion widths. 93
- Figure 5.8 Dopant concentration as function of depletion width for different devices. 94
- Figure 5.9 Gains of devices with different areal density of the δ p-layer measured at the BEAR beamline averaged over seven different energies in the 500-800 eV range, and with the green laser. 95
- Figure 5.10 Currents for device E and F as a function of the applied reverse bias. 96
- Figure 5.11 A detail of the simulated conduction band profile of the SAM-APD structure taken in the surroundings of the layer which separates the absorption and multiplication regions at different biases. 97
- Figure 5.12 Simulation of the gain as a function of the reverse bias and the excess noise factor as a function of the gain for devices characterized by 6, 12, 24 and 48 steps. 98

- Figure 5.13 Measured capacitance and depletion width as a function of the reverse bias for devices with 6, 12 and 24 steps. 98
- Figure 5.14 Gain as a function of the bias for devices characterized by different number of steps. 99
- Figure 5.15 Excess noise factor as a function of the gain for devices characterized by a different number of steps: 6, 12 and 24. 100
- Figure 5.16 Time response of devices characterized by 6, 12, 24 steps. 102
- Figure 5.17 Gain as a function of the reverse bias, extrapolated from the areas under the time waveforms. 103
- Figure 5.18 Examples of a few signals acquired before the shaper with a 6-step device for different biases. 104
- Figure 5.19 Histograms of the area of the pulses resulting from the shaper, normalized both in area and frequency to highlight the variation of the standard deviation, for devices with 6, 12 and 24 steps, respectively. 104
- Figure 5.20 Gain as a function of the reverse bias extrapolated from the area under the acquired shaper responses for devices with different number of steps. 105
- Figure 5.21 Fluorescence maps: distribution of particular materials across our device. 107
- Figure 5.22 Current maps acquired at different biases with an energy beam of 1500 eV. 108
- Figure 5.23 Attenuation length as a function of the photon energy for a GaAs bulk. 109
- Figure 5.24 Dark current and photocurrent for three photon energies of the BEAR beamline in the 500-800 eV range of an E-type device; and corresponding gains for the same photon energies. 109
- Figure 5.25 Current maps at 5 V and 31 V for the device with a mesa diameter of 600 μm . 110
- Figure 5.26 Measurements performed in air with a hard X-ray beam. 111
- Figure 5.27 Dark gap detail of a time trace acquired at the XRD2 beamline by the oscilloscope. 112
- Figure 5.28 Time traces acquired at the XRD2 beamline by the oscilloscope for different bias voltages. 113
- Figure 5.29 Gain and noise as a function of the bias for a device with 24 steps under a 15-keV beam provided by the MuCLS. 114

Figure 5.30	Examples of some signals generated by an americium alpha particle impinging on a 12-step detector, biased at 40 V. 114
Figure 5.31	Mean value trend of the the step as a function of the bias for devices characterized by 6, 12 and 24 steps by using a laser and by using the ^{241}Am radioactive source. 115
Figure 5.32	Horizontal scan revealing the overlap of metal electrodes and silicon oxide. 116
Figure B.1	Structures grown on wafers. 131
Figure B.2	Sample equipped with a protecting layer prior to removal of the Ga glue. 132
Figure B.3	Mesa lithography steps. 133
Figure B.4	Example of two masks. 133
Figure B.5	Results of the etching of the mesa. 134
Figure B.6	Al_2O_3 deposition steps. 135
Figure B.7	P-contact metalization. 136
Figure B.8	Bottom n-metalization. 136
Figure B.9	Final structure. 136

LIST OF TABLES

Table 1.1	Properties of GaAs and Si. 12
Table 3.1	Layers of the SAM-APD structure from which the devices were fabricated. 53
Table 4.1	BEAR monochromator characteristics. 65
Table 5.1	Acceptor densities for the p-doped layer, measured with Hall effect. 89
Table 5.2	Summary of the maximum gain obtained using different sources and setups for devices characterized by different numbers of steps. 105
Table B.1	Polishing recipe. 132

INTRODUCTION

Recently commissioned Free-Electron Lasers (FELs) and 4th-generation Synchrotron Radiation (SR) sources have opened new research possibilities by providing extremely short pulses of extremely bright and coherent radiation, even at high X-ray energies. On the experimental side this has led to an increasing demand for very fast detectors able to detect hard-X-rays. Nowadays, the most mature technologies for the production of photon detectors are based on silicon and, as a result, different Si devices are widely employed for the detection over a broad range of photon energies. They give optimal results at low energies and up to now they have been quite adequate in terms of the required performances; however, they are rather inefficient at detecting photons in the hard-X-ray region, where they may also experience some severe issues due to radiation hardness.

Over time, in order to fulfill the more stringent requirements the advent of next-generation light sources imposed, other materials have been researched to replace silicon, such as CdTe or other compound semiconductors. Our attention is directed to the latter ones and in particular to Avalanche PhotoDiodes (APDs) based on compound semiconductors, as according to the literature they possess some promising properties (e.g. [1, 2]).

Photodiodes are electronic devices which collect photons and generate an electronically measurable signal. Generally speaking, when a photon hits them, it creates electron and hole pairs; these carriers are separated by an electric field (in most of the cases of our interest, generated by applying a reverse bias to the diode) resulting in an electric current inside the device. In particular, APDs are designed to capture extremely low photon fluxes; when they are reverse biased near the breakdown voltage, impact ionization occurs and such mechanism is used to amplify the signal obtaining high gains without adding excessive additional noise, proving, in some conditions, an improvement with respect to external electrical amplification of extremely low photogenerated charge.

Compound-semiconductor APDs (e.g. based on GaAs/AlGaAs hetero-junctions) possess some advantages compared to those based on Si. In particular, the high atomic number of GaAs makes its absorption coefficient much higher than that of Si [3]. Consequently, the absorption length of GaAs for energies higher than 11 keV is significantly shorter and this allows the device to be thinner [4]. This, combined with larger electron mobility, translates into shorter response times. However, to obtain low noise APD, it is essential that the material have very different electron and hole ionization coefficients (α and β ,

respectively) [1]. The ratio between the two is greater than 20 in Si, while in III-V compound semiconductors it is approximately equal to 1 because the two coefficients are comparable.

To solve this problem, superlattice structures consisting of nanometre thick alternating layers have been proposed in literature. This possibility exploits the so-called “band gap engineering” techniques, which allow the synthesis of multilayers with different composition, and thus the modulation of the semiconductor band gap energy at the sub-nm level. Particularly the pattern that we plan to analyze is a “staircase” structure: it is a region, a few nm thick, of $\text{Al}_x\text{Ga}_{1-x}\text{As}$ with x variable from $x = 0$ to x_{max} , which is repeated for N periods. This would allow minimizing the multiplication noise [5].

The theoretical basis upon which these observations rely was developed in the literature by Capasso [5], where it has been highlighted that with suitable structures, epitaxially grown from materials with calibrated doping and molar fractions, it is possible to obtain a substantial gain keeping the signal-to-noise ratio (SNR) high. The above-mentioned structure is made of conduction bands which provide energy to moving electrons and valence band discontinuities that subtract energy from moving holes. It could be erroneously thought that by increasing the number of electrons and holes equally it is possible to achieve better performances; conversely, to obtain such result the electrons responsible for the current must be the majority carrier with respect to the holes [6] and this aspect will be thoroughly analyzed in the thesis.

Although these structures have been proposed and implemented for years, for both fiber optic communications and X-ray detection, some aspects of their realization can be further investigated, and their performances can still be improved. With this in mind, the development of new numerical models is essential for their optimization in terms of various parameters, e.g. noise. Furthermore, an extensive experimental characterization by means of synchrotron and conventional light sources renders it possible to obtain more controlled and reproducible results (e.g. monochromatic SR is characterized by high fluxes with precise energies) and to be able to provide devices as required by the market. This is the reason why the work conducted for this thesis is part of a larger project of national interest (PRIN) for the development of new detectors. The PRIN, called “Rivelatori di raggi X in semiconduttori ad alto numero atomico per sorgenti di nuova generazione e *imaging* medicale”¹ was carried on by several research groups and it is a collaboration between Elettra - Sincrotrone Trieste, CNR-IOM, the University of Udine and the University of Trieste.

The thesis consists of six chapters structured as follows.

¹ *X-ray detectors based on high atomic number semiconductor for next generation light sources and medical imaging.*

THE FIRST CHAPTER offers an overview of the APD structures and their mechanism of impact ionization; it explains the advantages of the superlattice together with the description and analysis of our devices.

THE SECOND CHAPTER provides an overview of the models used to simulate the devices illustrated in the first chapter. It presents the local model and the nonlocal ones. The former was used in the past to describe impact ionization in thick multiplication regions. However, it is inadequate when dealing with photodiodes with narrow intrinsic areas as the one depicted in chapter one. For this reason, an improved nonlocal history-dependent model for gain and noise in APDs based on the energy balance equation was introduced.

THE THIRD CHAPTER is focused on the materials and methods used. It is a comprehensive description of the techniques employed during the manufacturing and the machines utilized for the fabrication.

THE FOURTH CHAPTER outlines the experimental setups which were involved to test the devices. It is divided mainly in two subsections, the first one highlighting the used light sources and the second one describing the readout and acquisition electronics.

THE FIFTH CHAPTER describes the measurements which have been carried out, analyzing in detail the experimental results from different points of view.

THE SIXTH CHAPTER summarizes the activities carried out and the results achieved in the three year duration of my PhD.

AVALANCHE PHOTODIODES

A direct conversion photodetector is a device whose electrical characteristics vary when it is exposed to light. By converting the energy of the absorbed photons into a measurable form, it can be used to determine some quantity related to the incident photon beam [7]. The absorption of photons which impinge on it causes the creation of positive and negative charge carriers. Under the effect of an electric field these charge carriers separate and drift, producing a measurable current. Some photodetectors also incorporate an internal gain mechanism so that the photocurrent is amplified thanks to a cascade process (impact ionization), thereby rendering the signal more easily detectable. This becomes very useful, especially when the number of photons to detect is very low and would produce a signal comparable or lower than the noise of the readout system. A weak light is then able to produce a current that is large enough to be readily detected by the electronics following the device. However, the multiplication process requires time and introduces gain noise, which limits the system bandwidth and performance. Chapter 1 will present some concepts to better understand this subject and it will introduce some types of photodiodes, the materials used, and their general properties, including the description of the adopted staircase structure and its characteristics.

1.1 RADIATION-MATTER INTERACTION

Already in the 18th century it was shown by macroscopic observations of Lambert and Beer that the attenuation of visible light is connected to the material properties through which the light is traveling [8].

Assuming a monochromatic wave field traveling in the x direction which impinges perpendicularly onto a material sample, the radiant intensity at some distance is reduced of a certain quantity $dI'(x)$, compared to the intensity I' that entered, expressed by

$$dI' = -\mu \cdot I' \cdot dx' \quad (1.1)$$

where μ is the linear attenuation coefficient, whose numerical value is material dependent and describes the fraction of X-rays beam that is absorbed or scattered per unit thickness of the absorber. A scattered photon might still reach the detector or generate a fluorescent photon that reaches the detector especially for high energy photons. Equation 1.1 is a homogeneous differential equation of first order,

which can be solved by separation of variables and subsequent partial integration

$$\int_{I_0}^I \frac{dI'}{I'} = \ln(I) - \ln(I_0) = \ln\left(\frac{I}{I_0}\right) = - \int_0^z \mu(x') \cdot dx' \quad (1.2)$$

leading to what nowadays is called the Lambert - Beer law:

$$I(x) = I_0 \cdot e^{-\int_0^x \mu(x') dx'}. \quad (1.3)$$

If the material distribution $\mu(x)$ along the path of the light is known, the line integral in the exponent can be calculated [8].

Assuming, instead, that the electromagnetic field emitted by a physical source is never strictly monochromatic, it is possible to divide in K discrete energy steps ΔE the spectral distribution $P(E_\gamma)$ of the incident X-rays. For each energy, a certain incident radiation I_i can be identified ($I_0(E_\gamma) = P(E_\gamma) \cdot \Delta E$). Then equation 1.3 can be written as

$$I(x, E_\gamma) = \sum_{\gamma=1}^K P(E_\gamma) \cdot e^{-\int_0^x \mu(x, E_\gamma) \cdot \Delta E} \quad (1.4)$$

considering that μ varies also with the X-ray energy and E_γ is the incident wave energy.

The above mentioned two equations (eq. 1.3 and 1.4) can be further generalized thinking in addition to the integration over all energies, also to the discrete distribution of N different elements in the sample as

$$I(x, E_\gamma) = \sum_{\gamma=1}^K P(E_\gamma) \cdot e^{-\sum_{i=0}^N \mu(\Delta x_i, E_\gamma) \cdot \Delta x_i} \cdot \Delta E \quad (1.5)$$

where $\mu(E_\gamma, \Delta x_i)$ are known for arbitrary chemical elements and X-ray energies.

To study the propagation of a wave we need to consider not only the macroscopic effects but also the microscopic ones. Defining the mass attenuation coefficient as $\frac{\mu}{\rho}$, where μ is the attenuation coefficient and ρ is the mass density, we can express microscopically the total mass absorption coefficient in terms of sum of atomic cross sections $\sigma = \sum_i \sigma_i$ as

$$\frac{\mu}{\rho} = \frac{N_A}{m_a} \cdot \sigma = \frac{N_A}{m_a} \cdot \sum_i \sigma_i \quad (1.6)$$

where m_a is the atomic molar mass in g mol^{-1} and N_A is Avogadro's number.

The cross section is the probability that an interaction of an incident wave field or particle beam and the target object consisting of discrete particle happens. The interaction can happen with or without energy transfer, denoted as resonant and non-resonant process.

In the energy range of X-rays discussed in this thesis (from some keV to some 10 keV) the dominant non-resonant effects are Thomson scattering and coherent scattering, respectively, while the resonant process is mainly given by the Compton scattering and the photoelectric effect.

Thomson in 1906 described the interaction between a long wavelength wave and weakly bound electrons, known as Thomson scattering effect, which results in the electrons accelerated along the polarization of the wave and being the sources of spherical waves that propagate with the same frequency as the incident wave. The cross section of this event (Thomson cross section, $\sigma_{Th} = 0.665 \cdot 10^{-24}$) is independent from λ , thus the scattering of electromagnetic waves on weakly bound electrons is the same for each wavelength, considering that the photon momentum can be neglected.

Thomson scattering

In case of coherent scattering (Rayleigh scattering) a wave characterized by a certain frequency f_0 interacts instead with bound electrons, bound to the nucleus via a spring with frequency f_a . Assuming $f_0 \ll f_a$ the cross section results in

Coherent scattering

$$\sigma_{Ra} = \sigma_{Th} \cdot \left(\frac{f_0}{f_a}\right)^4 \quad (1.7)$$

which depends on the inverse fourth power of the wavelength of the incident radiation [8].

For higher X-ray energies, the photon-electron interaction considers both momentum and energy conservation. During the Compton scattering the photon is scattered by a weakly bound electron to which transmit its momentum and energy. Thus the electron will gain certain kinetic energy as the wavelength increases and its direction changes. Considering energy way lower than 511 keV, the Compton cross section is

Compton scattering

$$\sigma_{Co} = Z \cdot \sigma_{Th} \cdot \left(1 - \frac{E_\gamma}{mc^2}\right) \quad (1.8)$$

where E_γ is the energy of the incident photon, m is the mass of the electron, c is the speed of light and Z is the atomic number. The cross-section is multiplied by Z as there are Z electrons that can be potentially scattered. Equation 1.8 shows how the Compton cross-section decreases with the photon energy while it increases with the atomic number of the target, and it does that linearly [8].

The photoelectric effect consists in the absorption of an incident photon and then the transfer of all its energy to a bound electron. This happens if the energy of an incident photon is greater than the binding energy of a bound electron. Due to the energy conservation the difference between the photon energy and the binding energy is transformed into kinetic energy while the photon annihilates. For hydrogen like atoms the cross section of this effect is given by

Photoelectric effect

$$\sigma_{PE} = \sqrt{\frac{32}{\epsilon^7}} \cdot \alpha^4 \cdot Z^5 \cdot \sigma_{Th} \quad (1.9)$$

where $\varepsilon = m \cdot c^2 / (\hbar \cdot \omega)$, $\alpha = e^2 / (\hbar \cdot c)$ is the fine structure constant, Z is the atomic number and σ_{Th} is the Thomson cross-section.

The Z^5 dependency implies that high Z materials absorb X-rays much better than light materials, since the cross-section is coupled with the mass absorption coefficient (eq. 1.6) and this explains why materials such as GaAs are used in direct conversion X-ray detectors [8].

1.2 PHOTODIODES

This section introduces the basics of the avalanche photodiode structure. The p-n and p-i-n junctions will be briefly explained and discussed and their application as photodiodes will be presented. Moreover, the staircase structure, which is the structure mainly used in this work, will be described and shown.

The p-n junction is of great importance in understanding the semiconductor devices as it serves to explain in a simplified way the basics of the physics underneath them.

P-i-n junctions, on the other hand, are very similar to p-n but they have a larger depletion region which increases the photodetector sensitivity. And last, there are the avalanche photodiodes, which are similar to the above-mentioned devices except that the bias applied is sufficiently large to cause impact ionization.

1.2.1 p-n junction

A p-n junction is a homojunction between a p-type and an n-type semiconductor crystal. These two sections are characterized by an abundance of the majority carriers, holes and electrons, respectively. The other carriers, which are present in the sections, are called minority carriers [7].

As soon as these two sections are put in contact, electrons and holes diffuse from areas where they are in high concentration toward areas of low concentration, owing to the the large density gradient. As these carriers move into oppositely doped material, they leave behind uncompensated dopant atoms near the junction, causing an electric field. As a result, this creates a potential barrier (V_{bi} , Fig. 1.1c) so that the process cannot continue indefinitely. At a certain point (at thermal equilibrium) a space charge region forms between the two types of material. Essentially this region is depleted of any charge and thus is called depletion region (Fig. 1.1a).

By imposing equilibrium conditions and the Boltzmann statistics, the built-in voltage V_{bi} can be extrapolated as a function of the doping and of the intrinsic semiconductor concentration [10], namely

$$V_{bi} = \frac{k_B T}{q} \log\left(\frac{N_A N_D}{n_i^2}\right) \quad (1.10)$$

where N_A and N_D are not the donor acceptor impurity concentrations but rather the net donor and acceptor concentrations in the individual n and p regions, respectively, k_B is the Boltzman constant, T is the working temperature, q is the elementary charge, and n_i is the intrinsic carrier concentration [11].

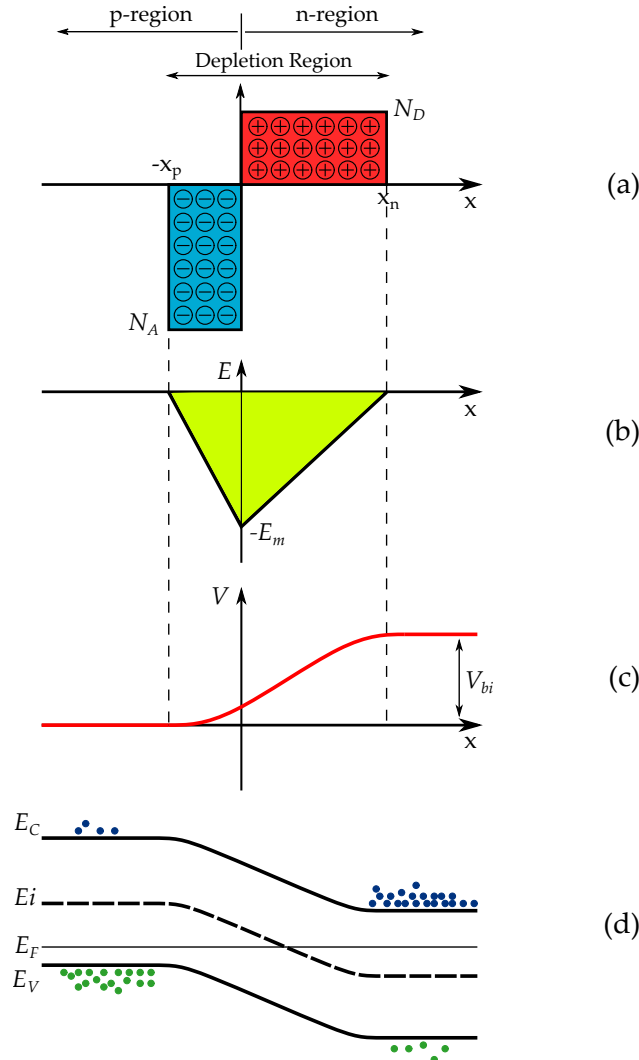


Figure 1.1: Abrupt p - n junction in thermal equilibrium. (a) Space charge distribution. (b) Electric-field distribution. (c) Potential distribution where V_{bi} is the built-in potential. (d) Energy-band diagram.[9]

At thermal equilibrium, the energy-band diagram is as shown in Fig. 1.1d, where the Fermi energy level is constant throughout the entire system. The built-in potential barrier maintains the equilibrium between the majority and minority carriers in the two regions and thus no current is produced by this voltage.

So, an electric field is formed in the depletion region by the separation of the negative and positive space charge densities (Fig. 1.1a, assuming an abrupt junction). Solving the Poisson equation, it is pos-

sible to evaluate the potential in the junction, as function of the spatial coordinate x , by integrating the electric field as

$$\phi(x) = - \int E(x)dx \quad (1.11)$$

which is reported in Fig. 1.1b.

The solution of the Poisson equation in the presence of an external applied bias V_A leads to the following expression of the total depletion width [11]:

$$W = \sqrt{\frac{2\varepsilon(V_{bi} - V_A)}{qN_{eq}}} \quad (1.12)$$

where $N_{eq} = N_D^{-1} + N_A^{-1}$. The total depletion width increases with increasing the reverse applied voltage and it is limited by the magnitude of the existing dopant concentrations of the two sides of the junction (the higher the dopant concentration, the narrower the space-charge region inside a given region).

1.2.1.1 Junction Capacitance

Since we have a separation between positive and negative charge in the depletion region, a capacitance, which depends from the bias V , can be associated to the junction. By using this capacitance, it is also possible to calculate the width of the depletion layer of the diodes as a function of the applied voltage as

$$W = \frac{\varepsilon_r \varepsilon_0 A}{C(V)} \quad (1.13)$$

where A is the area of the device, $C(V)$ is the depletion-layer capacitance at a bias V , ε_r and $\varepsilon_0 = 8.854 \cdot 10^{-12}$ F/m are the equivalent relative permittivity of the material and the permittivity of vacuum, respectively.

Moreover, starting from this depletion-layer capacitance we can calculate the nonuniform doping profile $N(W)$, by using the equation for general nonuniform distributions [9]:

$$\frac{d(1/C_A^2)}{dV} = \frac{2}{q\varepsilon_r \varepsilon_0 N(W)} \quad (1.14)$$

where C_A is the capacitance per unit area of the mesa, V is the applied bias, q is the elementary charge and W is the depletion width.

This method will be used in Ch. 5 to analyze the δ profile of the the structure described in section 1.2.3 .

1.2.2 Avalanche photodiode

Avalanche photodiodes (APDs), as the name suggests, exploit the avalanche multiplication of the photogenerated carriers. This is done

through the mechanism (described in Section 1.4.3) called impact ionization, which amplifies the current generated inside the detector, improving the device sensitivity. In an APD we can distinguish two regions: the generation region and the multiplication region. These two regions can be physically the same, as it is in the p-i-n, or they can be separated, as in the separated absorption and multiplication APD (SAM-APD).

The structure of a conventional APD is a p-i-n diode (Fig. 1.2a) under reverse bias conditions, with negligible minority carrier diffusion currents at the edges of the depletion region [11]. A p-i-n junction is similar to a p-n one with the only difference that an intrinsic region interposes between the two highly doped ones. This is done in order to have a large, completely-depleted layer under reverse bias conditions characterized by an almost constant electric field [11]. However, a higher noise is also associated with the larger photocurrent produced inside this device.

To overcome this problem, SAM-APDs (Fig. 1.2b) can be used. In these structures the whole primary photocurrent is injected entirely at the edge of the avalanche region, whereas in conventional APDs the photocurrent injection takes place only gradually within the avalanche region that act as absorption region increasing the noise [11]. As mentioned, in this structure the photon is absorbed in a different place to where electrons and holes are multiplied. Moreover, optimum noise and speed can be achieved if the process of creating the carriers is unipolar (meaning that just electrons or holes undergo impact ionization). In fact, as said in Section 1.4.3 when the ionization coefficients are similar the noise increases and the speed is reduced. So, if the ionization coefficient of the avalanche-triggering carrier is much larger than the other one less noise is generated. This condition is met naturally for some materials, for instance in Si, but can also be artificially achieved by bandgap engineering as in heterostructures.

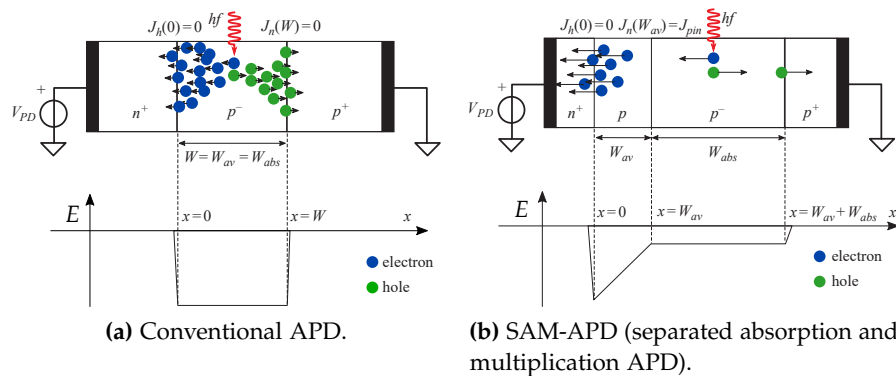


Figure 1.2: Structure and electric field profile of a conventional APD and a separated absorption and multiplication one [11]. W_{av} is the multiplication region and W_{abs} is the generation one (where the electron-hole pairs are created).

1.2.3 Heterostructure

Heterostructures are semiconductor structures in which the chemical composition changes with position creating heterojunctions (interfaces where traps and lattice mismatch play a negligible role). They are important because they are able to improve the overall performances of the semiconductor devices by modifying locally the energy band structure and thus offering control over the motion of the charge carriers [12]. Examples of heterostructure are the superlattice structures known as multi-quantum-well [13] and the staircase structure [5] proposed by Capasso.

Superlattice structure

The staircase structure, so called because of its band diagram similar to a staircase, is one of the most common super-lattice structures [14] and it is an evolution of multi-quantum-wells. The concept on which it relies is the imposition of specific band discontinuities between the conduction and the valence band, in order to provide energy to the moving electrons and to make the hole impact ionization less probable. Between the interfaces of the different layers a difference in energy is created: ΔE_c in the conduction band and ΔE_v in the valence one.

Multi-quantum-well

In the specific case of a simple super-lattice composed of alternating layers of $\text{Al}_{0.45}\text{Ga}_{0.55}\text{As}$ and GaAs the band diagram is shown in Fig. 1.3. Here the discontinuities are equal to 0.48 eV and 0.08 eV, ΔE_c and ΔE_v respectively [13].

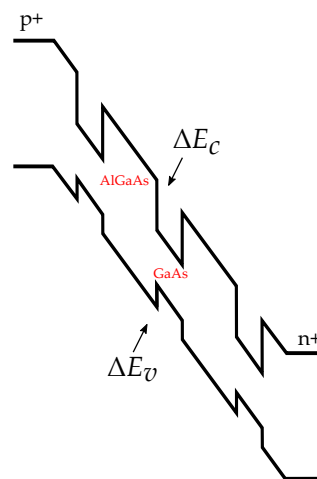


Figure 1.3: Energy-band diagram of the superlattice multi-quantum-well APD [13].

It was demonstrated experimentally that in this multi-quantum-well structure, the effective impact ionization rates for electrons and holes are different ($k \simeq 10$, where k is the ratio between the electron and hole impact ionization coefficients), although this is not the case for the bulk material where they are comparable ($k \simeq 1$).

What happens is that an electron accelerating in an AlGaAs barrier enters the GaAs abruptly and gains an energy equal to the conduction band energy discontinuity over a smaller distance than the phonon scattering mean free path, so that the average distance to reach the ionization threshold is reduced and thus α enhanced. Since ΔE_c is greater than ΔE_v , electrons have a higher kinetic energy compared to holes and so they are much more likely to undergo impact ionization; and since only one component is multiplied, only this one adds to the noise generated in the structure [14].

However, even if carriers are strongly accelerated by the field, it is not certain that an electron will ionize at each step. Moreover, to enhance the electron ionization it is desirable to maximize ΔE_c , but this may lead electrons to be trapped in the wells. To overcome this problem compositionally graded regions may be introduced as is done for the staircase structure.

The multistage graded-gap structure, known as staircase structure, is based on the same principle; however, here the electron ionization energy is entirely provided by conduction-band steps [14]. Figure 1.4a shows the energy-band diagram of the graded-gap multilayer material when a zero bias is applied. Each stage goes from a specific energy gap (E_{g1}) to an higher one (E_{g2}) over a certain distance l , where an abrupt step lowers again the energy to the starting point. Instead, Figure 1.4b shows the same structure when a bias is applied: here the conduction band gives a higher kinetic energy to the electrons, which flow towards the anode increasing their ionization rate; conversely, the steps in the valence band are quite small and the holes will gain less kinetic energy and will less likely undergo ionization. Because only electrons cause ionization, the device resembles a photomultiplier [14].

Staircase

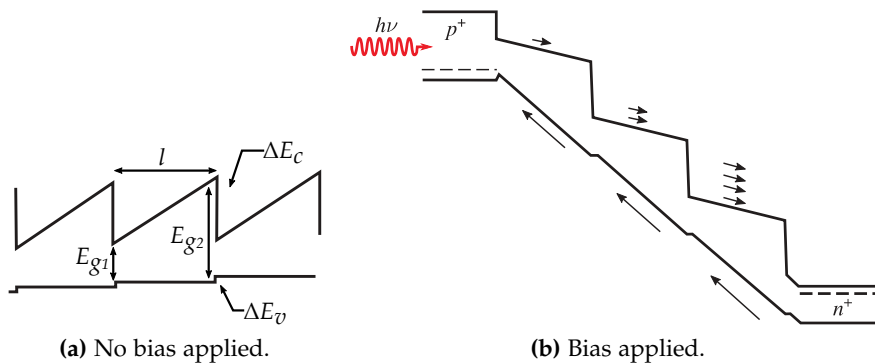


Figure 1.4: Staircase structure band diagram [5].

Under the combination of the bias field E and the grading field $\Delta E_c/ql$, the electron drifts toward the conduction band discontinuity. After the step the electron has sufficient energy to impact ionize because $\Delta E_c \approx E_{ie}$, where E_{ie} is the electron ionization energy [14].

In staircase APDs impact ionization occurs just in the immediate vicinity of the conduction band discontinuity. This provides a deterministic behavior because if the step is quite high, then all the electrons should multiply by a factor of 2, which means each electron ionizes once after each step, without having some statistical variability in the multiplication process. However, this is not what happens in reality: if we define δ as the fraction of electrons, which does not undergo impact ionization, it results that the total gain of the structure is

$$M = (2 - \delta)^N \quad (1.15)$$

where N is the number of stages in the staircase structure; and the excess noise factor can be expressed as

$$F = 1 + \frac{\delta[1 - (2 - \delta)^{-N}]}{2 - \delta} \quad (1.16)$$

so, if the majority of carriers ionize at each step then F is almost equal to 1 and it becomes independent of the number of stages which form the structure, implying that the process is almost noiseless for high gains [14]; this is why we develop and use this superlattice structure.

Developed device

The structure just mentioned is also the one adopted in this work. It uses nanometric-size alternating layers of semiconductors, mostly GaAs and AlGaAs. The devices under investigation were grown epitaxially onto GaAs wafers by using molecular beam epitaxy (MBE) techniques accordingly to Table 3.1.

A sketch of such a device is shown schematically in Fig. 1.5. After the deposition of a 100-nm-thick highly n-doped ($2 \cdot 10^{18} \text{ cm}^{-3}$) buffer layer onto a (001) n-substrate, an intrinsic multiplication layer was grown, following the protocol described in Appendix B (the related employed techniques are described in Ch. 3). The next layer includes a staircase structure with a given number of stages (repetitions) and it represents the multiplication region. Each stage consists of 35 nm of GaAs, 25 nm of $\text{Al}_{0.45}\text{Ga}_{0.55}\text{As}$ and 20 nm of a linearly graded region where the aluminum content is reduced linearly from 45% to 0%. The initial percentage of aluminum is chosen in order to maximize the energy potential drop electrons undergo each step of the staircase, while still keeping a direct bandgap. The layers' dimensions, instead, were selected considering that the electrons usually impact ionize after a distance the order of a few times the mean free path, which is typically 5-10 nm in most III-V semiconductor [5]. Such widths were suggested in [4]. Above the staircase structure, a 35-nm-thick GaAs spacer was grown, followed by a δ p-doped layer (2D sheet) of carbon atoms characterized by a concentration of $2.5 \cdot 10^{12} \text{ cm}^{-2}$. Such a layer ensures that after applying a reverse bias the vast majority of the potential drops in the multiplication region. On the top of the

δ layer, the intrinsic GaAs absorption layer was deposited. Finally, the sample was capped with a 150-nm highly p-doped ($6 \cdot 10^{18} \text{ cm}^{-3}$) GaAs contact layer. The overall thickness of the active part depends both on the thickness of the absorption layer and the number of repetitions in the multiplication region.

At the end of the fabrication process, most of the structures feature a mesa of $200 \mu\text{m}$ and an opening of $150 \mu\text{m}$ in diameter.

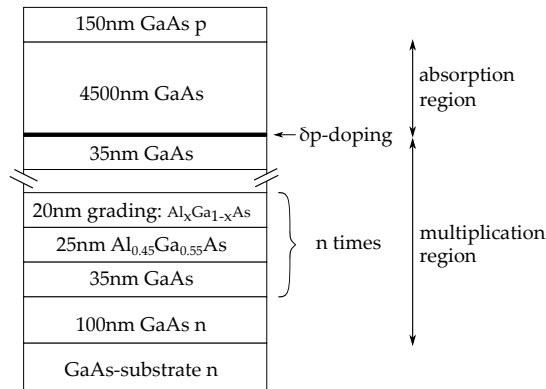


Figure 1.5: Sketch of the structure adopted in this work.

Eventually, as suggested in [15], in order to improve the gain of the device, a change in the structure was made, and in the first two steps of the multiplication region the AlGaAs were replaced with InGaAs in order to have a larger ΔE_c . To exploit the potential interest of the use of $\text{In}_x\text{Ga}_{1-x}\text{As}$ -based materials, one would ideally need a substrate, which is lattice-matched to the active layers of the device, in order to prevent dislocations from degrading the device properties. Unfortunately, only heterostructures of one particular composition ($\text{In}_{0.52}\text{Al}_{0.48}\text{As}/\text{In}_{0.53}\text{Ga}_{0.47}\text{As}$) can be grown lattice-matched to a commercial binary substrate (InP). However, with particular precautions, thin layers of $\text{In}_x\text{Ga}_{1-x}\text{As}$ can be grown on GaAs.

1.3 GENERAL ASPECTS OF SEMICONDUCTOR MATERIALS

Semiconductors find widespread use in photonics as they serve as detectors and have many other important roles [7], opening perspectives for fundamental sciences as astrophysics, X-ray spectroscopy for material study and analysis, medical imaging systems, and many industrial applications [16].

In the X-ray region, especially for applications in synchrotron radiation experiments, detectors have been traditionally based on silicon, as it is the most mature technology [17]. Up to now they have been quite adequate in terms of the performance. However, especially for synchrotron radiation experiments utilizing mid and hard X-rays ($> 10 \text{ keV}$, as described in section 1.3.1) silicon based devices become inefficient and this has led to the research of new materials [18].

	IIA	IIIA	IVA	VA	VIA
2		5 B	6 C	7 N	8 O
3	12 Mg	13 Al	14 Si	15 P	16 S
4	30 Zn	31 Ga	32 Ge	33 As	34 Se
5	48 Cd	49 In	50 Sn	51 Sb	52 Te
6	80 Hg		82 Pb		

Gas

Solid

Liquid

Figure 1.6: Partial view of the periodic table regarding semiconductors. The different colors highlight the form the elements take at room temperature: solid, gas and liquid, respectively, gray, yellow and turquoise [7].

Gallium arsenide is a compound semiconductor that possess some advantages compared to Si, such as the shorter absorption length (Fig. 1.8b) and larger electron mobility, which translate into thinner devices and shorter response times. The high-atomic number of its constituents (Fig. 1.6) and its wide bandgap (1.42 eV) result in a high photon absorption (similar to germanium and ten times higher with respect to silicon [16]) and a lower leakage current allowing X-ray detection even at room temperature. Another advantage is its relatively low electron-hole pair creation energy (4.184 eV at 300 K) which allows similar statistic and spectroscopic resolution to Si [18]. A comparison between the characteristics of GaAs and those of Si can be seen in Table 1.1.

	GaAs	Si
Crystal structure	zinblende	diamond
Number of atoms [cm^{-3}]	$4.42 \cdot 10^{22}$	$5 \cdot 10^{22}$
Density [g cm^{-3}]	5.32	2.329
Dielectric constant <i>static</i>	12.9	11.7
Dielectric constant <i>high frequency</i>	10.89	
Energy gap [eV]	1.424	1.12
Breakdown field [V cm^{-1}]	$\simeq 4 \cdot 10^5$	$\simeq 3 \cdot 10^5$
Mobility [$\text{cm}^2 \text{V}^{-1} \text{s}^{-1}$] <i>electrons</i>	8500	1400
Mobility [$\text{cm}^2 \text{V}^{-1} \text{s}^{-1}$] <i>holes</i>	400	450
Diffusion coefficient [$\text{cm}^2 \text{s}^{-1}$] <i>electrons</i>	200	36
Diffusion coefficient [$\text{cm}^2 \text{s}^{-1}$] <i>holes</i>	10	12

Table 1.1: Properties of GaAs and Si. Mobility data are upper bounds referring to undoped material [11, 19].

Furthermore, this material together with other III-V semiconductors can be arranged in different ways as crystal-growth techniques such as molecular beam epitaxy (MBE) can be used to grow these materials with particularly designed band structures. If their super-

lattice structure, consisting of nanometric-size alternating layers of compound semiconductors, is properly arranged and the electron-hole pair creation occurs just in a particular region of the device, it is also possible to minimize the multiplication noise [6]. Specifically, the well-established microelectronic technology is another advantage of GaAs with respect to other high- Z , wide bandgap semiconductors.

For these reasons, a short introduction to some III-V semiconductor properties with particular focus on GaAs will be presented.

1.3.1 III-V compound semiconductors

Gallium arsenide is a III-V semiconductor which takes the form of a zincblende structure comprising two face-centered-cubic lattices: one of Ga atoms and the other of As atoms. Each atom is surrounded by four atoms of the opposite type, equally spaced and located at the corners of a regular tetrahedron. The conventional cube cell of GaAs can be seen in Fig. 1.7.

GaAs

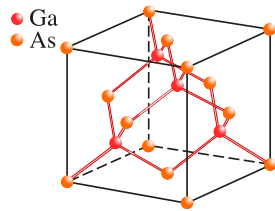


Figure 1.7: Zincblende structure of GaAs [7]. It differs from the diamond structure of silicon where all the positions are occupied with Si.

From the standpoint of electronic properties, this semiconductor is characterized by a bandgap energy E_g of 1.42 eV at room temperature [7].

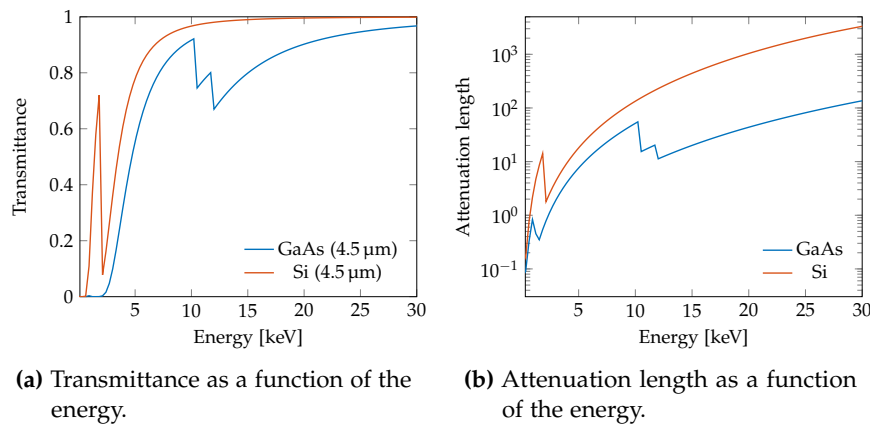


Figure 1.8: Comparison between transmittance of a bulk region of 4.5 μm and attenuation length of GaAs and Si, blue and red, respectively.

Its transmittance is shown in Fig. 1.8a for the case of a 4.5 μm -bulk layer (the reason why this length is represented is that it is a distinctive feature of most of the devices analyzed in this work).

*Ternary
semiconductors*

Figure 1.8b shows, instead, the attenuation length of the material. Both curves are compared to those of Si.

Aluminum gallium arsenide is a ternary compound which is formed from two elements of group III with one element from group V. The ratio of which these elements are present in the compound is expressed by the compositional mixing ratio x , as $\text{Al}_x\text{Ga}_{1-x}\text{As}$. Its properties interpolate between the ones of AlAs and those of GaAs, so influencing the bandgap, which varies from 1.42 eV to 2.16 eV as x goes from 0 to 1 [7].

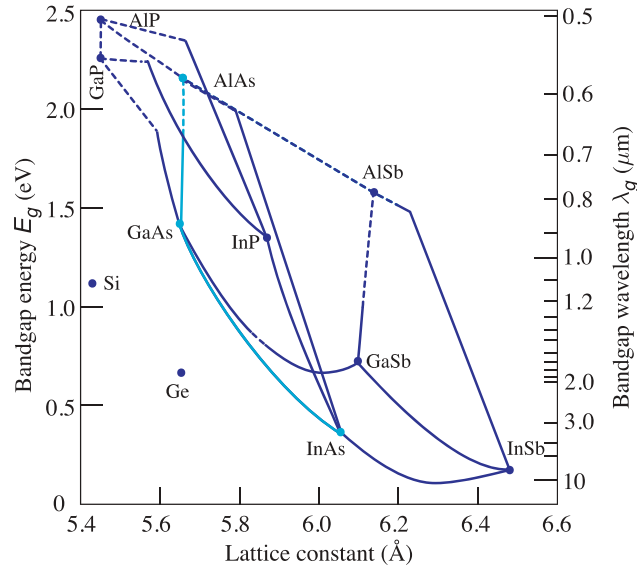


Figure 1.9: Bandgap energy and wavelength versus lattice constant are represented [7]. Solid and dash lines represent direct and indirect bandgap, respectively. As it can be seen, there are cases where a material can present a different type of bandgap for different mixing ratios, as it is the case between AlAs and GaAs. In light blue are highlighted the curves of interest in this research project.

In Fig. 1.9 the bandgap as a function of the lattice constant can be observed. The line connecting AlAs to GaAs shows the possible bandgaps $\text{Al}_x\text{Ga}_{1-x}\text{As}$ can assume. The fact that the line which connects these two elements is vertical is important because it translates into the property that such material can be grown on GaAs without lattice mismatch. Moreover, this line is both solid and dash, meaning that for a given mixing ratio the bandgap is either direct (up to $x = 0.45$) or indirect, respectively. We are mainly interested in the former, as materials which possess this characteristic are able to interact directly with photons. In fact, in this case it is necessary to provide just an energy of the order of the bandgap and no further particle is needed to provide for the momentum. This makes the interaction with photons more likely to happen [11].

Another useful ternary compounds is $\text{In}_x\text{Ga}_{1-x}\text{As}$, which also can be grown on GaAs without mismatching. However, as can be seen in

Fig. 1.9, the line connecting GaAs to InAs is not vertical, thus choosing an appropriate composition ratio x and proper growth characteristics, e.g. the growth temperature, is very important for matching the lattice constants.

1.4 BASICS OF IMPACT-IONIZATION

Impact ionization is a three-body collision process [9] where free carriers (either electrons or holes or both) are accelerated by a high electric field until they gain sufficient energy to promote an electron from the valence band into the conduction band.

As previously mentioned, by the use of “bandgap engineering” it is possible to arrange where the impact ionization is going to occur designing the ionization rates of electrons and holes, rather than simply accepting the values given in a particular material [20]. Thus, it is possible to exploit this property to develop devices able to detect low photon fluxes. Some basic useful information to better understand this mechanism will be covered.

1.4.1 Drift and Diffusion

When an electric field is applied to a semiconductor sensor, charge carriers experience a driving force that increases their average velocity with respect to the one they have when no field is applied (equilibrium condition). In particular, the motion of electrons and holes under this condition is called drift motion and it is described by the drift current densities:

$$J_n = qn\mu_n E \quad J_p = qp\mu_h E \quad (1.17)$$

where q is the charge of the carrier, E is the field which establishes in the structure, n and p are the charge densities and, μ_n and μ_h are the mobilities of electrons and holes, respectively [11].

These carriers, however, move also owing to the concentration gradients, with the following diffusion current densities:

$$J_n = qD_n \nabla n \quad J_p = qD_h \nabla p \quad (1.18)$$

where D_n and D_h are each the diffusivity of the charge particle taken into account, electron and hole, respectively. The electron drift velocity-field curves of a few semiconductors can be seen in Fig. 1.10

Thus, the overall velocity is due to both mechanisms [11].

1.4.2 Generation and Recombination

Through mechanisms of generation and recombination, carriers that undergo the processes described in 1.4.1 can be created. These mechanisms can be either phonon-assisted (thermal), or photon-assisted

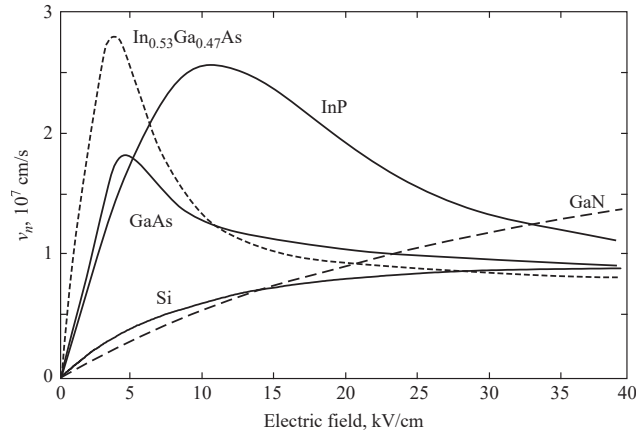


Figure 1.10: Electron drift velocity-field referring to some intrinsic semiconductor materials [11].

(radiative), or even assisted by other electrons or holes. The generation-recombination mechanisms are described by the rates with which electron and holes are generated (G_n and G_h for electrons and holes, respectively) and recombined (R_n and R_h for electrons and holes, respectively) per unit time. The net recombination rates are described as

$$U_n = R_n - G_n \quad U_h = R_h - G_h \quad (1.19)$$

and they are expressed by the continuity equations in 1.20

$$\begin{cases} \frac{\partial n}{\partial t} = \frac{1}{q} \frac{\partial J_n}{\partial x} - U_n \\ \frac{\partial p}{\partial t} = -\frac{1}{q} \frac{\partial J_p}{\partial x} - U_h \end{cases} \quad (1.20)$$

where x is the spatial coordinate that represents the depth in the device.

In particular, impact ionization is a mechanism of generation of electron-hole pairs.

1.4.3 Impact Ionization

Impact ionization is the main process that occurs in the device under study (described in section 1.2.3). Figure 1.11 shows the way this process takes place. In particular, in this representation the first electron-hole pair is created by a photon. Afterwards, thanks to the electric field applied to the structure, the charged particles are accelerated and if they gain sufficient energy they can interact with the lattice. Indeed, if a carrier, e.g. an electron (also called primary electron), gains enough kinetic energy E_k (higher than the bandgap energy E_g , in direct bandgap materials) after a scattering event its energy

can be transferred to another electron in the valence band (secondary electron) which is excited to the conduction band. The process results in two electrons in the conduction band and one hole in the valence band, which can undergo the same process. A similar process can occur for holes in the valence band.

The electric field required in order to obtain $E_k > E_g$ depends on the bandgap of the material.

If most of the secondary particles gain sufficient energy to undergo the same process, the avalanche effect can be triggered, increasing greatly the carrier density. Thus, many consecutive impact ionization events produce avalanche multiplication.

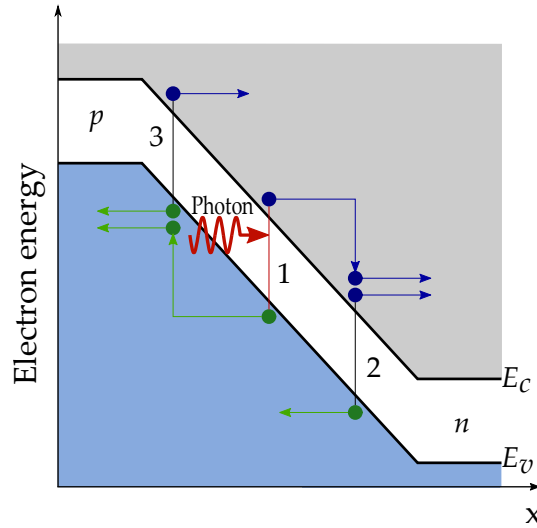


Figure 1.11: Impact ionization caused by a photon [7]: at 1 the photon-generated electron-hole pair, while at 2 and 3 the pairs which are generated by impact ionization.

1.4.3.1 Ionization rates

The impact ionization coefficients or rates for electrons and holes (α and β , respectively) can be defined as the reciprocal of the average distance which is required by either carriers to travel before undergoing an electron-hole pair creation process; so, they are ionization probabilities per unit length (cm^{-1}). The ionization coefficient increases with a higher electric field, since this provides an additional acceleration, and it decreases with increasing temperature, since the increasing frequency of collision does not allow the carriers to gain sufficient energy to ionize [7]. For example one way to express them is by using Equation 2.1, here reported:

$$\begin{cases} \alpha = A_e \exp\left(-\left(\frac{B_e}{E}\right)^{\gamma_e}\right) \\ \beta = A_h \exp\left(-\left(\frac{B_h}{E}\right)^{\gamma_h}\right) \end{cases} \quad (1.21)$$

where E is the absolute value of the electric field and, A_i , B_i and γ_i with $i \in \{e, h\}$ are the proper coefficients chosen to adjust them to experimental results. Though Equation 2.1 is a reasonably good approximation it still suits lots of working devices. In Chapter 2, different formulations of the more complicated models used for impact ionization will be proposed.

Ionization ratio
 $k = \alpha/\beta$

The ratio of α over β is called k . This is important because it is a way to characterize the performance of a device. If k is close to 1, meaning that the two coefficients are comparable, the material is not suitable for the fabrication of APDs because the noise performance is degraded. In fact, if the two coefficients are comparable, it means that both electrons and holes undergo similar impact ionization. Although this feedback process, where each carrier produces other carriers, increases the gain of the device, generating a larger amount of charge per photocarrier pair, it is not desirable. It is time consuming, reducing the device bandwidth; it is random, thus it increases the noise, and it can be unstable, leading to avalanche breakdown. These are the reasons why single carrier multiplication is more desirable [7]. In some materials, as silicon, this phenomenon occurs naturally, however in others, as III-V semiconductors, this does not happen. And this has led to search for a way to artificially change this ratio in III-V semiconductor, by using superlattice structures [14].

1.4.3.2 Gain and excess noise factor

Impact ionization can be quantified through some parameters. Below, two of the most important ones are described: gain and excess noise factor.

Gain. In some detectors the number of collected pairs is approximately equal to the number of photo-generated pairs. However, certain detectors have internal gain mechanisms whereby the number of collected pairs may be much larger than that of the photo-generated ones. The internal gain can be associated to an amplification M of the photocurrent that would have been generated if no gain were present [11].

The multiplication gain M represents the ratio between the total current (whose density is J) actually present in multiplication regime and the one not multiplied, which can be thought as an injected current (whose current density, $J_n(0)$ and $J_p(W)$, is shown in Fig. 2.1). Multiplication can be classified also according to the type of carrier that initiates the process (e.g. $M_n = J/J_n(0)$ and $M_p = J/J_p(W)$, electron- and hole- induced, respectively). The analytical form used to describe this will be expressed in Chapter 2, where it will be also shown how the gain depends on the electron and hole impact ionization rates, as well as on other parameters (e.g. the width of the multiplication

region W).

Excess noise factor. The excess noise factor F is a measure of how noisy the device is. In fact, the excess noise factor is the value that shows how much the power spectral density of the actual noise (net of the gain) differs from the ideal shot noise. For definition it can be expressed as

$$F = \frac{S_i}{S_{i,shot} \cdot M^2} \tag{1.22}$$

in other words, as the ratio between the total power spectral density and the shot noise multiplied by the square of the gain.

Owing to the discrete nature of the electric charge, the total current in the device can be represented as the sum of a large number of independent events $i_p(t)$ occurring at a random average λ . The arrival time frequency can be expressed as $\lambda = I_{PH}/q$, where I_{PH} is the current without the multiplication phenomena.

The total current, then, can be represented by the sum of the pulses as

$$i(t) = \sum_p i_p(t - t_p) \tag{1.23}$$

where t_p is the pulse arrival time. So, even if from a macroscopic point of view the current seems to be constant, microscopically its instantaneous value oscillates around a mean value, as shown in Fig. 1.12.

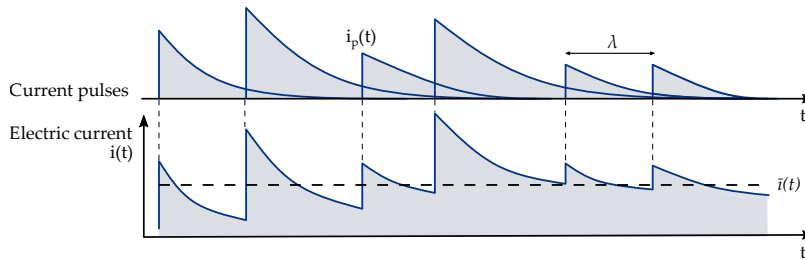


Figure 1.12: The photocurrent induced in a photodetector circuit comprises the superposition of current pulses, differently multiplied, each associated with a detected photon. The illustrated individual pulses are decaying step functions. Their superposition constitutes the shot noise [7].

In particular, for photon generated electrons, the differential probability dp , which describes the time intervals between adjacent random events, is given considering that the next event will take place within a differential time dt after a time interval of length t by

$$dp = I(t)dt = \lambda e^{-\lambda t} dt \tag{1.24}$$

where λ is the average events of occurrence as stated above. This is due to the fact that photon detection follows a Poisson counting

process. Equation 1.24 implies that the interoccurrence time between two successive photon detections tends to be null.

Considering a device able to perform multiplication, the area of the single pulse depends on the stochastic process $m(x)$ which is the APD gain at the section x and can be expressed as

$$\int i_p(t) dt = qm(x). \quad (1.25)$$

The Fourier transform $\Psi(f)$ of $i_p(t)$ is $\mathcal{F}\{i_p(t)\} = \int_{-\infty}^{+\infty} i_p(u)e^{-j2\pi fu} du$, and it can be calculated for each different individual event¹ leading, using Carson's formula [21], to the power spectral density of the signal of equation 1.23

$$S_i = 2\lambda \overline{|\Psi_p(f)|^2} \quad (1.26)$$

where $\overline{|\Psi_p(f)|^2}$ is the average value of $|\Psi_p(f)|^2$. Moreover, since for low frequency we can consider that

$$\mathcal{F}\{i_p(t)\} = \int i_p(u) du \quad (1.27)$$

we can obtain from equations 1.25 and 1.27 the following

$$\Psi_p(f) = \mathcal{F}\{i_p(t)\} = \int i_p(u) du = qm(x) \quad (1.28)$$

where x is the position where impact ionization occurs, and using equation 1.26 with $\lambda = I_{PH}/q$ it results

$$S_i = 2\lambda q^2 \overline{m(x)^2} = 2qI_{PH} \overline{m(x)^2}. \quad (1.29)$$

If we do not consider the randomness of the multiplication process, and think of our device as a linear system characterized by a response function M , then the power spectrum density of the shot noise results in

$$S_{i,shot_{multiplied}} = 2qI_{PH}M(x)^2 = 2qI_{PH} \overline{m(x)^2}. \quad (1.30)$$

Thus for the definition of the excess noise factor (equation 1.22) is that

$$F(x) = \frac{S_i}{S_{i,shot_{multiplied}}} = \frac{\overline{m(x)^2}}{\overline{m(x)}^2}. \quad (1.31)$$

¹ if the events are absolutely integrable

Impact ionization (II) is the main mechanism responsible for the gain in the avalanche photodiodes considered during this work. Being able to model it correctly allows the interpretation of the experimental data and optimization of the devices. Hereinafter, the theory of some models for impact ionization, namely local and nonlocal ones, will be presented, focusing on the gain of the detectors and the associated multiplication noise.

The main difference between these two types of model is the dependence of the ionization coefficients on the electric field: the local model is characterized by coefficients depending only on the electric field at the specific position of ionization, and can be used with photodiodes with a large multiplication region (some micrometers); the nonlocal model relies on coefficients which take into account the non locality of the charge carriers, and the dependence on the overall electric field profile and on the path traveled by the carriers after being generated (by light or by II). The latter model is used especially for short multiplication regions (hundreds of nanometers or less) in order to overcome the limitations of the local models. Specifically, the nonlocal model which will be presented is the Energy Balance History Dependent Model (EBHDM) developed and implemented by Nichetti and Pilotto and published in [22].

2.1 LOCAL MODEL

As mentioned in Chapter 1, photodiodes which exhibit a gain may improve the signal-to-noise-ratio of the detection system, provided that the noise generated by the multiplication process does not become too high. Local models are accounted to describe gain and noise caused by impact ionization in those photodiodes with large multiplication regions, in other words, where the avalanche multiplication characteristics are more or less uniform over a considerable portion of the multiplication region [6].

Moreover, the local model is useful to better understand some general aspects of APDs, like the noise behavior in case of similar impact ionization coefficients for electrons and holes ($\alpha \sim \beta$) or the performance in the case of single-carrier multiplication ($\beta \sim 0$, i.e. just electron multiplication).

Let us consider a p-i-n structure under reverse bias, which is a simplified way to look at the structure of the devices analyzed in the

following thesis. It presents a depletion region, which can be thought of as developing from 0 to W and an electric field E of arbitrary profile sufficiently high to have impact ionization. In this structure electrons are supposed to move towards right and holes to the left (Fig. 2.1).

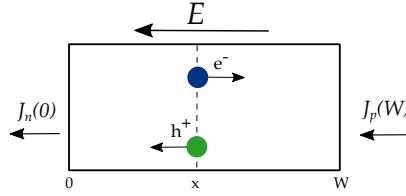


Figure 2.1: Representation of the depletion region of the structure under investigation, where the direction of the movement of the carriers is highlighted; E is the electric field and $J_n(0)$ and $J_p(W)$ are the injection current densities of electrons and holes, respectively.

Ionization coefficients In the local model it is assumed that electrons and holes, traveling through the depletion region, possess ionization probabilities per unit length depending point-by-point only on the electric field, equal to α and β , respectively. This consideration means that the ionization probability depends only on the instantaneous momentum of the carriers. Usually, carriers can impact ionize only when their energy exceed above a specific threshold energy, which they may acquire after traveling in a region with a significant voltage drop. Conversely, considering that the ionization coefficients depend only on E and not on the previous carrier history implies that a carrier always acquires an energy of at least ϵ_{ii} (the minimum energy for impact ionization) within a distance smaller than the mean distance between ionization collision and also smaller than the length over which E changes by an appreciable amount. ϵ_{ii}/eE can be considered as an estimation of the distance a carrier travels to undergo impact ionization, which means that the total voltage drop across the region of interest must be larger than ϵ_{ii}/e [6].

Many authors, who have investigated impact ionization in the drift-diffusion framework, have suggested an exponential relation between the coefficients (α and β) and the electric field E [23] as

$$\begin{cases} \alpha(x) = A_e \exp\left(-\left(\frac{B_e}{E(x)}\right)^{\gamma_e}\right) \\ \beta(x) = A_h \exp\left(-\left(\frac{B_h}{E(x)}\right)^{\gamma_h}\right) \end{cases} \quad (2.1)$$

where $E(x)$ is the electric field profile, A_i , B_i and γ_i with $i \in \{e, h\}$ are proper coefficients chosen to adjust them to the experimental results.

Current As a preface to determine the gain of an APD let us consider the double-carrier multiplication problem. Consider the mono dimensional structure of Fig. 2.1: with an electric field applied and a

depletion region spanning from 0 to W , a total current caused by both electrons and holes will establish through it. The total current density J is determined by the expression

$$J = J_n(0)M(0) + J_p(W)M(W) + \int_0^W G_o(x)M(x) dx \quad (2.2)$$

whose derivation can be found in Appendix A.1.1. $J_p(W)$ and $J_n(0)$ are the thermally and optically generated holes and electrons entering at the two ends of the depletion region, G_o is the optic and thermally generation rate, and $M(0)$ and $M(W)$ are the multiplication factors for electrons and holes injected [6]. Moreover, for the continuity equation J must remain constant

$$J_n(x) + J_p(x) = J \quad (2.3)$$

where $J_n(x)$ is the electron current density and $J_p(x)$ the hole one.

Since charges generated in an element of distance dx are created in pairs, to calculate the overall current we need to calculate just one of the two rates. So, within a distance dx , on average the current is incremented by

$$dJ_n = (\alpha J_n + \beta J_p + G_o)dx \quad (2.4)$$

where αJ_n and βJ_p are the pair generation rate per unit length due to impact ionization of electrons and holes, respectively, and, G_o is the term that takes into account the optic and thermal generation rate [6].

Remark 2.1: first-order linear differential equation

The solution of a first-order differential equation with variable coefficients $\frac{df(x)}{dx} + a(x)f(x) = g(x)$, knowing the Cauchy condition $y(x_o) = y_o$, is

$$f(x) = e^{-A(x)} \left[y_o + \int_{x_o}^x g(t)e^{A(t)} dt \right] \quad \text{with} \quad A(x) = \int_{x_o}^x a(t) dt.$$

Solving the first order differential equation 2.4 as suggested by the remark 2.1, considering also the quasi-steady-conditions ($J_n(0) = J_p(W) = 0 \Rightarrow J_n(W) = J$), leads to obtaining $J_n(x)$

$$J_n(x) = e^{\int_0^x (\alpha - \beta) dx'} \left[J_n(0) + \int_0^x (\beta J + G_o(x)) e^{-\int_0^{x'} (\alpha - \beta) dx''} dx' \right] \quad (2.5)$$

where for simplicity the dependence of α and β on x is not shown. Equation 2.5 can be further processed in $x = W$ and rearranged as

$$J = \frac{\int_0^W G_o(x) e^{\int_x^W (\alpha - \beta) dx'} dx}{1 - \int_0^W \beta(x') e^{\int_{x'}^W (\alpha - \beta) dx''} dx'}. \quad (2.6)$$

Continuity equation
 $\frac{dJ}{dx} = 0 \Rightarrow \frac{dJ_n}{dx} = -\frac{dJ_p}{dx}$

Avalanche multiplication gain As already stated, avalanche multiplication is a typical effect that establishes in some photodiodes when high fields are involved and impact ionization occurs. Considering the electron-hole pair created at x inside the depletion region, traveling over a distance dx : the electron will undergo ionization on average αdx times while the hole βdx . The secondary pairs created will also undergo impact ionization. Thus, if $M(x)$ is the average total number of pairs generated in the depletion layer from one pair created at x [6]

$$M(x) = 1 + \int_0^x \beta M(x') dx' + \int_x^W \alpha M(x') dx' \quad (2.7)$$

Once differentiated:

$$\frac{dM(x)}{dx} = -(\alpha - \beta)M(x) \quad (2.8)$$

whose solution, as suggested in remark 2.1, is

$$M(x) = M(W)e^{\int_x^W (\alpha - \beta) dx'}. \quad (2.9)$$

That leads, as shown in the calculation found in Appendix A.1.2, to

$$\begin{aligned} M(x) &= \frac{e^{\int_x^W (\alpha - \beta) dx'}}{1 - \int_0^W \beta(x') e^{\int_{x'}^W (\alpha - \beta) dx''} dx'} \\ &= \frac{e^{-\int_0^x (\alpha - \beta) dx'}}{1 - \int_0^W \alpha(x') e^{-\int_0^{x'} (\alpha - \beta) dx''} dx'}. \end{aligned} \quad (2.10)$$

This formula points out that any electron-hole pair created in x' in the chain of pairs resulting from an initial ionization at x will itself be multiplied by $M(x')$.

Remark: Alternative way to obtain the gain

$M(x)$ can also be obtained by comparing equation 2.2 with equation 2.6, where the boundary conditions have been taken into account, giving the same results as in equation 2.10.

*Single carrier
injection*

The multiplication factor can be calculated over the entire diode. In particular, if calculated in $x = 0$ and $x = W$ it gives the multiplication in the case of single-carrier injection M_n and M_p , for electrons and holes, respectively.

$$M(W) = M_p = \frac{1}{1 - \int_0^W \beta(x') e^{\int_{x'}^W (\alpha - \beta) dx''} dx'} \quad (2.11)$$

$$\begin{aligned}
M(0) = M_n &= \frac{e^{\int_0^W (\alpha-\beta) dx'}}{1 - \int_0^W \beta(x') e^{\int_{x'}^W (\alpha-\beta) dx''} dx'} \\
&= \frac{1}{1 - \int_0^W \alpha e^{-\int_0^{x'} (\alpha-\beta) dx''} dx'}
\end{aligned} \tag{2.12}$$

Avalanche multiplication noise In the local field model, the total generation rate is a random variable with a Poissonian probability distribution [1], so that the unilateral spectral density of its noise is $S_i = 2qI$ as described in Section 1.4.3.2, where q is the elementary charge and I is the average current. If the assumptions of the local model are implied, it can be assumed that the current generated in dx exhibits full shot noise, thus $\sigma_{in}^2 = \overline{(dI_n - \overline{dI_n})^2} = S_i df$, which leads to

$$\overline{(dI_n - \overline{dI_n})^2} = 2qdI_n df \tag{2.13}$$

in an element of bandwidth df . This element of current noise can be thought of as originating from a noisy current generator at x and will undergo the same multiplication as any other current generated at x . Thus, if Ψ is the noise spectral density in the total current established in the device, the contribution due to the pair generation rate in dx is given by

$$d\Psi(x) = dS_i = 2qM^2(x)dJ_n(x) \tag{2.14}$$

and this is the key to understanding the mechanism of noise generation [6].

Therefore, considering that each noise source is of shot noise type and that such noise is then further multiplied by the square of the local average value of the gain, integrating equation 2.14 the total noise spectral density is given by equation 2.15a [6]

$$S_i = 2q \left[J_n(0)M^2(0) + J_p(W)M^2(W) + \int_0^W \frac{J_n}{dx} M^2(x) dx \right] \tag{2.15a}$$

$$= 2q \int_0^W G_o(x)M^2(x)F(x) \tag{2.15b}$$

where the last equivalence (equation 2.15b) is to be consider under the verified boundary conditions $J_n(0) = J_p(W) = 0$. From the comparison between the two equations of 2.15 it is possible to obtain the excess noise factor F :

$$F(x) = 2 + \left[2 \int_0^W \beta(x') e^{2 \cdot \int_{x'}^W (\alpha-\beta) dx''} dx' - 1 \right] \frac{M(W)}{e^{\int_x^W (\alpha-\beta) dx'}} \tag{2.16}$$

as shown in Appendix A.1.3.

2.1.1 SNR analysis

The structure described in section 1.2.3 and used in this thesis is a separated absorption and multiplication APD. If opportune photon energies are chosen, single-carrier injection (i.e. of electrons) can be assumed. Thus, the gain (equation 2.10) and the excess noise factor (equation 2.16) used to calculate the signal-to-noise ratio (SNR) must be calculated in $x = 0$.

The SNR can be calculated as

$$\text{SNR} = \frac{(I_{PH}M)^2}{\left(2qI_{PH}M^2F + S_{nn}(f)\right)\Delta f} \quad (2.17)$$

where I_{PH} is the photogenerated current, S_{nn} the current spectrum of the amplifier referred to the input and Δf the bandwidth.

From this expression it is possible to study some particular cases useful to better understand some general characteristic of APDs. Let us observe two cases: the first one considering similar impact ionization coefficients ($\alpha \sim \beta$), which is the condition for most III-V semiconductor as GaAs and the second one considering single-carrier multiplication in particular electron multiplication only ($\beta \sim 0$).

$\alpha \sim \beta$ This is the typical case for III-V-material-based APDs, where both electrons and holes undergo impact ionization at the same rate. Let us use the hypothesis $\alpha \sim \beta$ in equations 2.10 and 2.16:

$$M = \frac{1}{1 - \int_0^W \alpha dx'} \quad (2.18)$$

$$\begin{aligned} F &= 2 + \left(2 \int_0^W \alpha dx' - 1\right) \frac{1}{1 - \int_0^W \alpha dx'} \\ &= 2 + \left(2\left(1 - \frac{1}{M}\right) - 1\right)M \\ &= M \end{aligned} \quad (2.19)$$

which leads to the following simplified SNR:

$$\text{SNR} = \frac{(I_{PH}M)^2}{\left(2qI_{PH}M^3 + S_{nn}(f)\right)\Delta f}. \quad (2.20)$$

This case represents an ideal situation and in order to find the optimum value of M we need to find the values that satisfy $\frac{\partial(1/\text{SNR})}{\partial M} = 0$, thus

$$\frac{\partial}{\partial M} \left(\frac{2qM}{I_{PH}} + \frac{S_{nn}(f)}{I_{PH}^2 M^2} \right) = 0 \quad (2.21)$$

whose solution is

$$M_{\text{OPT}} = \sqrt[3]{\frac{S_{nn}(f)}{qI_{PH}}}. \quad (2.22)$$

Equation 2.22 provides the optimum value and the maximum obtainable gain within this situation. This result shows that in case of similar ionization coefficients for electrons and holes there is no convenience in multiplying charge indefinitely, because after the optimal value the SNR is going to degrade.

$\beta \sim 0$ This second case is typical of some materials like Si and also of opportunely grown super-lattice structures, where one of the charge carriers is multiplied much more than the other one. Let us apply $\beta \sim 0$ to equations 2.10 and 2.16:

$$\begin{aligned} M &= \frac{1}{1 - \int_0^W \alpha e^{-\int_0^{x'} \alpha dx''} dx} \\ &= \frac{1}{1 + \left[e^{-\int_0^{x'} \alpha dx''} \right]_0^W} \\ &= e^{\int_0^W \alpha dx'} \end{aligned} \quad (2.23)$$

$$F = 2 - e^{-\int_0^W \alpha dx'} = 2 - \frac{1}{M}. \quad (2.24)$$

In this case the SNR will be

$$\text{SNR} = \frac{(I_{PH}M)^2}{\left[2qI_{PH}M^2 \left(2 - \frac{1}{M} \right) + S_{nn}(f) \right] \Delta f}. \quad (2.25)$$

This expression is devoid of any maxima for finite values of M , thus the greater the gain M the higher is going to be the SNR. Therefore, we are able to amplify the signal without degrading the signal-to-noise ratio.

As mentioned before, III-V semiconductors are characterized by $\alpha \sim \beta$, seemingly precluding them from being used as APDs. However, to overcome this limitation, it is possible to use particular super-lattice structures. These structures are characterized by abrupt changes in the electric field, making the use of the local model not suitable anymore, and they necessitate more accurate and advanced models than the nonlocal ones.

2.2 NONLOCAL MODELS

Impact ionization in thick multiplication regions is adequately described by local models in which the ionization coefficients are functions only of the local electric field, as described in 2.1. In devices

featuring thin multiplication regions nonlocal effects are significant, and new models that take into account the path that a carrier experiences before gaining sufficient energy to impact ionize are necessary. Carriers at a given position have different ionization probabilities depending on the location where they were generated either by optical absorption or by ionization processes.

The nonlocal history-dependent models proposed so far in the literature differ in the way they correlate the ionization coefficients with the electric field profile. There are two predominant approaches in the literature to describe the phenomenon of nonlocal history-dependent impact ionization: one is the model proposed by McIntyre [1], which transforms the electric field profile into an effective field by the convolution with a Gaussian function in space that mimics a soft ionization threshold; the other one is the *dead space* model developed by Hayat [24], which assumes that the ionization coefficient is null within a distance from the generation position and this distance is the one required for the carriers to attain an energy equal to a suitable ionization threshold.

However, their application to staircase APDs is not straightforward. For instance, in the dead space model it is not obvious to decide whether the dead space should be accounted for at every step or only at the first one encountered by the ionizing carrier [25]. On the other hand, the history-dependent model of McIntyre in [1] is not applicable to staircase APDs because it relates the parameters of the Gaussian function to the local electric field and becomes singular in the presence of band discontinuities. Inspired by [26] and [27], the nonlocal energy-balance history-dependent model (EBHDM) applicable to the interpretation of electrical measurements on single-photon staircase APDs is presented below.

2.2.1 Energy-balance history-dependent model

Just for a matter of visual simplicity (the same reasoning is applicable to staircase APDs), let us consider a p-i-n junction whose multiplication region extends from 0 to W : we assume that the carriers are created in x , either by optical generation or by impact ionization and ionize in x' within a distance dx . If the junction is reverse-biased electrons will drift from left to right while holes will move in the opposite direction, as shown in Fig. 2.2.

In this situation, once defined the electron ionization coefficient $\alpha(x|x')$, the probability that the first ionization of an electron will happen between x' and $x' + dx'$ is:

$$\begin{aligned} p_e(x|x')dx' &= \alpha(x|x') \left[e^{-\int_x^{x'} \alpha(x|x'')dx''} dx' \right] \\ &= \alpha(x|x') \left[P_{se}(x|x')dx' \right] \end{aligned} \quad (2.26)$$

where $p_e(x|x')$ is the probability density, which is equal to the ionization coefficient multiplied by the survival probability $P_{se}(x|x')$, which in turn expresses the probability that a carrier does not ionize between x and x' .

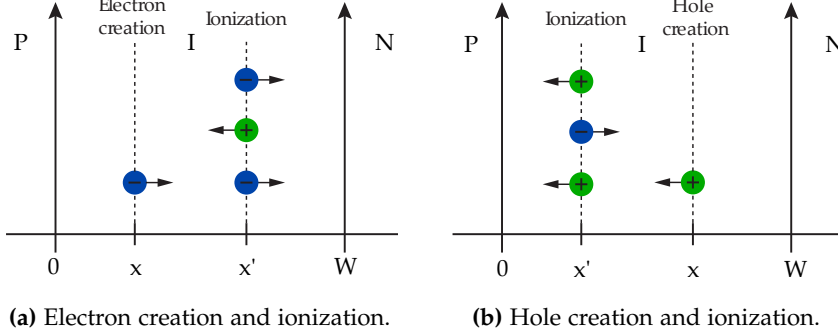


Figure 2.2: Schematic for the spatial notation used for holes and electrons. Both carriers are generated in x and they impact ionize at x' .

Similarly, for holes the terms are related as

$$\begin{aligned} p_h(x|x')dx' &= \beta(x|x') \left[e^{-\int_x^{x'} \beta(x|x'')dx''} dx' \right] \\ &= \beta(x|x') P_{sh}(x|x')dx' \end{aligned} \quad (2.27)$$

where $\beta(x|x')$ is the ionization coefficient, $p_h(x|x')$ the ionization probability density, and $P_{sh}(x|x')$ the survival probability.

Ionization coefficients The ionization coefficients are defined as the probability that a carrier generated in x will undergo a ionization collision within the interval $[x', x' + dx']$. The coefficients are $\alpha(x|x')$ and $\beta(x|x')$ for electrons and holes, respectively. Both $\alpha(x|x')$ and $\beta(x|x')$ are expressed in cm^{-1} .

The ionization coefficients do not depend only on the local field but they consider the position where the carrier was generated and the field profile between the ionization point and the generation point. So, carriers at a given position have different ionization probabilities depending on the location they were generated.

The ionization coefficients are related to suitable effective fields (a modified version of the electric field) in the form suggested by McIntyre [1].

$$\alpha_{E_{\text{eff},e}}(x|x') = A_e \cdot \exp \left[- \left(\frac{E_{c,e}}{E_{\text{eff},e}(x|x')} \right)^{\gamma_e} \right] \quad (2.28a)$$

$$\beta_{E_{\text{eff},h}}(x|x') = A_h \cdot \exp \left[- \left(\frac{E_{c,h}}{E_{\text{eff},e}(x|x')} \right)^{\gamma_h} \right] \quad (2.28b)$$

where A_e , A_h , $E_{c,e}$, $E_{c,h}$, γ_e , and γ_h are the adjustable model parameters to be calibrated against the experimental data.

V_{th_i} being the ionization threshold and $E(x)$ the electric field

However, unlike in [1] where a Gaussian function with $\lambda_i = V_{th_i}/E(x)$, with $i \in \{e, h\}$ for electrons and holes, is convolved with the electric field, in the energy-balance history-dependent model (EBHDM) the effective fields are obtained by convolving the quasi-electric-field (gradient of the bands, that is, including the band steps) with an exponential function, under the assumption that the potential profile is not significantly modified by the generated charge

$$E_{\text{eff},e}(x|x') = \frac{1}{\lambda_e} \int_x^{x'} \frac{dE_C}{dx}(x'') \exp\left(\frac{x'' - x'}{\lambda_e}\right) dx'' \quad (2.29a)$$

$$E_{\text{eff},h}(x|x') = \frac{1}{\lambda_h} \int_{x'}^x \frac{dE_V}{dx}(x'') \exp\left(\frac{x'' - x'}{\lambda_h}\right) dx'' \quad (2.29b)$$

In this thesis as in [22] the quasi-electric-fields E_C and E_V were obtained from Sentaurus TCAD simulations [28], solving the drift-diffusion equations without considering impact ionization.

Avalanche multiplication gain Once the above-mentioned ionization coefficients have been calculated, it is possible to calculate the gain of the device.

Figure 2.2 highlights the situation: in particular, let us focus on an electron generated in x (Fig. 2.2a). The result of its first ionizing collision, occurring in x' , is going to be three *cold* carriers: two electrons and a hole, each of which can generate further carriers.

cold means not having enough energy to ionize right away

Let $n_e(x|x')$ be the total number of resulting particles, both electrons and holes, generated in a single process, including the initial electron (even the first carrier will become a *cold* one downstream from the ionization process). For this single event we can therefore write:

$$n_e(x|x') = n_{e1}(x') + n_{e2}(x') + n_h(x') \quad (2.30)$$

where $n_{e1}(x')$, $n_{e2}(x')$ and $n_h(x')$ are the numbers of particles generated in the single process by the first *cold* electron, the second one and the *cold* hole, respectively. Averaging equation 2.30 we obtain

$$N_e(x|x') = 2N_e(x') + N_h(x') \quad (2.31)$$

where $N_e(x|x') = \overline{n_e(x|x')}$, $N_e(x') = \overline{n_{e1}(x')} = \overline{n_{e2}(x')}$ e $N_h(x') = \overline{n_h(x')}$.

Since the probability density that the first ionization takes place in x' is $p_e(x|x')$, the overall average of the number of electrons is:

$$N_e(x) = P_{se}(x|W) + \int_x^W \left(2N_e(x') + N_h(x')\right) \cdot p_e(x|x') dx'. \quad (2.32)$$

In equation 2.32 the first term represents the probability that an electron reaches the position W (the limit of the multiplication region) without undergoing a collision that leads to ionization, while the second term is the average number of carriers that are obtained between

x and W starting from the first ionization. Similarly, the number of holes is

$$N_h(x) = P_{sh}(x|0) + \int_0^x \left(2N_h(x') + N_e(x') \right) \cdot p_h(x|x') dx' \quad (2.33)$$

where P_{sh} is the probability that a hole reaches the position 0 without undergoing an ionizing collision, p_h is the ionization probability in x' and $n_h(x|x') = n_{h1}(x') + n_{h2}(x') + n_e(x')$.

Considering the boundary conditions

$$N_e(W) = P_{se}(W|W) = 1 \quad (2.34)$$

$$N_h(0) = P_{sh}(0|0) = 1 \quad (2.35)$$

the gain corresponding to a pair generated in the generic position x is given by:

$$M(x) = \frac{N_e(x) + N_h(x)}{2} \quad (2.36)$$

In this way, for any structure whose field distribution is known, if the probability densities are calculable, then $M(x)$ can be determined by solving equations 2.32 and 2.33.

Excess noise factor Once the history-dependent coefficients are known, it is also possible to calculate the excess noise factor, $F(x)$, which represents the noise in excess compared to the shot noise. The equation that describes the noise factor corresponding to the multiplication process triggered by an electron-hole pair generated in x , as shown in section 1.4.3.2, is

$$F(x) = \frac{\overline{m^2(x)}}{\overline{m(x)}^2} \quad (2.37)$$

Since $\overline{m(x)} = M(x)$, from equation 2.36 is possible to write

$$m(x) = \frac{n_e(x) + n_h(x)}{2} \quad (2.38)$$

with $n_e(x)$ and $n_h(x)$ being the number of carriers generated by a process triggered by the generation of the electron and the hole in x , respectively.

Furthermore, it can be deduced from equations 2.32 and 2.33 that

$$\overline{n_e^2(x)} = P_{se}(x|W) + \int_x^W \overline{(n_{e1} + n_{e2} + n_h)^2} \cdot p_e(x|x') dx' \quad (2.39)$$

$$\overline{n_h^2(x)} = P_{sh}(x|0) + \int_0^x \overline{(n_{h1} + n_{h2} + n_e)^2} \cdot p_h(x|x') dx' \quad (2.40)$$

and considering

$$\begin{aligned} N_e &= \overline{n_{e1}} = \overline{n_{e2}} \\ N_h &= \overline{n_h} \\ &\text{(section 2.2.1).} \end{aligned}$$

$$\overline{(n_{e1} + n_{e2} + n_h)^2} = 2\overline{n_e^2} + \overline{n_h^2} + 2N_e^2 + 4N_eN_h \quad (2.41a)$$

$$\overline{(n_{h1} + n_{h2} + n_e)^2} = 2\overline{n_h^2} + \overline{n_e^2} + 2N_h^2 + 4N_eN_h \quad (2.41b)$$

then $\overline{n_e^2(x)}$ e $\overline{n_h^2(x)}$ can be written in the following way

$$\begin{aligned} \overline{n_e^2(x)} = P_{se}(x|W) + \int_x^W (2\overline{n_e^2} + \overline{n_h^2} + 2N_e^2 + 4N_eN_h)\alpha(x|x') \cdot \\ \cdot p_e(x|x')dx' \quad (2.42) \end{aligned}$$

$$\begin{aligned} \overline{n_h^2(x)} = P_{sh}(x|0) + \int_x^W (2\overline{n_h^2} + \overline{n_e^2} + 2N_h^2 + 4N_eN_h)\beta(x|x') \cdot \\ \cdot p_h(x|x')dx' \quad (2.43) \end{aligned}$$

which can be quantified once $N_e(x)$ and $N_h(x)$ (equations 2.32 and 2.33) are known.

The excess noise factor can then be reformulated as

$$F(x) = \frac{\overline{m^2(x)}}{\overline{m(x)}^2} = \frac{\overline{(n_e(x) + n_h(x))^2}}{4M^2(x)} = \frac{\overline{n_e^2} + \overline{n_h^2} + 2N_eN_h}{4M^2}. \quad (2.44)$$

The gain and the excess noise factor just calculated are consistent with the results of the local model considered the local ionization coefficients (i.e. $\alpha(x|x') = \alpha(x')$ e $\beta(x|x') = \beta(x')$), as can be seen in Appendix A.2.

Implementation $N_e, N_h, \overline{n_e^2(x)}, \overline{n_h^2(x)}$ are the values needed to calculate the gain and the excess noise factor. For all of them equations 2.26 and 2.27 must be taken into account.

The first two terms can be rearranged from equations 2.32 and 2.33 as:

$$N_e(x) = e^{-\int_x^W \alpha(x|x') dx'} + \int_x^W (2N_e + N_h)(x')\alpha(x|x')e^{-\int_x^{x'} \alpha(x|x'') dx''} dx' \quad (2.45)$$

$$N_h(x) = e^{-\int_0^x \beta(x|x') dx'} + \int_0^x (2N_h + N_e)(x')\beta(x|x')e^{-\int_x^{x'} \beta(x|x'') dx''} dx' \quad (2.46)$$

while the latter two from equations 2.42 and 2.43, as:

$$\begin{aligned} \overline{n_e^2(x)} = e^{-\int_x^W \alpha(x|x') dx'} + \\ \int_x^W (2\overline{n_e^2} + \overline{n_h^2} + 2N_e^2 + 4N_eN_h)\alpha(x|x')e^{-\int_x^{x'} \alpha(x|x'') dx''} dx' \quad (2.47) \end{aligned}$$

$$\overline{n_h^2(x)} = e^{-\int_x^W \beta(x|x') dx'} + \int_x^W \left(2\overline{n_h^2} + \overline{n_e^2} + 2N_h^2 + 4N_e N_h \right) \beta(x|x') e^{-\int_x^{x'} \beta(x|x'') dx''} dx' \quad (2.48)$$

To solve them a new method that calculates the matrix form for 2.45, 2.46, 2.47, 2.48 instead of using the iterative procedure proposed in [1] was implemented [22].

After the discretization of the structure on a spatial mesh (see Fig. 2.3) equations 2.45 and 2.46 can be written as products between vectors and matrices

$$\begin{cases} \vec{N}_e = \vec{A} + \vec{B}_1 \vec{N}_e + \vec{B}_2 \vec{N}_h \\ \vec{N}_h = \vec{C} + \vec{D}_2 \vec{N}_h + \vec{D}_1 \vec{N}_e \end{cases} \quad (2.49)$$

where \vec{N}_e and \vec{N}_h are the column vectors, which represent the values of N_e and N_h on the simulation mesh, \vec{A} and \vec{C} are the column vectors that contain neither N_e nor N_h , while \vec{B}_1 and \vec{D}_i , with $i \in \{1, 2\}$, are the constant matrices, which will multiply the unknown variables. We can further rearrange the expressions obtaining the following matrix equation:

$$\begin{pmatrix} \vec{N}_e \\ \vec{N}_h \end{pmatrix} = - \begin{pmatrix} \vec{B}_1 - \vec{I} & \vec{B}_2 \\ \vec{D}_1 & \vec{D}_2 - \vec{I} \end{pmatrix}^{-1} \cdot \begin{pmatrix} \vec{A} \\ \vec{C} \end{pmatrix} \quad (2.50)$$

where \vec{I} is the identity matrix.

It has to be observed (see again Fig. 2.3) that \vec{N}_e and \vec{N}_h include only the unknown samples of N_e and N_h . The values imposed by the boundary conditions ($N_h(0) = 1$ and $N_e(W) = 1$) are not part of these vectors (highlighted in red in Fig. 2.3), but are contained elsewhere in the matrices \vec{B}_i and \vec{D}_i .

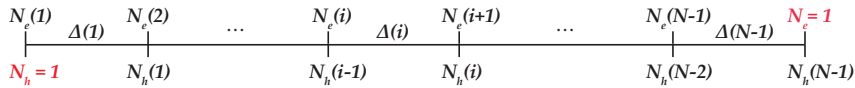


Figure 2.3: Spatial discretization of the variables N_e and N_h and indication of the boundary conditions (in red).

It is possible to write also equations 2.47 and 2.48 in a matrix form:

$$\begin{cases} \overline{n_e^2} = \vec{E} + \vec{F}_1 \overline{n_e^2} + \vec{F}_2 \overline{n_h^2} \\ \overline{n_h^2} = \vec{G} + \vec{H}_1 \overline{n_e^2} + \vec{H}_2 \overline{n_h^2} \end{cases} \quad (2.51)$$

which can be solve with the same above-mentioned reasoning.

2.2.1.1 Validation of the EBHD model

As discussed in [24] and [1], in the EBHD model the adjustable parameters that require calibration are the eight ones used in equations 2.28 and 2.29: namely, the mean free paths λ_i and A_i , E_{ci} , γ_i which correlate the effective fields with the ionization coefficients as in [6], with $i \in \{e, h\}$ for electrons and holes, respectively. The model calibration

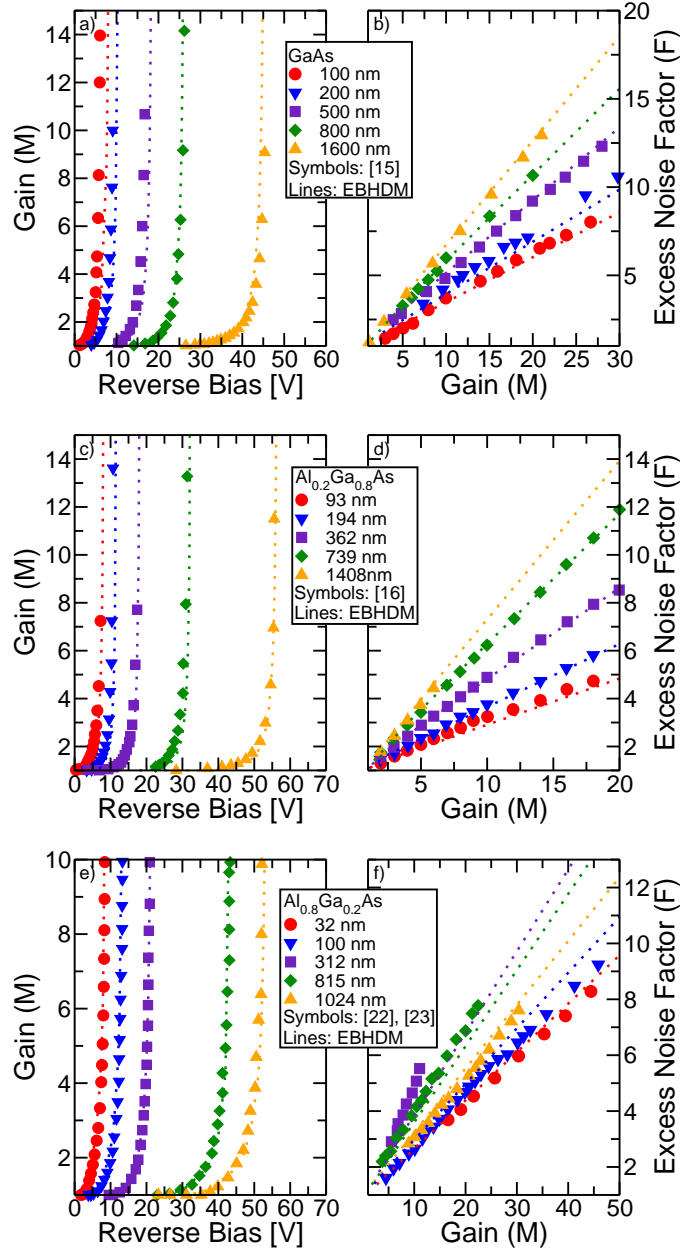


Figure 2.4: Gain as a function of the applied voltage (left) and excess noise factor as a function of the gain (right) for p-i-n diodes in (a) and (b) GaAs, (c) and (d) $Al_{0.2}Ga_{0.8}As$, and (e) and (f) $Al_{0.8}Ga_{0.2}As$. The model described in section 2.2.1 (lines) is compared to the experiments (symbols) in [29], [30], [2], and [31].

first requires a reliable estimation of the electric field profiles. The same doping concentration and geometrical structure for the p-i-n diodes reported in [29], [30], [2], and [31] have been reproduced with the Sentaurus TCAD [28] and the EBHD model has then been applied to them as postprocessing, taking as input the electric field from drift-diffusion TCAD simulations.

The good agreement at high gains validates the postprocessing approach, indicating that the generated charge has little impact on the electric field profile. Figure 2.4 compares the model results with the measured gain as a function of bias and with the measured excess noise as a function of gain. In both cases, good agreement between simulations and experiments is found over a wide range of intrinsic layer thicknesses with a unique set of material-dependent model parameters summarized in Table I, found in [22]. Figure 2.4 (right) shows that in GaAs and $\text{Al}_{0.2}\text{Ga}_{0.8}\text{As}$ the excess noise factor increases proportionally to the gain and that it is smaller for thinner intrinsic layers. As pointed out in [2], this behavior is in contrast with the predictions of a local model [32], but it is consistent with the measurements. In fact, when the extension of the intrinsic region becomes comparable to λ_e and λ_h (mean free paths), the ionization probability of the secondary carriers decreases, making the ionization process more deterministic.

The F versus M curves for $\text{Al}_{0.2}\text{Ga}_{0.8}\text{As}$ put in evidence a more complex nonmonotonic trend as a function of W ; in fact, when W decreases from 1024 to 312 nm, F increases for a given M , owing to the fact that at high electric field (as in short diodes) it approaches [6]. However, as W shortens, nonlocal effects come into play and reduce the value F as in GaAs and $\text{Al}_{0.2}\text{Ga}_{0.8}\text{As}$.

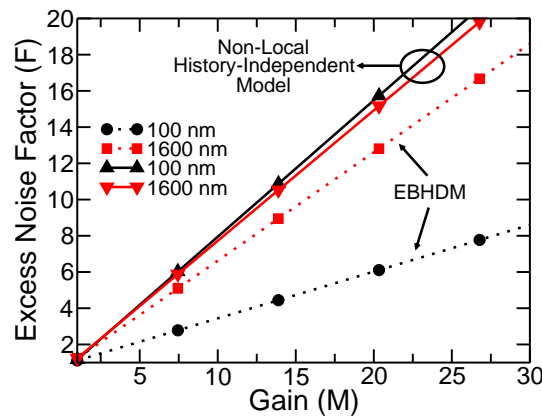


Figure 2.5: Excess noise as a function of the gain for the 100-nm- and the 1600-nm-thick GaAs p-i-n diodes described in [15]. The EBHDM described in Section II (dashed lines) is compared with the results obtained by using a nonlocal model that is history independent (solid lines).

It is worth mentioning that the good agreement between simulations and experiments from the literature for the excess noise versus gain

curve in Fig. 2.4 is a distinctive result of history-dependent models. In fact, a nonlocal history-independent model (remark 2.2) predicts that the excess noise versus gain curve only slightly depends on the thickness of the intrinsic layer.

The results (Fig. 2.5) are easily explained by observing that in this case the secondary carriers have the same ionization probability as the primary ones and this renders the ionization process more random compared with that of history-dependent models. The results of the nonlocal but history-independent model are thus close to the ones of a local model in terms of excess noise versus gain, while predictions for the gain versus voltage curves are different [26].

Remark 2.2: History dependent model

In the history independent model the ionization coefficients are expressed as a function of an effective field but at a given position all carriers have the same ionization probability regardless of the position where they were generated [26], [27] (α and β are function only of x and not from both x and x' , generation and ionization position, respectively). Thus, the coefficients depend on the complete electric field profile, but they do not differentiate according to the position where the carriers were generated. This can be demonstrated by setting $\alpha(x|x') = \alpha(0|x')$ and $\beta(x|x') = \beta(0|x')$ in the EBHD model, where 0 and W are the left and right end side boundaries of the simulation domain.

The application of the EBHD model on a staircase structure will be discussed in Chapter 5.

MATERIALS AND METHODS

The aim of this chapter is to describe the instruments and the techniques employed during this thesis to fabricate the devices. The first section is about molecular beam epitaxy, where the growth apparatus and the processes are described, while the second one focuses on the techniques utilized once the epitaxial processing is completed.

Furthermore, linked to this chapter is Appendix B, which gives an overview and some tips about the actual work carried out in the clean rooms.

3.1 MOLECULAR BEAM EPITAXY

Molecular Beam Epitaxy (MBE) is a ultra-high vacuum (UHV) deposition technique that allows the growth of thin epitaxial structures made of several materials, e.g. semiconductors, metals or insulators, thanks to its precise control of beam fluxes and growth conditions [33]. Moreover, owing to the extreme dimensional control and the low growth temperature it is possible to grow crystals layer-by-layer obtaining complex structures not available in nature [33], such as the staircase structure described in section 1.2.3.

3.1.1 MBE building blocks

A typical schematic arrangement of the growth chamber of an MBE system is shown in Fig. 3.1, where the main building blocks are presented and explained in detail throughout this section.

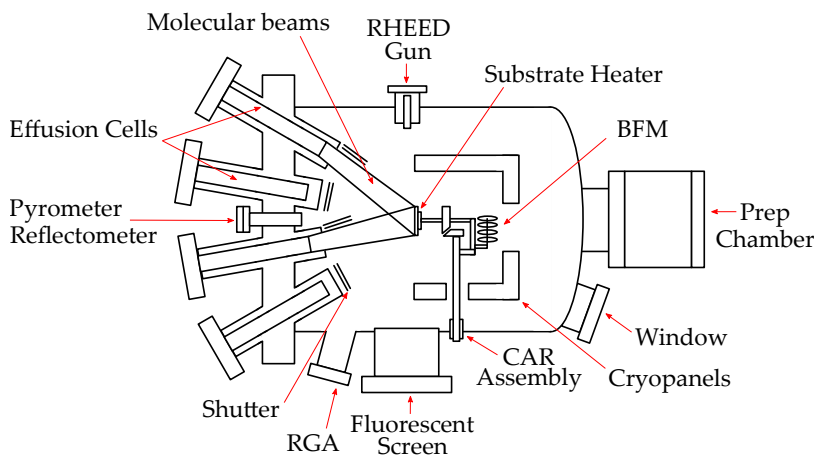


Figure 3.1: Schematic drawing of a generic MBE system.

Preparation chamber

Vacuum system The main chamber, which characterizes the growth system, is made from stainless steel, bolted together with CF flanges and pumped to a background pressure (after bake-out, which is necessary to minimize out-gassing from the internal walls [34]) in the UHV range [35]. The substrates are inserted in a load-lock module, which in turn is connected through UHV to a preparation chamber where the substrates are degassed before entering the main chamber. In fact, layer purity improves considerably with time, following the initial pump-down and bakeout, so it is of vital importance that substrates can be introduced into the machine without letting the system up to air [35]. Moreover, all the components that can be found inside there must resist for a long period of time at bake-out temperatures (up to 200 °C) [34].

Pumping system To ensure the purity of the deposited films the background pressure must be kept at such a level that the arrival rate of unwanted species on the substrate is much lower than those from the various effusion cells [35]. The pressure is maintained through a combination of ion, turbo-molecular, titanium sublimation and/or cryo pumps, which are able to reduce the base pressure to a range between 10^{-11} and 10^{-12} Torr, with the residual gas being basically H_2 . As an example, in order to grow crystals with an atomic density of about 10^{22} cm^{-3} the impurity concentration must be below 10^{15} cm^{-3} which is maintained with a pressure below 10^{-13} Torr [34].

Liquid N_2 cryopanel It is standard practice to surround the main chamber wall and the source flange with liquid-nitrogen-cooled cryopanel, which serve as thermal isolation, to remove heat from the system and to trap impurity species that might otherwise contaminate the growing film [34] and to prevent any cross-contamination between cells by wandering molecules, which condense on the panel rather than infiltrating other cells.

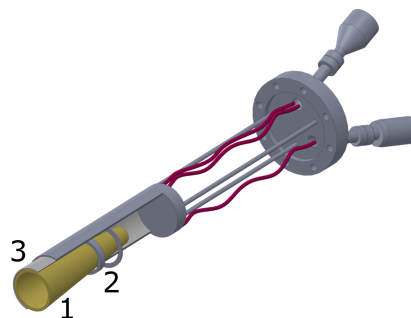


Figure 3.2: Schematic of an effusion cell, in which the main elements are marked: the crucible (1), the Ta filament (2), and the heat shielding (3).

Shutter

Effusion cells A set of effusion cells, each mounted on a source flange, supplied with a movable shutter (which can be used to inter-

rupt the flow of molecules to the substrate) provides molecular beams that must be characterized by an extremely stable and uniform flux and material purity. For these reasons the choice of materials to use and the geometry of the cells are crucial adding also to the fact that they have to endure really high temperature (up to 1400 °C) [34]. The most frequently used effusion cells are those of the Langmuir type, provided with a large orifice that allows lower temperature to be used for a given flux and thus reduces power consumption and thermal generation of impurities. The so-called cracker cells are used as well, which are a modified high-capacity version of the conventional effusion cells for the group V materials where the beam is directed from the crucible to the substrate through a higher-temperature cracker region [33]. A schematic drawing of a typical effusion cell can be observed in Fig. 3.2: the source material is held in condensed phase in an inert crucible (1) which is heated by radiation from a resistive heater. The crucible is usually made of pyrolytic boron nitride (PBN), which can withstand temperatures up to 1300 °C without appreciable degassing [34] and it takes different shapes (cylindrical or conical), sizes and tapering angles according to the material and applications. A thermocouple is used as control of the temperature, which in the cell is provided by a Ta filament (2) together with some Ta foils used as heat-shielding system (3).

Molecular beams

Substrate manipulator A key feature of any MBE machine is the substrate manipulator which, thanks to a continuous azimuth rotation (CAR), improves the growth uniformity across the wafer. This is necessary to smooth out non-uniformities due to the off-axis arrangement of the effusion cells which otherwise can vary spatially the growth rate [35]. Below the wafer holder it is equipped with a heater designed to maximize temperature uniformity, and to minimize power consumption and impurity outgassing [34]. On the manipulator a Mo or Ta substrate holder is mounted, where the wafers can be glued with gallium or clamped. On the other side of the holder there is an ionization gauge which is used as beam flux monitor (BFM) in order to calibrate the intensities of the molecular beams on a regular basis.

CAR

BFM

Analysis tools One important feature of the MBE film growth is the analysis tools that can be found in situ in the MBE chamber. The monitoring system typically comprises a mass spectrometer, a monitoring ionization gauge, a reflectometer, a pyrometer, and the Reflection High Energy Electron Diffraction (RHEED) system.

One of the most important growth parameters in MBE is the substrate temperature. Optical pyrometers are commonly used to measure substrate temperatures during growth as they are reliable and do not depend on the measurement geometry. However, there are some challenges implementing temperature measurements by pyrometry in

Pyrometer

Reflectometer MBE, as explained in [36]; therefore, alternatives to the standard pyrometer have been developed. These alternatives provide for built-in reflectometers that are used to measure the surface emissivity, the substrate temperature with an improved accuracy and the growth rates in-situ by analyzing the reflectivity signal. The reflectometer uses monochromatic diodes, which emit light with normal incidence and the change in the optical intensity of the reflected signal is monitored to give information about the growth of the thin film [36].

RHEED A complete grazing-incidence reflection electron-diffraction system can also be available inside the chamber. The RHEED (Reflection High-Energy Electron Diffraction) system is one of the most common and useful in-situ metrology tools used in MBE. It can be used to characterize the structural information of the substrate (as the crystalline structure, quality and chemical composition of surfaces) and to measure growth rates, to calibrate surface temperatures and to characterize V/III flux ratios [36]. The RHEED is sited a few degrees off the sample surface, to avoid physical interference with the effusion cells and to maximize surface sensitivity thanks to the grazing incidence. Full surface geometry is determined by rotating the sample at different azimuth angles. The RHEED diffraction pattern generated by the sample surface is displayed on a phosphor screen specularly located from the gun with respect to the substrate. This pattern may be evaluated and further processed in a specially designed optoelectronic system [33]. More details on this tool are going to be mentioned in section 3.1.2.

Fluorescent screen

RGA Another in situ tool is the quadrupole residual gas analyzer (RGA), which is a mass spectrometer that allows the analyses of the residual gas composition in the chamber. This tool is also used for leak-testing the vacuum system through helium detection.

3.1.1.1 HMMBE system at IOM-CNR

The High Mobility Molecular Beam Epitaxy (HMMBE) installed at IOM-CNR in Trieste, Italy, is a facility dedicated to the growth of high-purity III-V semiconductors in UHV with atomic layer control on compositions and thicknesses, characterized by a very high carrier mobility, which can be viewed in Fig. 3.3.

To achieve the high-mobility environment some peculiar modifications with respect to a classic MBE system are necessary. In Trieste, in particular, two 3000 L s⁻¹ cryopumps replaced the ion pumps, providing a cleaner, higher-capacity pumping system. All-metal gate valves were mounted instead of the Viton seals to eliminate outgassing. No group-II materials, such as Be, are employed for p-doping, since they are known to drastically reduce carrier mobility; a carbon source was installed as p-doping source instead. High-capacity and duplicate cells (for gallium and arsenic) were installed to avoid cell refilling or



Figure 3.3: High Mobility MBE at IOM-CNR at Trieste.

repairing for extended periods. In fact, once installed an extensive degassing and bake-out of the duration of three months (at 200 °C) was carried out to increase the purity of the materials.

The model of the MBE in question is a *Veeco Gen II* machine with a dedicated design for high mobility. It is equipped with different effusion cells whose materials are As, Ga, Al, In and two doping sources, Si and C, for growth on 2" GaAs wafers. Grown structures range from high mobility two-dimensional electron systems in GaAs/Al-GaAs (with mobilities up to $8.6 \cdot 10^6 \text{ cm V}^{-2} \text{ s}^{-1}$) and metamorphic $\text{In}_{0.75}\text{Ga}_{0.25}\text{As}/\text{In}_{0.75}\text{Al}_{0.25}\text{As}$ heterostructures, to photonic structures and self-assembled nanostructures.

The facility is completed by a variable temperature magneto-transport equipment for electrical characterization (whose temperature varies in the range of 1.5 K and 400 K and whose magnetic field can reach up to 7 T).

3.1.2 MBE growth process

Molecular beam epitaxy is a versatile technique for growing thin epitaxial structures. The essential elements of the growth system can be distinguished in three different phases: the generation of the molecular beams from the effusion cells, characterized by a disordered gas phase; the crystalline phase constituted by the growing substrate; and the zone proximate to the substrate where the beams intersect and the vaporized elements mix [33].

This last zone, which is the near-surface transition layer is where the phenomena that interest the most the MBE process take place. It has to

be considered that, in MBE, the pressure of the residual gas and that of the molecular beams are so low that the mean free path for molecule collision is much larger than the source-to-substrate distance. Thus MBE fluxes can be considered as ballistic events and no homogeneous reactions in the gas phase can occur [34].

Atomic or molecular species impinging perpendicularly on the surface get physisorbed or chemisorbed on it, and the process is characterized by different required energies. Furthermore, a series of surface processes are involved in MBE growth, and the most important are reported hereinafter [33]:

- (a) adsorption of the constituent atoms or molecules impinging on the substrate surface;
- (b) surface migration of the adsorbed molecules (which can then diffuse);
- (c) dissociation of the adsorbed molecules;
- (d) incorporation of the constituent atoms into the crystal lattice of the substrate or the epilayer already grown (they meet other atoms and thus form a cluster);
- (e) thermal desorption of the species not incorporated into the crystal lattice (they can re-evaporate).

The energetics of these events, their time and length scale depends on a number of factors, like the surface roughness or its crystallographic orientation, the temperature, and the gas phase composition.

Moreover, the case of deposition of a specific material onto a substrate of different material has to be considered, taking into account lattice mismatch. The strain energy due to the difference in lattice spacing is an increasing function of the growth thickness [34]; when a critical thickness is reached, the strain energy is relaxed through formation of dislocations or three-dimensional islands. This latter phenomenon can be observed for InGaAs/GaAs if not grown with the opportune conditions, as it will be shown in Ch. 5.

3.1.3 Growth rate calibration

To grow ternary alloys as $\text{In}_x\text{Ga}_{1-x}\text{As}$ and $\text{Al}_x\text{Ga}_{1-x}\text{As}$ with well defined thickness and concentration x , one must know accurately, prior to growth, the growth rates R_{GaAs} , R_{AlAs} and R_{InAs} .

In case of $\text{Al}_x\text{Ga}_{1-x}\text{As}$, the two growth rates (R_{GaAs} and R_{AlAs}) are calibrated either by RHEED or reflectometry; while in case of $\text{In}_x\text{Ga}_{1-x}\text{As}$, the growth rate R_{InAs} cannot be measured through RHEED or reflectometry because of the large lattice mismatch, thus it is obtained by measuring x through X-ray diffraction from a 1- μm -thick InGaAs layer and knowing R_{GaAs} .

As the depositions of the above mentioned materials are not competitive processes, in the former case it is possible to calculate the concentration as

$$x = \frac{R_{AlAs}}{R_{AlAs} + R_{GaAs}}. \quad (3.1)$$

In the latter R_{InAs} can be calculated from

$$x = \frac{R_{InAs}}{R_{InAs} + R_{GaAs}}. \quad (3.2)$$

The calibration of the MBE growth rates is performed almost daily, prior to sample growth, on an ad-hoc substrate. The day-to-day variation of R_{GaAs} and R_{AlAs} , with constant cell temperatures is $\approx 1\%$; the long term behavior of these rates, on the other hand is fairly predictable and it is constant until the cell is almost empty, unless major changes to the cell environment happen (like refilling, etc).

RHEED

The growth rates R_{AlAs} and R_{GaAs} are calibrated and measured by the intensity oscillations of the specular spot of the RHEED signal during the growth of a AlAs or GaAs film on a GaAs substrate, respectively.

This technique employs an electron gun that produces a collimated beam of electrons, with energies ranging between 10 keV and 50 keV, directed on the growing surface of the sample at grazing incidence, and eventually impinging on a fluorescent screen where the diffraction patterns [36] are displayed and then acquired by a CCD. Thanks to the grazing incidence and the limited mean free path of electrons in solids, the electron beam is scattered only by the very first atomic layers, giving rise to a surface-sensitive diffraction pattern. Therefore, the RHEED can provide information about the flatness of the surface and additional information about the surface geometry and chemistry, both in static conditions and during growth, as the streaks which appear in the diffraction pattern vary with the bulk lattice periodicity [34].

The principle upon which this technique relies is the Laue law, which states that wavevectors of diffracted beams are determined by the intersection of reciprocal lattice lines or points with the Ewald sphere [36]. Figure 3.4 shows a schematic representation of the origin of RHEED diffraction patterns from atomically rough and smooth surfaces. These surfaces are characterized by reciprocal lattices given by spots 3.4a and rods 3.4b, respectively [36]. As it can be seen, the intersections of the Ewald sphere with the features of the reciprocal lattice define diffracted spots and streaks that are then visualized on the fluorescent screen: if the surface is not flat many electrons will be scattered in different directions and the pattern will be constituted by many spotty features; otherwise, if the electrons interact with a perfectly flat and ordered surface the points will degenerate into

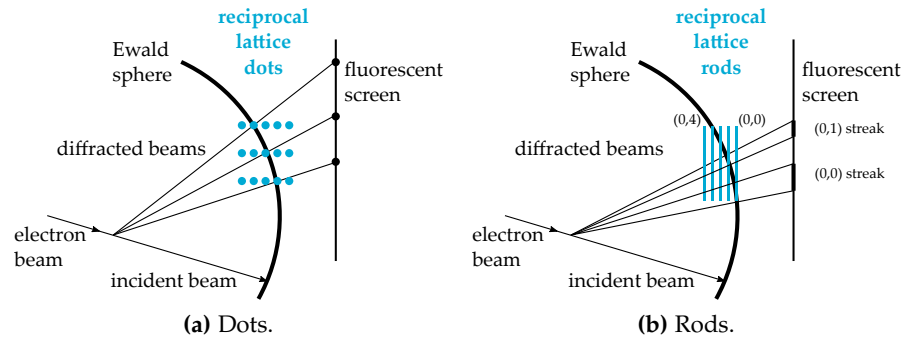


Figure 3.4: Schematic representation of the origin of RHEED diffraction patterns: (a) from atomically rough surfaces and (b) from smooth ones (just a few of which are sketched). The intersections of the Ewald sphere with the features of the reciprocal lattice define diffracted spots and streaks visualized on the fluorescent screen [36].

parallel infinite rods [36]. An example of diffraction pattern, taken at two perpendicular azimuths, of a flat, epitaxially grown (100) and (010) GaAs surface is shown in Fig. 3.5 [34].

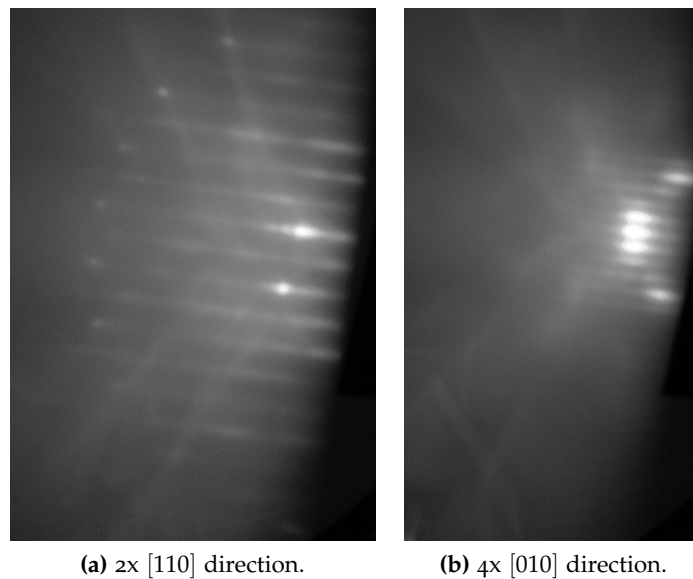


Figure 3.5: 2x and 4x diffraction patterns from a (2x4)-reconstructed (001) GaAs surface [34].

As the RHEED intensity signal is acquired during crystal growth (an example of such measurements is shown on the right panel of Fig. 3.6) it can be noted that the amplitude of the signal initially decreases with respect to the static conditions and it starts to oscillate periodically with a damped intensity until the shutters are closed again. This happens because a flat surface, present when a monolayer is complete, reflects perfectly the electrons while in a condition in which a half-monolayer has been deposited the electron beam gets

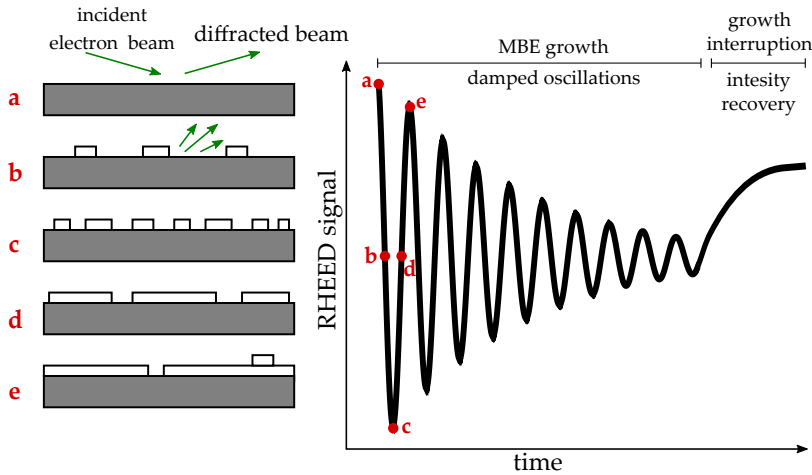


Figure 3.6: Growth mechanism with corresponding RHEED intensity oscillations as a function of growth time. The periodic variation of concentration of surface steps influences the intensity of the oscillations. In fact, the steps behave as scattering centers for incident electrons [36].

partially scattered by the stepped surface. As schematically shown by Fig. 3.6, initially the electron beam is scattered only by the first flat surface, where the reflections of the electrons are optimal (Fig. 3.6a); instead, while the layer is being deposited the electron beam gets partially scattered by the rough surface (Fig. 3.6b). Then again as the layer grows the reflected intensity is reduced. Scattering is maximized at half coverage (Fig. 3.6c) and then the reflected intensity recovers its value as the monolayer grows as a flat surface (Fig. 3.6d- 3.6e). A progressive dumping of the oscillation intensity is due to an increasing disorder of the growth front as the growth proceeds.

The period with which this intensity changes gives information on the growth rate and it allows daily calibration [34]. Furthermore, the intensity oscillation depends on the periodic variation of the concentration of surface steps that behave as scattering centers for incident electrons as it can be seen in Fig. 3.6 [36]. In fact, a period of RHEED oscillation corresponds to the growth of one single layer. By measuring the time necessary to complete a certain number of oscillations one can calculate the growth rate in monolayer/s for a fixed effusion cell temperature, and easily convert in Å/s knowing the lattice parameter of GaAs or AlAs.

Reflectometry

Reflectometry is a real-time monitoring technique which monitors the interference of a monochromatic optical beam between the growing surface and a buried interface. This technique becomes reliable for layer thicknesses greater than $\lambda/4$, where λ is the monitoring wavelength [37], a value much thicker than typical thicknesses of RHEED oscillations (a few to a few tens of monolayers). This makes the former

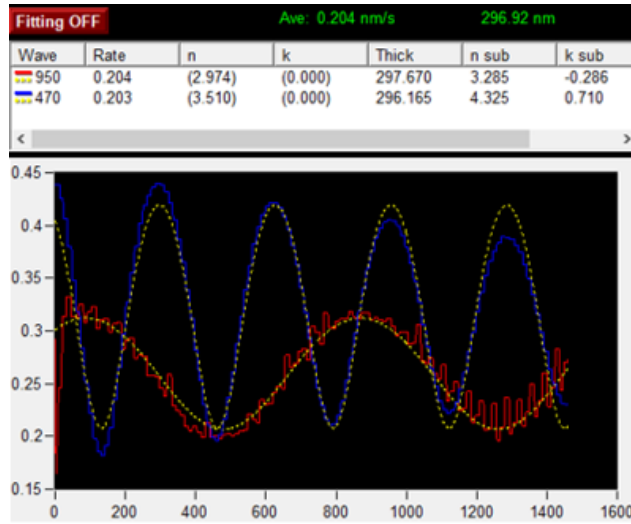


Figure 3.7: A reflectivity measurement with two different wavelengths for thickness control ($\lambda_1 = 950$ nm in red and $\lambda_1 = 470$ nm in blue) as a function of the time in seconds.

much less sensitive to statistical fluctuations and to flux transients and thus more precise. Additionally, reflectivity probes a larger spot size than RHEED (about a cm in diameter) and can be used during sample rotation making it less sensitive to spatial flux variations.

The period of oscillation, amplitude, phase and damping characteristics of the reflectance data depend on the film index of refraction and can be monitored through growth-rate fitting software procedures by fitting to a multi-parameter analytical model [38].

Semiconductor substrates are not opaque at all wavelengths, so it is critical to choose a measurement wavelength at which the substrate is opaque. During the film growth, the optical reflectance was monitored at 470 nm and 950 nm. The period of oscillation, P , is proportional to the film index of refraction, n , and the growth rate, G , by the expression:

$$P = \frac{2nG}{\lambda}. \quad (3.3)$$

Since the measurement wavelength, λ , is known, the product of n and G is found from fitting the oscillations to a theoretical model, which takes into account the sinusoidal interference with period P and the signal dumping through the overlayer. The index of refraction is calibrated once for all for GaAs and AlAs at the growth temperatures by X-ray diffraction on dedicated superlattice samples; thus the growth rate is calculated from the oscillation period. The growth rate is measured in real time by fitting the oscillating reflectance information to an analytical model [39].

3.2 FABRICATION TECHNIQUES

This section is focused on the principles of the main techniques utilized during fabrication. The presented tools are all available in the clean rooms at CNR-IOM, in Trieste.

3.2.1 *Spin coater*

To create the structures of the devices on a specific wafer a certain pattern has to be transferred onto it. This is accomplished by applying a photoresist on the wafer with a process called spin coating [40]. The resist has to be reliable, thus it has to stick to the substrate, to spread uniformly and its thickness has to be reproducible under the same conditions [40]. The process starts by applying a small amount of resist on the wafer, held with a vacuum system to the spindle and then spinning it at a rate of 2000-8000 rpm for a certain amount of time (usually between 10 and 60 s). Due to the centrifugal force most of the resist hurls off during the spinning and it has to be considered that the remaining thin layer (whose thickness is controlled by the spin speed which can be set) is characterized by a thicker edge bead. The resist, once applied, has to be baked to improve adhesion to the material [40].

3.2.2 *Lithography*

Lithography is a technique that allows to transfer copies of an optical image onto the surface of a solid material. The most widely used form is photolithography [41]. During this process the resist which has been previously deposited, is exposed under a UV light through a mask, for a certain exposure time. An example of the mask can be found in Appendix B.1.2. The mask is then transferred to the photoresist which once developed in a solvent that melts away the portions characterized by a higher solubility [40] can be further processed.

The photoresist is mainly made of a polymer, a sensitizer (resist without it are called single-component) and a casting solvent. Each component has its specific function: the polymer changes structures when exposed under illumination; the solvent allows the resist to be spun; the sensitizers control the photochemical reactions in the polymeric phase. [41].

Photoresist Two types of resist can be identified: the positive one, that becomes more soluble when exposed to illumination as the photochemical reaction weakens the polymer [41] and the negative one, where the polymer becomes stronger after the exposure [41] losing its solubility [40]. Accordingly to these different types of resist the process can undergo two different paths, as highlighted in Fig. 3.8.

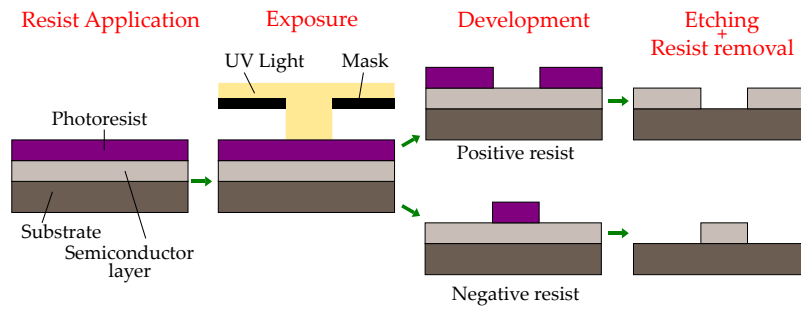


Figure 3.8: Schematic representation of a generalized positive and negative resist processes :exposure, development, and pattern transfer. Positive resists develop in the exposed region. Negative resists remain in the exposed region.

It is very important to underline that the resist must be proved to have high sensitivity and present a high resistance to etchants. The photoresist which has been used during this thesis work belongs to the S1800 Series and it is a positive photoresist, optimized for use with the MF-319 metal-ion-free developer family. It has to be soft baked at 115 °C for 60 s [42].

Lift-off resist The lift-off resist (LOR), in contrast to the above-mentioned photoresist, is not a photo-sensitive resist. That means that after baking, exposed and not exposed areas have the same dissolution rate, allowing bi-layer techniques to be applied by the control of the so-called undercut.

The LOR used in combination with conventional photoresists can be used to perform a subsequent deposition of a layer, such as a metalization layer, which is meant to cover just a particular portion of the structure in a process that takes advantage of the creation of an undercut.

The LOR 3B used during the thesis was baked at 180 °C for 5 min on a hot plate.

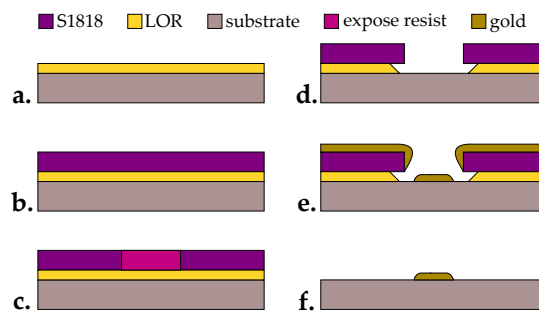


Figure 3.9: Lift-off process [43]. The substrate is covered with the LOR (a) and the photoresist (b), then the latter is exposed under the UV light (c) and developed (d). On the resulting structure a film of the desired material is deposited (e). Thanks to the under cut the material which is not necessary can be removed (f).

The process known as lift-off process consists of the steps highlighted in Fig. 3.9: firstly the substrate is coated with the LOR and prebaked, then the imaging resist is spun and baked; after the expo-

sure through the mask, the whole structure is developed. As the LOR develops isotropically creating a bi-layer re-entrant sidewall profile, the subsequent deposition of a film will present a discontinuity which allows for the lift-off of the bi-layer resist stack [43]. As highlighted, the discontinuity in the deposited metal is necessary so that the solvent can reach and remove the uncoated resist wall.

3.2.2.1 Resolution and minimum feature size

During the transfer from the mask to the sample the correct feature sizes must be preserved as the performances of the fabricated devices depend upon them [41]. To measure the resolution of a lithographic process one must refer to the critical dimension, which is the minimum feature size that can be obtained during the transfer, which is usually also the minimum resolved dimension of a line or a space.

In the case of contact printing the chosen photomask is pressed against the wafer, which is coated with the photoresist. However, the transfer of a perfectly delineated edge becomes blurred or diffused owing to the diffraction of light at the edge of the opaque features found in the masks. The theoretical resolution R with a grating mask thus is given by:

$$R = \frac{3}{2} \sqrt{\frac{\lambda z}{2}} \quad (3.4)$$

where λ is the wavelength of the exposing radiation and z is the photoresist thickness [41]. From equation 3.4 it is clear that in order to achieve a higher resolution one must use shorter wavelengths and thinner resist layers. However, there are different factors which do not allow the theoretical resolution to be reached (e.g. wafer flatness, mask alignment) [41].

The mask aligner used at the IOM-CNR facility in Trieste is a Karl Süss MJB 3 mask aligner whose UV radiation for exposure works with a Hg i-line at a wavelength equal to 365 nm. With λ of 365 nm and a 1- μm -thick resist a theoretical resolution of approximately 1 μm is possible with this machinery.

Lithography is the precursor of either subtractive processes, where the materials are removed (section 3.2.3) and additive processes where materials are somehow added (section 3.2.4).

3.2.3 Etching

Some of the main techniques used to remove materials from the wafer include wet and dry etching. The etching of solid surfaces can occur physically by bombarding it with ions or chemically through reactive species.

3.2.3.1 *Wet chemical etching*

During the wet chemical etching the wafer is soaked in a liquid chemical solution that dissolves away the semiconductor. This technique is the one employed, for example, after photolithography in order to create the designed structures. The etching process involves a chemical reaction in which the etching solution reacts with the elements of the layer that has to be etched. The etching rate is proportional to the etching time and it is usually isotropic, thus such technique is not able to produce sharp sidewalls. Furthermore, the etching rate depends upon the concentration of the chemicals involved in the etchant and the temperature of the solution [40].

3.2.3.2 *Dry etching*

During this work the dry etching technique has been employed to clean the surfaces of the structure before metal deposition, in order to achieve the best adhesion possible. This process has been carried on both through reactive ion etching and sputtering. In principle, this technique allows a more precise etching size with respect to the wet-etching one and, furthermore, it allows to etch materials that are not etchable by wet chemicals.

Reactive ion etching The Reactive Ion Etching (RIE) is a tool that can be used both for ion-implantation and for etching purposes [40]. A RIE machine consists of a chamber where a plasma is produced by passing an RF electrical discharge through a gas at a low pressure that creates ions and electrons. Inside the chamber the sample is placed on an electrode, which attracts gas ions achieving a ionic bombardment capable of etching or milling the structure. The interaction happens as the ions are accelerated in a controlled way by the electric field and if the ion energy is large enough the ions simply sputter off atoms from the surface in a rather unselective manner. [40].

3.2.4 *Metal evaporation*

Many thin films can be deposited through evaporation; an example is Physical Vapor Deposition (PVD) characterized by low pressure environment where the vaporized materials encounter just few intermolecular collisions while traveling towards the substrate [41].

The principle on which it is based is the boiling off or the sublimation of materials, which are heated in vacuum (less than 10^{-5} Torr [41]) in order to prevent the creation of contaminated layers.

The evaporation carried on in the IOM-CNR clean room is an electron-beam (e-beam) evaporation. The e-beam evaporator is equipped with a high-intensity electron beam gun (3 to 20 keV), which is focused

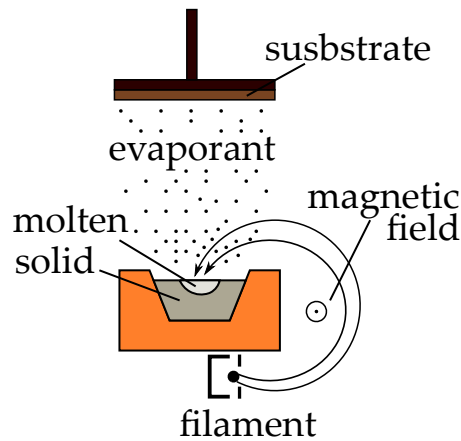


Figure 3.10: Schematic of an e-beam evaporator.

on the target material placed inside a crucible placed in turn into a water-cooled copper heart. It is cooled down so that fewer source-contamination problems can be registered. As shown in Fig. 3.10 the electron beam is magnetically directed to the material which is locally molten. This mode of operation results in higher-quality films and higher deposition rates [41].

3.2.5 Profilometer

The profilometer is an instrument used to measure the profile of surfaces. It works through a stylus, normally made of diamond, which is always in contact with the sample. The distance and the contact force must be specified prior to the measurement; later the information about the surface morphology is digitized and displayed.

The one available at IOM-CNR features a measurement range of some microns with a resolution of the order of nanometers. During this thesis work, it was employed to measure the etching depth of all the different devices which were fabricated.

3.2.6 Bonding machine

This instrument is used to create electrical connections in microelectronic devices. The machine utilizes a 25- μm wire, which is normally made of Al or Au that runs through the eye of a needle, as Fig. 3.11a shows. In the case of aluminum the bonding can be performed at room temperature, while a temperature of 120 °C is advised if working with gold filament.

The two pads of interest are bonded by setting some parameters. The main ones are the electric power delivered, the contact force and the time, in order to optimize the bonding as a function of material, thickness and substrate.

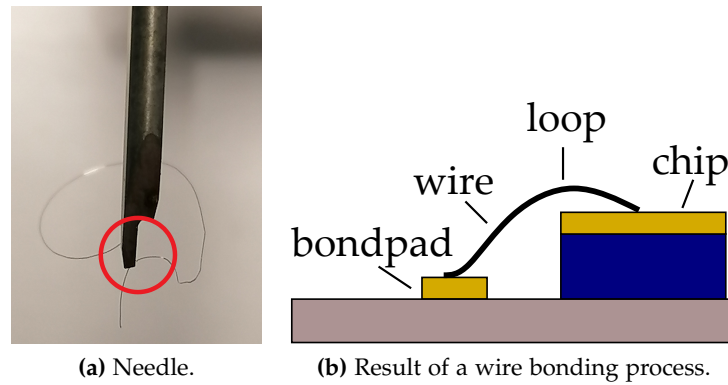


Figure 3.11: Wire bonding. (a) Needle of the wire bonding tool, where its eye is highlighted in red. (b) Schematic of the result of the process.

The procedure for making an ultrasonic-wire bond between two points requires to lower the tool to its first “search” position. The tool is then further lowered and it presses the wire against the bonding surface with a predetermined force. Ultrasonic energy is applied for a preset time to make the first bond. Then, the tool is raised while the wire is paid out from the spool of wire and, while the work holder moves toward the second bonding site, a loop is formed. Again, the tool is lowered to its second search position, onto the bonding pad, and the second bond is made, as initially. As the second bond is made a wire clamp closes and pulls back on the wire which breaks near the bond. The needle raises and the end of the wire is fed out underneath the tool until the end is located somewhat beyond the front of the tool (the “tail” length). The bonder is then ready to repeat this cycle [44]. The result is schematically shown in Fig. 3.11b.

3.3 REALIZATION OF THE DEVICES UNDER STUDY

This section is dedicated to the description of the processes actually employed to obtain the devices under study. These include the growth of the structures, using an MBE apparatus, the subsequent fabrication of the mesas and finally, placing and bonding the dice to the printed circuit board (PCB), through which it is possible to bias the devices and to read the output signals.

3.3.1 Wafer growth

The devices under investigation were grown epitaxially onto 2-inch n-doped GaAs wafers by using MBE. The utilized structure is a separated absorption and multiplication region, thus the name Separate Absorption and Multiplication APD (SAM-APD); as described in 2.1.1, this structure exhibits a better signal-to-noise ratio with respect to APDs in which this feature is not present.

Material	Dopant	Dopant type	Thickness (nm)	Doping density
GaAs	C	p	150	$6 \cdot 10^{18} \text{ cm}^{-3}$
GaAs			4500	
δ layer	C	p		$2.5 \cdot 10^{12} \text{ cm}^{-2}$
GaAs			35	
$\text{Al}_x\text{Ga}_{1-x}\text{As}$			20	
AlGaAs			25	
GaAs			35	
GaAs	Si	n	100	$2 \cdot 10^{18} \text{ cm}^{-3}$

Table 3.1: Layers of the SAM-APD structure from which the devices were fabricated. The gray part highlights a single step of the multiplication region. In most of the devices this is repeated 12 times. Devices with a different number of steps (6 or 24) were also fabricated.

The first structures were grown accordingly to Table 3.1, where the gray part represents a single step of the multiplication region which can be repeated n times. A sketch of such device is shown schematically in Fig. 3.12a and 3.12b. The modifications of the original structure carried on during the thesis are presented and described in Ch. 5.

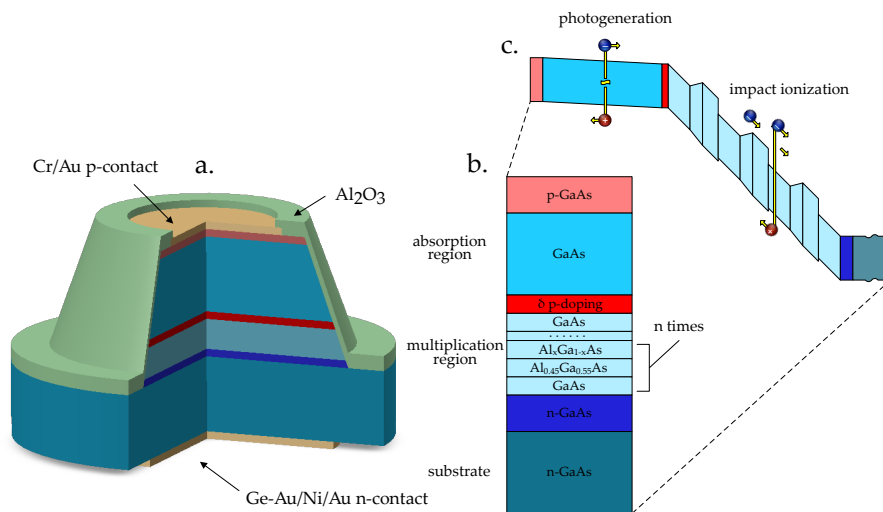


Figure 3.12: (a) Sketch of the fabricated avalanche photodiode with separated absorption and multiplication regions. (b) Scheme of the structure grown by MBE. (c) Band diagram under reverse bias. Image courtesy of Dr. Matias Antonelli.

After the deposition of a 100-nm-thick highly n-doped buffer layer (concentration $2 \cdot 10^{18} \text{ cm}^{-3}$) onto a (001) n-substrate, an intrinsic multiplication layer was grown. This layer includes a staircase structure with a given number of stages (repetitions) and it represents the multiplication region. Each stage consists of 35 nm of GaAs, 25 nm of

$\text{Al}_{0.45}\text{Ga}_{0.55}\text{As}$ and 20 nm of a linearly graded region where the aluminum content is reduced from 45% to 0%. Devices with 12 steps were grown originally following the protocol described in [4]. Later devices with a different number of repetition, 6 and 24 steps respectively, were fabricated, too.

In principle, the graded composition $\text{Al}_x\text{Ga}_{1-x}\text{As}$ layer requires a continuous linear gradient of either or both the alloy materials, gallium or aluminum. However, this is not practically achievable in MBE, thus a digital alloy was introduced. The digital alloy which was utilized consists of thin layers of GaAs alternating to $\text{Al}_{0.45}\text{Ga}_{0.55}\text{As}$. The thickness of each bilayer is constant (15.38 Å), while the thickness ratio between GaAs and AlGaAs varies in order to decrease the average composition from 0.45 to 0. Since the thicknesses are smaller with respect to the mean free path of electrons, these carriers interact with the potential of the digital alloy as if it were a constant gradient. The actual concentration is depicted in Fig. 3.13 in gray, while the effective concentration appears in red and it is a representation of how electrons perceive the variation of Al.

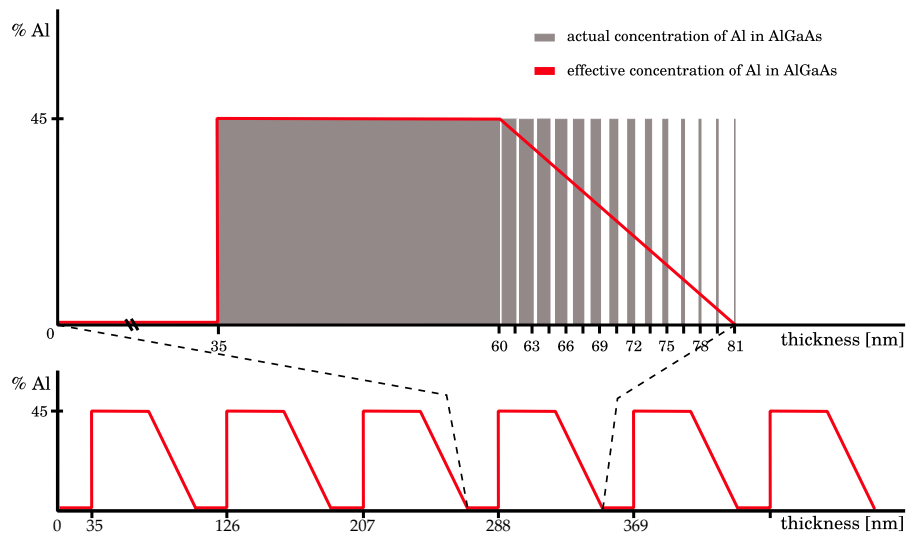


Figure 3.13: Aluminum concentration profile of a portion of the staircase structure (bottom) and detail of a single step (top). The actual concentration is depicted in gray, while the effective concentration appears in red. The latter is a representation of how electrons perceive the variation of Al. Image courtesy of Dr. Tereza Steinhartova.

Above the staircase structure, a 35-nm-thick GaAs spacer was grown, followed by a δ p-doped layer of carbon atoms. Such layer ensures that after applying a reverse bias the vast majority of the voltage drops across the multiplication region (illustrated in Fig. 3.12c). Also in this case, different doping concentration were used and the results are reported in Ch. 5. On top of the δ layer, an intrinsic GaAs absorption layer was deposited. Its thickness is 4.5 μm in the prototype sample[45], but samples with different absorption-region length were

also grown (i.e. 300 nm and 15 μm). Finally, the sample was capped with a 200-nm highly p-doped ($6 \cdot 10^{18} \text{ cm}^{-3}$) GaAs contact layer.

Thickness, composition and uniformity verification After growth, different methods, i.e. X-ray diffraction and hall measurements, were used to assess the thickness, the composition and the uniformity of the MBE-grown layers.

X-ray diffraction rocking curve measurements reveals the broadening of the diffraction peaks; the increase in the peak widths may be caused by misorientation of the crystal lattice, strain or limited layer thickness. Figure 3.14 (red trace) shows the (004) rocking curve of a SAM-APD sample as described in Table 3.1, which was measured with a high resolution x-ray diffractometer equipped with a four-crystal Ge (220) monochromator using Cu- K_{α_1} radiation. The appearance of sharp superlattice interference fringes up to high order confirms the thickness uniformity and interface quality of our layers. An analysis of fringe spacing and of the average alloy composition over a single step gives a step thickness of $80 \pm 1 \text{ nm}$ and $x \approx 0.47$ for this particular sample.

X-ray diffraction

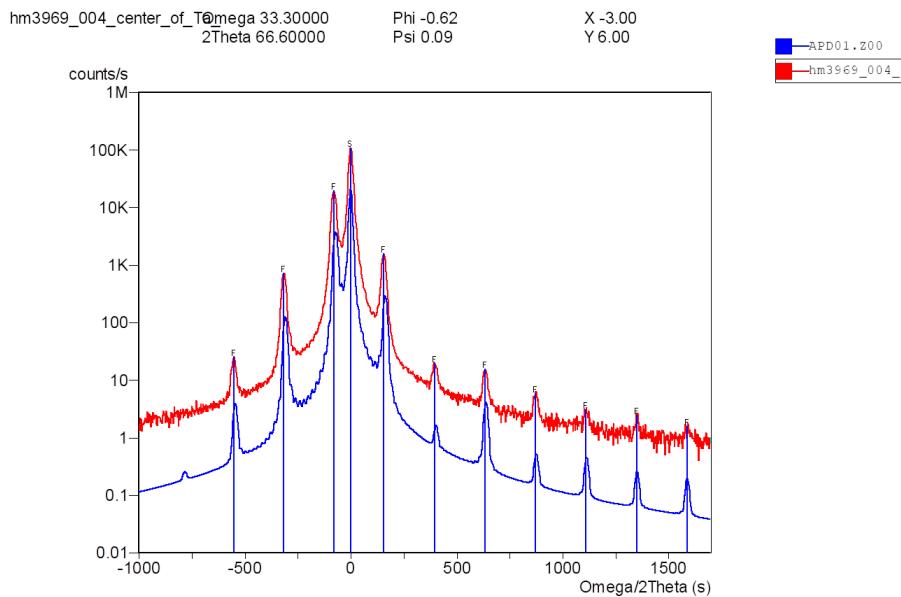


Figure 3.14: XRD spectra of a SAM-APD structure grown on a (001) GaAs n-doped substrate having a multiplication region of 12 steps. The red curve represents the data measured by the diffractometer, while the blue curve is a simulation.

Hall measurements were performed to calibrate the effective acceptor density in the p layer separating the absorption and the multiplication regions. In order to do so, the free carrier concentration was measured at room temperature in a series of GaAs bulk sample where either a δ or a 50-nanometer p-doped GaAs layer was inserted with different planar densities of C atoms.

Hall measurements

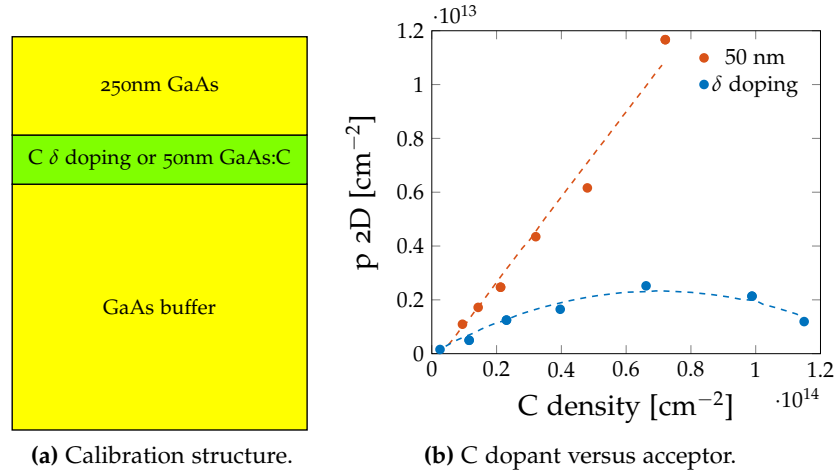


Figure 3.15: The structure utilized to calibrate the p-doping density (a) C acceptor density as a function of the 2D-density of carbon deposited atoms (b). The dashed lines are plotted to guide the eye in visualizing the trend of the plotted data.

The different concentration is obtained by varying the current through the graphite filament in the carbon sublimation source during the growth. In particular, the δ p-doped layer is a 2D sheet of C atoms deposited during a growth interruption of the host GaAs material.

The planar density expresses the actual 2D density in case of a δ separation layer, while in the case of a finite thickness layer, it is calculated as an integral of density over the thickness. For example a 50-nm-thick layer of C-doped GaAs with acceptor density $5 \cdot 10^{17} \text{ cm}^{-3}$ possesses a planar density of $2.5 \cdot 10^{12} \text{ cm}^{-2}$.

Figure 3.15 shows how δ p-doped C layers are highly compensated (meaning that not all C atoms end up on arsenic sites but also on gallium ones becoming donors), likely owing to atomic pairing as suggested in [46]. In fact, even though carbon has a lower diffusion coefficient and higher solubility with respect to other materials in use (e.g. beryllium) [46], the carbon density (x-axis) and the actual acceptor planar density (y-axis) are not in a one to one ratio; the actual acceptor density is lower than the amount of C delivered by the effusion cell. Compensation takes place in the thin GaAs:C layers as well, although to a lesser extent. The maximum planar achievable acceptor densities in δ p-doped C layers and in the thin (50 nm) GaAs:C layers were $2.5 \cdot 10^{12} \text{ cm}^{-2}$ and $1.2 \cdot 10^{13} \text{ cm}^{-2}$, respectively (Fig. 3.15). In the same plot it can be seen that in the δ doping case, the dopant concentration p drops below its maximum value as the source current is further increased. Therefore, as it was not possible to study the effect of higher concentration of dopant with the δ layer, the 50-nm-thick layer was used instead above $2.5 \cdot 10^{12}$.

3.3.2 Device fabrication

The device fabrication procedure, starting from the epitaxial wafers, is composed of different phases and processes, whose mode of operation have been explained in section 3.2.

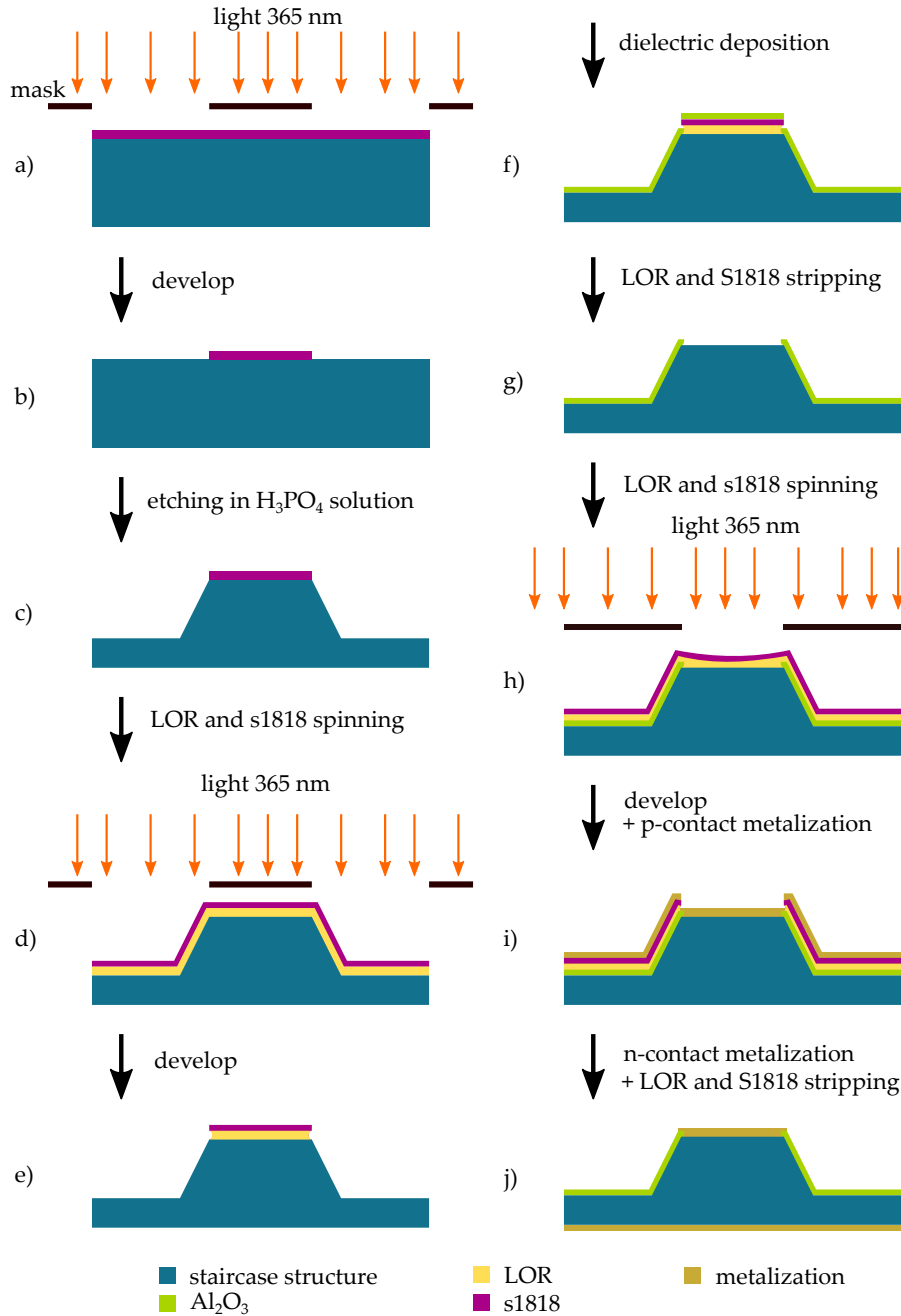


Figure 3.16: The main steps performed during fabrication.

A step-by-step detailed explanation of the procedure employed in the clean rooms at the IOM-CNR facility in Trieste (which are class ISO 3 clean rooms, meaning a maximum of $1000 \text{ particles} \cdot \text{m}^{-3}$) can

be found in appendix B. In the following, the main fabrication phases are highlighted.

A summary of the steps taken during the fabrication is shown in Fig. 3.16. The main steps depicted are the mesa lithography (a-b) which precedes the etching of the mesa (c), a further lithography used for the deposition of the dielectric layer (d-e-f-g), followed by the lift-off procedure to create the p-contact (h-i) and the final deposition of the n-contact (j).

Mesa lithography As highlighted in Fig. 3.16 the first step to fabricate our devices consists in preparing the mesas (Fig. 3.16c) through the photolithographic process, the fundamental of which is described in section 3.2.2.

The sample was placed in the spinning hood: firstly it had to be cleansed with acetone, isopropanol and then dried using pressured nitrogen. Once this was done, it was coated with a layer of positive photoresist S1818. In order to do so, the thermalized S1818 (at room temperature) was applied as an homogeneous layer to the clean surface by a Pasteur pipette. The sample was spun for 1 minute, setting a rotation speed of 2500 rpm and a rotation acceleration factor of 6. These values were chosen in order to obtain a final thickness of 2 μm . The resist was then soft baked-out on a hotplate heated up to 115 $^{\circ}\text{C}$ for 1 minute [42].

The resist coating was then exposed for 15 s through a photomask using a mask aligner with a mercury I-line at 365 nm (Fig. 3.16a). Several masks were designed. In order to thoroughly understand the devices' characteristics, the GaAs APDs were initially manufactured in different sizes (mesa diameter of 200 μm , 400 μm , 600 μm and 800 μm). However, as it will be clear in Ch. 5, the attention was aimed at the ones with the lowest capacitance; thus, mostly 200- μm -diameter devices were fabricated. The resist was then developed in MF-322, which will remove all parts that had not been illuminated (Fig. 3.16b), as the S1818 is a positive resist.

Mesa etching The etching process begins with the preparation of the etching solution: $\text{H}_3\text{PO}_4:\text{H}_2\text{O}_2:\text{H}_2\text{O}$ (3:1:50). The sample was submerged in it for a certain amount of time considering the etching rate, which was approximately 100 nm/min (Fig. 3.16c). However, there are different factors that can influence the velocity with which this process develops, i.e. the temperature and the concentration of the stored H_2O_2 . For this reason, a calibration of etching rate should be performed each time. This can actually be skipped thanks to an empiric criterion which suggests when to stop the etching process by exploiting the interface effect of the multilayer structure. In fact, while etching a staircase structure a rainbow pattern will appear and subsequently disappear once the structure is etched, reaching the n-substrate

and at that point the sample can be removed from the etching solution.

Dielectric layer The samples need a dielectric layer to isolate the exposed material after etching, layer arranged as in Fig. 3.16g. Many types of dielectric layers can be grown in different ways. When dealing with silicon one good option to use is silicon oxide (SiO_2), as it can be grown thermally and it results in good quality layer. Instead, in the case of GaAs, thermal growth cannot be managed. Thus, alternatives have to be employed: the growth of such layer was carried out either with magnetron sputtering or e-beam evaporation, and either silicon oxide or alumina (Al_2O_3) were used.

The magnetron sputtering of SiO_2 (Fig. 3.17a) was performed using plasma; however, it had the disadvantage that the tool utilized for this process needed to be stopped for a 5-minute period as the temperature was rising beyond the safe limit. This mechanism caused degraded quality and low reproducibility of the dielectric layers.

Then, e-beam evaporation of SiO_2 (Fig. 3.17b) and then Al_2O_3 (Fig. 3.17c) were considered. Layers could be grown with thickness between 250 and 500 nm and the process could be performed continuously. However, some defects were detected with the evaporation of silicon oxide, unlike in the case of Al_2O_3 .

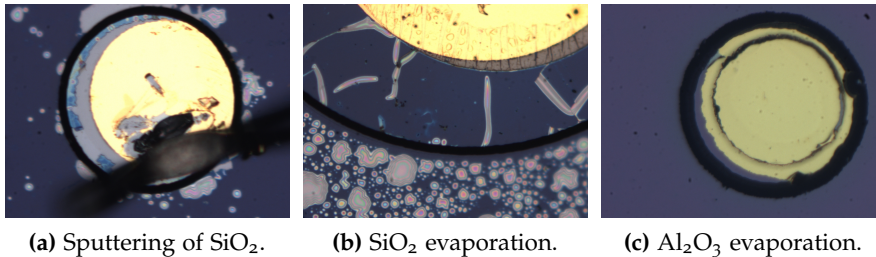


Figure 3.17: Pictures of the different utilized dielectric layers. It is visible how in both SiO_2 growth some defects are present, which do not appear in the case of alumina.

The incident electromagnetic radiation reaches the absorption-region through an opening performed in such layer. This opening was performed by coating the sample with two resist: firstly, the lift-off resist LOR-3B, and further, S1818 (Fig. 3.16d). The coating of the former was characterized by a spinning speed of 2500 rpm and a bake-out of 5 min. Instead, the S1818 followed the same procedure explained as above during the mesa creation. Between the lithography and the dielectric deposition an oxygen cleaning was performed on the device, which results as in Fig. 3.16e. After the dielectric deposition both resists were stripped away with acetone and then with MF-developer (Fig. 3.16g).

Metal evaporation The metal evaporation was performed on both the top and bottom sides of our device, for the p-contact and n-contact,

respectively. In the e-beam evaporator available at the IOM-CNR in Trieste up to 4 different metals can be grown without breaking the vacuum and thus polluting the sample.

p-contact

In the case of the p-contact the contact pattern was defined by the lift-off process, thus the coating of two resist (S1818 and LOR-3B) with the same recipe as the one used for the dielectric layer was necessary (Fig. 3.16h).

Different masks could be used in this process. The one mainly used during this procedure is the circular one, depicted in the leftmost of Fig. 3.18, which was collocated in the center on top of the mesa. Though, also different shapes were developed: the D-shaped one as in middle of Fig. 3.18, and the one equipped with a lateral bonding-site (leftmost of Fig. 3.18). The first one was introduced in order to have a region on the top of the device where there is no metal, to avoid the absorption of photons due to the metal contact. This design improves the behavior of the device especially for low energy photons, since it increases the fraction able to reach the absorption region where the charge carriers that need to be multiplied are created. The second one was developed in order not to bond on the top of the device, but on a lateral side, instead. However, this last mask presented a problem: the resulting capacitance arose mainly from the substrate-pad coupling and not from the multiplication region (where the drop in capacitance should instead be established as Fig. 3.12c shows).

In this case the resulting coating composition was as suggested in [4] to obtained a Schottky contact biased in forward direction, i.e. chromium/gold. Specifically, it was made out of 5 nm of chromium, which is used to improve the adhesion on the GaAs for the following layer composed of 50 nm of gold (Fig. 3.16i).



Figure 3.18: Masks used to define the p-contact. Rightmost the most used mask, where the gold is deposited almost everywhere on the top of the mesa. In the middle, the structure used to create a hole in the metalization where the beam could pass without being attenuated. On the leftmost, the pads designed to avoid the bonding on the structures are shown.

n-contact

Unlike the p-contact, the n-contact necessitates to be opportunely selected in order to create an ohmic contact on the wafer of n-type GaAs:Si doped to $2 \cdot 10^{18} \text{ cm}^{-3}$; in fact, the development of ohmic contact materials plays a key role in injecting external electric current from the metals to the semiconductors [47]. A multilayer of AuGe/Ni/Au was suggested in [48] in order to obtain ohmic contacts on n-GaAs. The suggested ratio between the thickness of the layer of Ni and the eutectic alloy AuGe is in the range of 0.2-0.25 to obtain the optimal

behavior of the contact [48]. The n-contact is deposited on the whole back of the sample, thus no masks are needed during this process.

Finally, after the deposition of AuGe/Ni/Au with thicknesses of 40/10/50 nm, respectively, the two resists on the front side of the wafer, left as protection, are removed with acetone (to strip out the S1818 photoresist) and then with MF-developer (to strip the LOR-3B). The final result is the one shown in Fig. 3.16j.

Bonding As a last step, the wafer was diced, resulting in a number of rectangles of approximately 6 mm by 12 mm, on each of which a set of 12 samples is present. Such array of devices was glued with a conductive paste to a specifically designed PCB. The conductive paste was used so that the n-contact position on the backside of the die is connected to the pad with the biasing pin, in all the PCBs which have been developed. The top p-contacts were then bonded to the lateral pads of the PCBs by an aluminum wire whose thickness is of 25 μm . Figure 3.19 shows one of the PCB that have been developed, where the devices can be bonded and a detail of one single device.

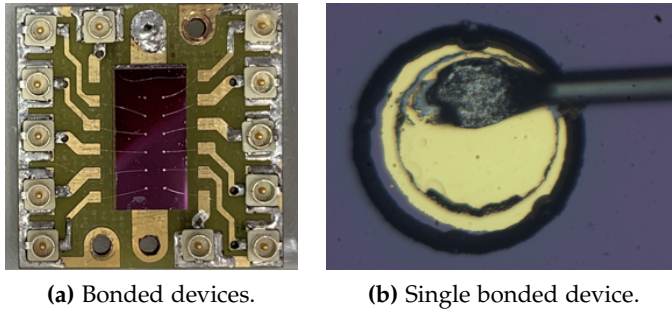


Figure 3.19: (a) Bonded devices on the dedicated PCB. The array is composed of 12 units, arranged in 2 rows of 6 APDs. (b) A detail of the bond of one of those 12 devices.

EXPERIMENTAL SETUP

4.1 LIGHT SOURCES

This section describes the characteristics of the light sources, utilized during this thesis, whose radiation ranges from visible to hard X-ray. The examples reported here are some specific beamlines of the Elettra Synchrotron, a few table-top lasers, the Munich Compact Light Source and an Americium source.

4.1.1 Synchrotron radiation

When electrons traveling at relativistic speed are forced to change their trajectories by a magnetic field, they emit a highly collimated photon beam in the tangential direction, known as synchrotron radiation [49].

One of the most effective ways to obtain a good synchrotron radiation (i.e. stable, with high brightness, high flux, etc.) is to use a structure dedicated to the production of such radiation. Elettra is a third-generation synchrotron radiation facility located in Basovizza (Trieste - Italy) that covers a spectral range spanning from infrared to hard X-rays, which will be taken as an example. This facility is composed schematically of: linac (linear accelerator), booster, storage ring and beamlines, as it can be seen in Fig. 4.1a.

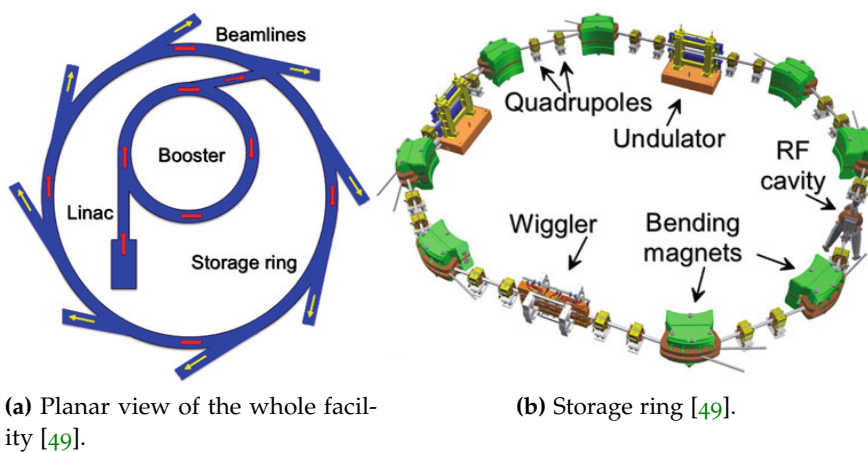


Figure 4.1: Schematic representations of a synchrotron radiation facility: its planar vision and the view of its storage ring, where some of its main elements are visible [49].

The electrons, after being accelerated by a linac and by a booster ring that gives them an extra energy to reach the desired energy (of the

order of the gigaelectronvolt), are injected into the storage ring. Here they are forced to follow a certain path owing to the action of bending magnets, which themselves are one of the sources of synchrotron light. This emission is then collected by a beamline and processed [49].

Inside the storage ring there are several elements that allow it to operate properly: the main ones are illustrated in Fig. 4.1b. As already mentioned, there are the bending magnets that change the electrons direction; the radio frequency cavity, which compensates for the energy lost by the electrons, applying an electromagnetic field that accelerates them in the longitudinal direction; and the insertion devices, which are also magnetic systems that force the electrons to undulate in the transverse direction. The two main types of insertion devices are wigglers and undulators, which characterize specifically the behaviour of a beamline.

The great benefit of exploiting a synchrotron radiation is the high brilliance, defined as the photon flux per unit solid angle and unit solid area at a given frequency: it is 10 billion times higher than conventional X-ray sources. Another fundamental advantage is the energy tunability: in conventional sources, the energy of the photons is fixed, and depends on the material of the anode.

Elettra can operate at two different energies: 2 GeV (with a storage ring current of 310 mA), which is particularly suitable for the low energy beamlines, and 2.4 GeV (with 160 mA), convenient for high-energy photons. The facility works in a top-up mode, in which the current is kept constant during operation thanks to the booster that provides electrons without affecting the run operation of the machine. Elettra thus results in a source of radiation of high flux, brilliance and spatial collimation, polarization and timing properties.

4.1.1.1 Elettra's beamlines

BEAR The BEAR beamline [50] optical layout is based on the plane mirror plane grating configuration which is conceived in order to have optics in sagittal focusing and not to have aberrations of any sort.

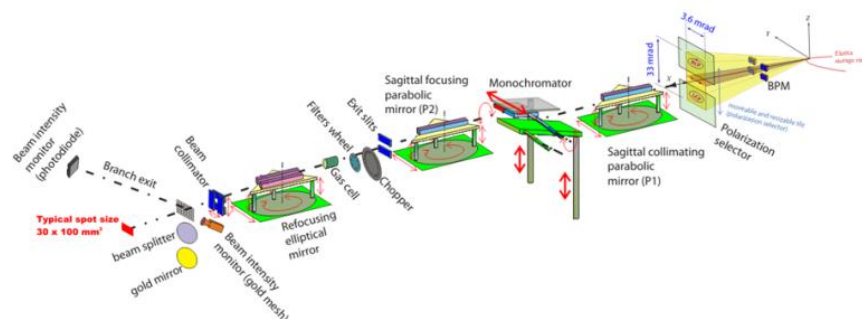


Figure 4.2: Illustration of the BEAR beamline arrangement [50].

As it can be seen in Fig. 4.2, this configuration exploits a beam position monitor installed at the beginning of the beamline in order to keep track of any movement of the beam. Then, a first parabolic mirror P1 positioned at 12 m from the source collimates the light emitted by the bending magnet source without any entrance slits. Downstream from the subsequent monochromator working in parallel light at variable deviation angle, a second parabolic mirror P2 focuses the dispersed beam onto the exit slits (the divergence of the beam is less than $20 \times 20 \text{ mrad}^2$) and an elliptical mirror, focuses the beam on the sample.

This beamline operates in the 2.8-1600 eV spectral region thanks to the monochromator, which is based on two channels (the grazing incidence channel working in the 40-1600 eV energy range, and the normal incidence channel working in the 3-50 eV energy range) working in parallel, either of which can be selected mechanically. Moreover, the beamline has the capability of delivering a polarized light (from linear to elliptical).

The photon flux on the sample has been measured with a calibrated commercial silicon diode and the intensity of the light on the sample is controlled on the monitor section. The flux that is normally measured is shown in Table 4.1 and it depends on the utilized grating. Its spot size is typically $30 \mu\text{m} \times 100 \mu\text{m}$ (vertical x horizontal).

Eventually, there are the experimental apparatus, mainly based on two end stations, and the transfer stage. The spectroscopy chamber is mainly dedicated to the synchrotron analysis of samples, while the preparation chamber, as the name suggests to the preparation of samples. The transfer stage allows to insert samples and to transfer them between the two chambers, always remaining in UHV environment ($1 \cdot 10^{-10}$ mbar) [50].

	Grating [$\mu\text{m}/\text{mm}$]	Energy range [eV]	Resolving power [at 400 eV]	Typical flux [photons/s]
G1200	1200	40-1600	3000	10^{11} at 100 eV with $E/\Delta E = 3000$
G1800	1800	200-1600	5000	10^{10} at 600 eV with $E/\Delta E = 3000$

Table 4.1: BEAR monochromator characteristics [50].

CiPo The Circular Polarization (CiPo) beamline [51] provides a synchrotron radiation beam that can vary its polarization from circular to linear, in a broad range of photon energies, from 5 eV up to 900 eV.

At this beamline, the photon beam is produced by an electromagnetic elliptical wiggler and it is dispersed by means of two collinear monochromators, that alternatively supply two beams in the UV-VUV and soft X-rays, 5-40 eV and 40-900 eV, respectively.

The beamline monochromator involved for the soft X-rays is characterized by four different spherical gratings that cover different energies:

- G1 grating from 400 to 900 eV
- G2 grating from 300 to 700 eV
- G3 grating from 120 to 400 eV
- G4 grating from 40 to 140 eV

as depicted in Fig. 4.3a.

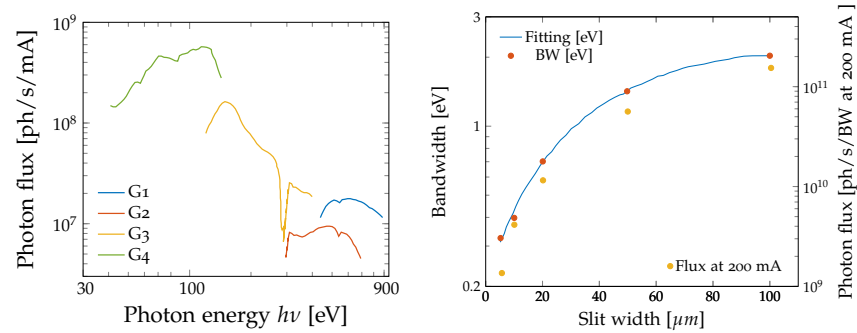


Figure 4.3: (a) Photon flux as a function of the photon energy for different gratings. The four different spherical gratings (G1 to G4) allow to cover the energy range 40 - 1000 eV. The data here reported are measured with a slit of 20 μm at 2.0 GeV [51]. (b) Bandwidth and photon flux as a function of the slit width, measured at 867 eV [51].

The photon flux available on the sample together with the photon energy resolution are important characteristic of the beamline. From Figure 4.3b they can be inferred, as they are plotted as function of the entrance and exit slits width. The data represent the results measured at 867 eV where the resolution has been determined from a Gaussian broadening obtained with a fitting procedure performed by using Voigt functions, while the photon flux was determined by using the double ion chamber [51].

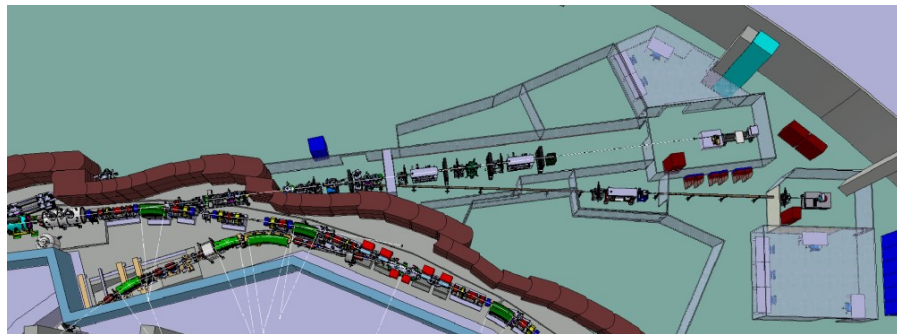


Figure 4.4: Illustration of the XRD2 beamline arrangement.

XRD2 The XRD2 beamline sited at Elettra is characterized by a high photon flux ($2\text{-}3 \cdot 10^{13} \text{ph}\cdot\text{s}^{-1}$) delivered by a super-conducting

multipole wiggler. It is supplied with a monochromator able to provide variable energy ranging from 8 keV to 35 keV; the beam size available is $280 \mu\text{m} \times 292 \mu\text{m}$ with an angular divergence of $2.3 \times 0.3 \text{ mrad}$.

Generally this beamline is dedicated to high-throughput molecular-crystallography experiments [52]. A view of the plan of the beamline layout is depicted in Fig. 4.4.

TwinMic The TwinMic beamline [53] is able to integrate the scanning and full-field imaging modes into a single instrument. This allows to identify element distributions inside the specimen thanks to the different electronic structure of atoms, which are characterized by their own specific spectral fingerprint. Moreover, shorter wavelengths allow a higher optical resolution with respect to visible light and this is why this beamline is provided with a short undulator placed in a straight section of the storage ring, supplying energies ranging between 400 and 2200 eV [54]. Figure 4.5 shows the main elements which form the beamline.

A high energy resolution is available and the flux is of the order of 10^9 photons/s. The sample stage consist of two stepper motors (providing X and Y movement) and piezoelectric PI motors providing X and Y movement for scanning mode [54].

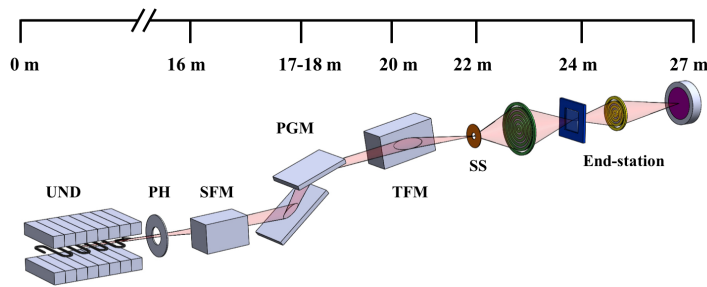


Figure 4.5: Optical scheme of the TwinMic beamline: short undulator X-ray source (UND), pinhole (PH), collimating cylindrical mirror (SFM), plane-grating monochromator (PGM), refocusing toroidal mirror (TFM) and secondary X-ray source (SS) [54].

TwinMic soft X-ray spectro-microscope is optimized to analyze lighter elements. Figure 4.6 reports the elements that can be accessed through the beamline.

4.1.2 Table-top lasers

Green lasers, whose wavelengths range between 510 nm and 540 nm, were chosen to test the fabricated devices. Although the devices are designed for high energies, this choice was made in order to ensure that the photo-induced charge generation were limited to the absorption region only. This configuration allows to have ideal conditions of charge injection, i.e. close to the entrance window of the absorp-

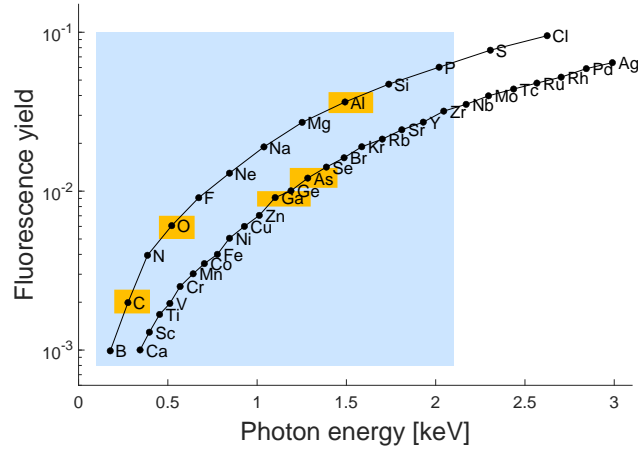


Figure 4.6: Elements that can be studied with the energies available at Twin-Mic [53]. In yellow the elements of interest, which are the components of the devices under study, are highlighted.

tion region, during noise characterization. At this energies, as it can be verified from Fig. 4.7, the absorption length ϵ (the inverse of the absorption coefficient μ , namely $\epsilon = 1/\mu$) ranges between 160 and 200 nm, when bulk GaAs is considered. This condition has enabled

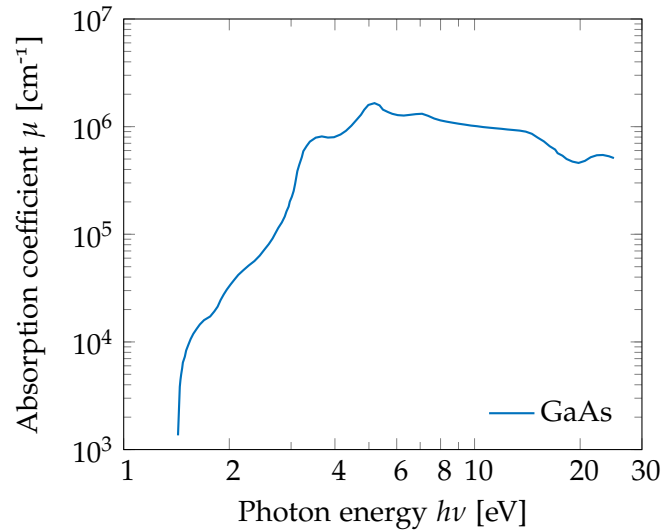


Figure 4.7: Absorption coefficient of GaAs versus photon energy from 1 eV to 25 eV [19].

the study of the sole multiplication effect without having it combined with the effect due to charges photo-generated in the multiplication region (and thus undergoing partial multiplication).

Here, a list of the three tabletop lasers utilized is reported.

- The *Millenia Vs*, which is an all solid-state, high-power, visible continuous-wave (CW) laser. Its output is a CW at 532 nm. The laser head houses a sealed laser module and a shutter to block

the output beam for safety. The highly efficient, diode-pumped neodymium yttrium vanadate (Nd:YVO₄) laser crystal requires a compact recirculating chiller that regulates its temperature. Moreover, the laser can be easily operated thanks to the available controller. Its output is maintained stable overtime, in fact, from specifications, its power may vary of $\pm 1\%$ (value measured over a 2-hour period and after a 30-minute warm up from the standby mode). The provided output is also characterized by low noise, less than 0.04% rms (over a 10 Hz - 100 MHz bandwidth). The laser was used at 0.2 W and 0.4 W, although it can reach even higher powers (5 W) [55].

- An all normal dispersion ytterbium-doped fiber laser oscillator (built at the Laser Laboratory situated at Elettra) opportunely tuned in order to have an output light source characterized by a 515-nm central wavelength and a power of 5 mW. The main fiber laser oscillator is characterized by a central wavelength of 1030 nm with a 20-nm bandwidth, a pulse whose length is of 3 ps, a repetition rate of 80 MHz and an output power of 80 mW. Its output is then amplified, thus the resulting output power is 250 mW and the amplified pulse length is 6 ps. After this amplification the signal is further processed to obtain the visible green light previously described. This is done through a KDP (Potassium Dihydrogen Phosphate) crystal that allows the second harmonic generation (SHG), thus converting the 1030-nm infrared signal to the 515-nm green one. A schematic of the oscillator and the amplifier is shown in Fig. 4.8.

SHG: a nonlinear optical process in which two photons with the same frequency interacting with a nonlinear material generate a new photon with twice the frequency of the initial photons.

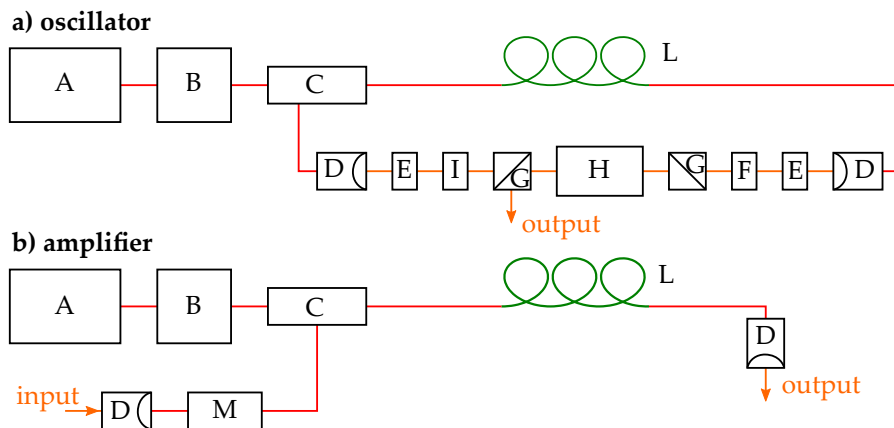


Figure 4.8: Oscillator and amplifier scheme, *a* (above) and *b* (below) respectively. They are used in the ytterbium-doped fiber laser, built at the Laser Laboratory situated at Elettra, Trieste. Figures courtesy of Dr. Paolo Cinquegrana.

- The third harmonic of an infrared (1656 nm) pulsed tabletop laser, whose pulses were characterized by a repetition of 200 kHz

and a width 100 fs, able to deliver an average power of 20 μ W. This laser was borrowed from the Q4Q Lab at Elettra, in Trieste.

4.1.3 Munich Compact Light Source

The Munich Compact Light Source (MuCLS) is a compact synchrotron source, which works as a miniature synchrotron producing a high-flux, large-field-of-view, quasi-monochromatic X-ray beam which can be tuned in energy. The CLS is based on the inverse Compton scattering producing X-rays through the collision of relativistic electrons with infrared laser photons [56]. The light produced is a 60 ps (rms) X-ray pulse coming at a repetition rate of 65 MHz. The typical energy range is 15-35 keV. Usually, the flux ranges around 0.5 - 0.8 $\cdot 10^{10}$ ph/s, and 75 - 120 photons per individual X-ray pulse can be expected.

4.1.4 Americium-241

Americium-241 is a radioactive isotope of americium characterized by a half-life of 432.2 years. Americium-241 decays mainly via α -decay with a weak γ -ray byproduct. The α -decay energy, which is produced in most of the cases, is approximately 5.4 MeV; the γ -ray energy, instead, is close to 59 keV.

The used source was a compact and portable source mounted in a dedicated tabletop housing provided by the INFN, the Italian National Institute for Nuclear Physics, of Trieste. It must be pointed out that a source of this kind emits almost isotropically; this lack of collimation is crucial to interpret the results which will follow in Ch. 5.

4.2 READOUT AND ACQUISITION ELECTRONICS

Different experimental setups were used as various measurements were performed with the light sources described in section 4.1.

It has to be noted that since it is not possible to remove a die attached to a certain PCB a universal PCB was designed in order to have the devices of one set bonded just on a single board compatible with most of the experimental setups. The PCB mostly used appears in Fig. 4.9: the array of 12 devices is attached to the center of the board by means of a conductive epoxy glue, connecting the back n-contact to the biasing pin; then, 12 wire-bondings connect each device to a pad leading to a U.FL connector (a miniature RF connector with certified characteristic impedance up to 6 GHz). The U.FL connectors were chosen for a number of reasons: the devices had to be tested in different environments some of which requiring UHV compatibility; the carrier boards had to be quickly interchanged, thus requiring easily detachable connections; signal integrity against interference and high-frequency loss rendered the use of RF coaxial connections

indispensable; last but not least, the extremely limited amount of space available in many setups allowed only small connectors to be mounted in proximity of the devices.

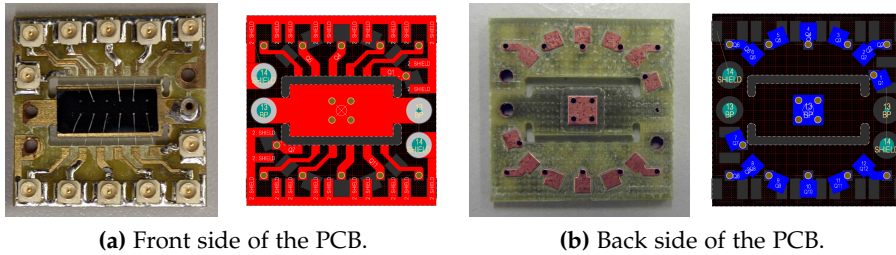


Figure 4.9: Front (a) and back (b) side of the PCB board where the devices must be accommodated in order to perform the measurements. Both the board realized and the corresponding layout designed with the CAD Altium are shown.

4.2.1 Instrumentation

For several preliminary tests of the manufactured GaAs APDs some general purpose readout electronics previously developed by the Instrumentation and Detector Laboratory of Elettra were utilized.

4.2.1.1 AH501B

The AH501B picoammeter was used to measure the currents of the GaAs APDs in dark conditions and under illumination. Sincrotrone Trieste's AH501B is a 4-channel, 24-bit resolution, ultra-wide input dynamic range picoammeter with an integrated bias voltage source. It is composed of a specially designed transimpedance input stage for current sensing combined with analog signal conditioning and filtering stages making use of state-of-the-art electronics. This device can perform bipolar current measurements in the range of ± 2.5 nA (with a rms noise lower than 250 fA), in the range of ± 2.5 μ A (rms noise of about 25 pA), and up to ± 2.5 mA (rms noise lower than 25 nA) with sampling frequencies up to 26 kHz (for 1 channel and a 16-bit resolution) and 6.5 kHz (4 channels, 16 bit/sample). Low temperature drifts, good linearity and very-low noise levels enable users to perform very-high-precision current measurements. The AH501B is housed in a light, robust and extremely compact metallic box that can be placed as close as possible to the current source (detector), in order to reduce cable lengths and minimize possible electromagnetic pick-up. It is specially suited for applications where multi-channel simultaneous acquisitions are required [57].

4.2.1.2 Preamplifiers

It is good practice to amplify and filter opportunely a signal coming from a detector maximizing the information brought by the specific quantity to be measured. Depending on the experiment for instance, it may be necessary to distinguish single events a few nanoseconds long or to quantify extremely low amounts of charge (down to the order of a few hundreds of electrons). In particular, if the photon flux or the photon energy is low, the signals provided by the photodiode can be weak and difficult to measure, thus, an amplification chain is necessary.

The front-end electronics of this amplification chain is characterized by a preamplifier as its first amplification stage. Ideally, this would have to be characterized taking into account the above-mentioned signal specifications by a bandwidth of the order of the GHz, a low noise (in some situation even as low as a few hundreds of electrons) and a stable input current-to-voltage transfer function, which are not compatible characteristics, thus some compromises have to be reached. Three solutions were chosen according to the different scenarios: a transimpedance amplifier (TIA), a charge sensitive amplifier (CSA) and an RF wideband amplifier.

TIA The TIA is employed because within its working spectrum it has a flat frequency response, i.e. the output is proportional to the signal; so, it is suitable for reproducing the shape, of (slow) current signals as well as measuring DC levels with high precision.

CSA The CSA is actually a current integrator, so it is not used to observe pulses as it completely changes their shape in the time domain; instead, it allows to measure the charge of the pulses when this is very small, even of the order of few electrons. Nevertheless, this value depends on the detectors and the limits of the setup, such as connections (due to parasitic capacitance); in our case the necessity to leave the detectors interchangeable limited us enormously, so it was not possible to reach precisions better than a few hundred electrons.

PIT Neither the TIA nor the CSA are able to analyze ns pulses in the time domain; in fact, for fast pulses as the ones we dealt with, a wide band amplifier would be possibly employed before entering the oscilloscope if the involved signals were small. An example of wide band amplifier is the PIT (an amplifier built in the Detector & Instrumentation Laboratory of Elettra), which will be described later on. Otherwise, if the signal does not need to be preamplified it can enter the measurement unit (oscilloscope) directly. It is important to point out that the broadband setup must be matched in impedance, thus it has to be terminated with 50Ω , which acts as a conversion resistance between the detector current and voltage, which is then amplified and/or acquired.

To resume, the strength of the TIA is that it has a good SNR (if properly designed) thanks to the much higher conversion factor due

to its feedback resistor R ; it features a bandwidth much narrower than that of the RF amplifier, thus it is useful to read signals which are not too fast in the time domain or to amplify signals without spectral distortion (contrary to the CSA), e.g. noise measurements with a spectrum analyzer, measurements of low continuous currents (where the interest is not in the current trend but only in its level). On the other hand, the RF amplifier being 50-ohm matched presents a conversion gain way lower with respect to the TIA. The CSA instead is basically a TIA operated in a region where the effect of the feedback resistor is negligible: this allows to reduce the thermal noise due to the resistance, but strongly modifies the shape of the signal.

TIA Transimpedance amplifiers are used to convert low-level photodiode currents to usable voltage signals; for noise measurements utilizing a spectrum analyzer, a transimpedance preamplifier with low parasitic capacity layout has been developed, and it is implemented with an operational amplifier (op-amp). From the noise point of view the op-amp can be described in terms of two equivalent noise sources, a voltage noise generator e_n and a current noise generator i_n . These quantities are specified in the data sheet of the op-amp. The current noise generator represents essentially the shot noise of the bias currents in the amplifier input stages, while the equivalent voltage noise is usually due to thermal noise in resistive components [58], that is in our case where the chosen ICs are FET-input operational amplifiers; whereas at lower frequency the prevalent noise is the flicker noise.

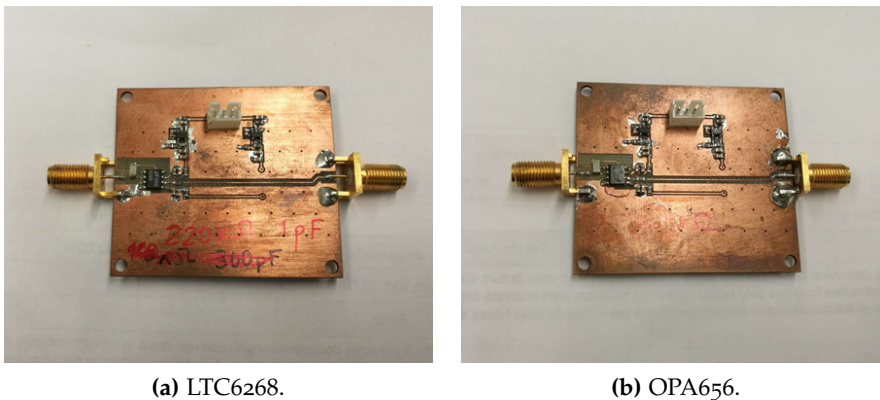


Figure 4.10: First prototype of a transimpedance amplifier using a LTC6268 (a) and the preamplifier prototype on the basis of an OPA656 (b).

According to the respective measurement needs, two versions have been realized (Fig. 4.10). The first prototype is based on the LTC6268 op-amp, featuring a transimpedance of $10 \text{ k}\Omega \parallel 11 \text{ pF}$, showing a flat frequency response up to approximately 2 MHz (sometimes modified in a $220 \text{ k}\Omega \parallel 1 \text{ pF}$ version). The second prototype is based on the OPA656 operational amplifier, with a transimpedance of $4.7 \text{ k}\Omega \parallel 10 \text{ pF}$,

featuring a higher bandwidth. This amplifier has been used in cases where a wider output dynamic range was required.

The actual set up used for the measurements is described later in section 4.2.2.1. Here the noise analysis of the above-mentioned TIAs is carried out.

Let's consider the general circuit in Figure 4.11: Z_1 represents the impedance of the photodiode, the cables and the input impedance of the op-amp (this one is high, thus irrelevant), C_2 and R_2 are the feedback resistance and capacitance part of the impedance Z_2 , i_n and e_n are the noise sources of the op-amp itself and i_{nR} is the thermal noise of the feedback resistor. This last one is expressed by

$$i_{nR}^2 = \frac{4kTB}{R} \quad (4.1)$$

in units of A^2 , where $k = 1.381 \cdot 10^{-23} \text{ J K}^{-1}$ is the Boltzmann's constant, T is the temperature in K, B is the bandwidth and R the value of the resistor. It is always present in all resistors at temperatures above the absolute zero [58].

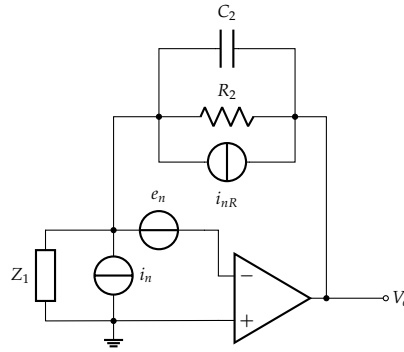


Figure 4.11: Circuit with noise sources in evidence.

Within the linear region of the op-amp, this latter circuit can be analyzed through the one depicted in Figure 4.12 and for the superposition principle each non-correlated noise source can be studied independently. Thus the total noise can be obtained through the three circuits in Figure 4.13, which can be modeled with the three systems expressed below and denominated as equation 4.2, each of which takes into account only a single noise source, i_{nR} (Fig. 4.13a), i_n (Fig. 4.13b), e_n (Fig. 4.13c); **a**, **b**, **c** respectively.

$$\mathbf{a.} \begin{cases} V_o = -AV_{in} \\ V_{in} = Z_1 I_1 \\ V_o = Z_1 I_1 + Z_2 I_2 \\ I_2 = I_1 + i_{nR} \end{cases} \quad \mathbf{b.} \begin{cases} V_o = -AV_{in} \\ V_{in} = Z_1 I_1 \\ V_o = Z_1 I_1 + Z_2 I_2 \\ I_2 = I_1 + i_{nR} \end{cases} \quad \mathbf{c.} \begin{cases} V_o = -AV_{in} \\ V_o = (Z_1 + Z_2) I_2 \\ V_o = Z_1 I_2 - e_n \end{cases} \quad (4.2)$$

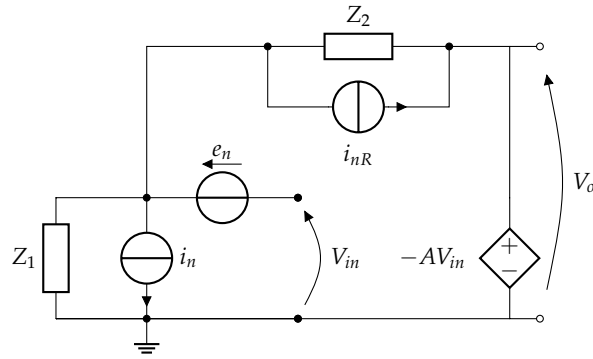
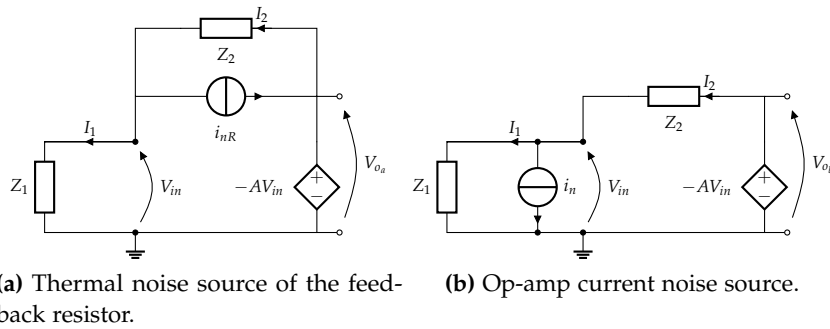
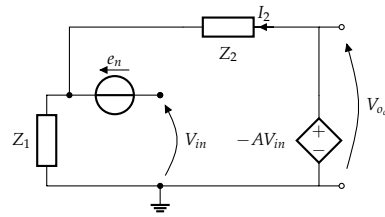


Figure 4.12: Linear-region equivalent circuit.



(a) Thermal noise source of the feedback resistor.

(b) Op-amp current noise source.



(c) Op-amp voltage noise source.

Figure 4.13: TIA's equivalent circuits with independent noise sources.

Solving the just-mentioned systems, the three following equations are obtained:

$$\begin{cases} V_{o_a} = \frac{AZ_1Z_2}{(A+1)Z_1+Z_2} \cdot i_{nR} \\ V_{o_b} = \frac{AZ_1Z_2}{(A+1)Z_1+Z_2} \cdot i_n \\ V_{o_c} = \frac{AZ_1}{(A+1)Z_1+Z_2} \left(1 + \frac{Z_2}{Z_1}\right) \cdot e_n. \end{cases} \quad (4.3)$$

Thus the noise output voltage V_{o_n} can be written as the sum of the single squared uncorrelated noise contributions, namely, $V_{o_n}^2 = V_{o_a}^2 + V_{o_b}^2 + V_{o_c}^2$, which gives

$$V_{o_n}^2 = \left| \frac{AZ_1Z_2}{(A+1)Z_1+Z_2} \right|^2 (i_n^2 + i_{nR}^2) + \left| \frac{AZ_1}{(A+1)Z_1+Z_2} \left(1 + \frac{Z_2}{Z_1}\right) \right|^2 e_n^2. \quad (4.4)$$

Let us define Z_{P12} and Z_A as

$$Z_{P12} = \frac{1}{Y_{P12}} \triangleq Z_1 \parallel Z_2 \quad (4.5)$$

and

$$Z_A \triangleq \frac{AZ_1Z_2}{(A+1)Z_1+Z_2}. \quad (4.6)$$

So $V_{o_n}^2$ can be rewritten as:

$$\begin{aligned} V_{o_n}^2 &= |Z_A|^2(i_n^2 + i_{nR}^2) + \left| Z_A \frac{1}{Z_{P12}} \right|^2 e_n^2 \\ &= |Z_A|^2 \left(i_n^2 + i_{nR}^2 + |Y_{P12}|^2 e_n^2 \right). \end{aligned} \quad (4.7)$$

Considering $A \gg 1$, which is the case when operating with an op-amp at least a decade below its transition frequency, then equation 4.6 simplifies to $Z_2 \parallel Z_1 A \simeq Z_2$. Furthermore, choosing the opportune op-amp, the thermal noise of the resistor is way larger than the noises which characterize the op-amp (i.e. $i_n^2, |Y_{P12}|^2 e_n^2 \ll i_{nR}^2$).

The noise floor at the input of the spectrum analyzer can then be calculated from equation 4.7. Let us consider as an example the case of the LTC6268; from its datasheet it can be inferred that $i_n \leq 100 \text{ fA}/\sqrt{\text{Hz}}$ for frequency below 1.5 MHz and $e_n \approx 4.3 \text{ nV}/\sqrt{\text{Hz}}$ in the range between 1 and 1.5 MHz. Considering the particular case where the spectrum analyzer input resistance is 50Ω , the feedback resistance (Z_2) is $10 \text{ k}\Omega$, and the bandwidth resolution is 10 Hz, then the noise power on the input of the spectrum analyzer is approximately -135 dBm in the band of interest (1-1.5 MHz), as it can also be observed in Fig. 4.18.

CSA - CUBE Charge sensitive amplifiers are a good choice when designing the readout circuitry for pulse detectors, as they integrate the input signal giving out an output signal which is proportional to the charge collected during each pulse event.

Thus for the spectroscopic analyses, a front-end electronics based on an ultra-low-noise charge amplifier has been developed. Such device is the ASIC CUBE produced by XGLab [59]. Given the biasing topology of the APDs and their typical capacitance (approximately 3 pF), the version of CUBE used is the PRE_039 able to integrate positive currents working with source capacitances from 3 to 10 pF. In terms of performances, this device has a conversion capacitance of approximately 50 pF and under optimal conditions it presents an equivalent noise charge of 20 rms electrons.

Given the fragility of the ASIC and its cost, the system in question was conceived according to a modular approach, in order to make several blocks replaceable and reusable. In particular, the PCB on which the CUBE is permanently bonded and the PCB on which the

APD is glued are separate. In this way, it is possible to use the same system to amplify the signal coming from any detector that is mounted each time, without having to permanently bind the ASIC to a specific device.

The board onto which these parts are mounted comprises a bias module that manages the power supplies and the reset signals of the CUBE, as well as connectors and polarization networks that allow to bias the die under study and to choose as input of the CUBE a specific device out of the 12-diode array.

Due to the presence of the described connections (necessary for interchangeability) and the polarization network with AC coupling (necessary for the non-negligible dark currents of the APDs), the charge amplifier cannot achieve its ideal performances in this system; however, a search for the best conditions, given these constraints, allowed to obtain an equivalent noise of about 600 rms electrons.

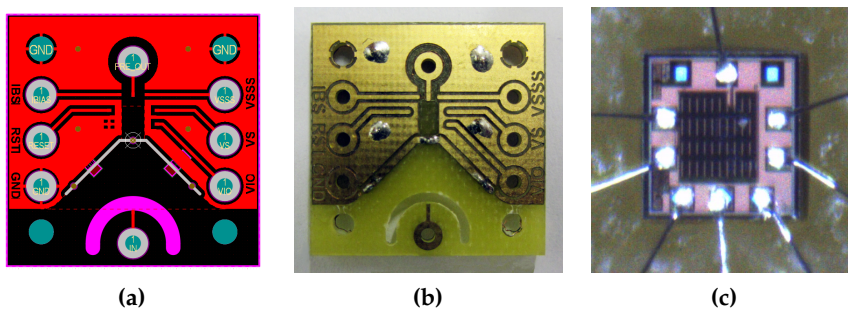


Figure 4.14: Upper-side of the PCB dedicated to the placement of the CUBE: CAD project (a) and actual realization (b). (c) Picture of the bonded CUBE, whose dimensions are $750 \mu\text{m} \times 750 \mu\text{m} \times 250 \mu\text{m}$.

WIDEBAND AMPLIFIER - PIT The wideband amplifier used in the measurements, called PIT, has a gain of about 35 dB, with a relatively flat response (-3dB) from 100 kHz to 2 GHz, still usable up to 4 GHz. It is composed by two stages of Mini-Circuits Gali-51+ monolithic amplifiers [60]. The noise figure is about 3.5 dB, and input and output ports are matched to 50Ω . It has been developed internally at the Detectors & Instrumentation Lab of Elettra mainly to amplify short pulses coming from microchannel plates (MCP). Figure 4.15 shows its internal structure, carefully optimized (according to RF design principles) to maintain its characteristics.

4.2.2 Setups

4.2.2.1 Laser setup

To test the SAM-APDs initially some green laser sources were utilized, as described in 4.1.2. The green table-top lasers were chosen in order

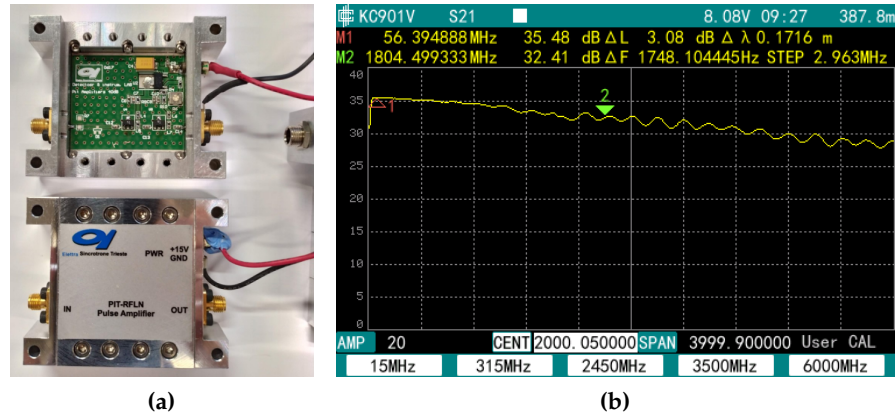


Figure 4.15: PIT wideband amplifier (a) and its gain up to 4 GHz (b).

to ensures that photogeneration occurs entirely within the absorption region. Below, the different setups involved using the table-top laser in different experiments (i.e. noise, time-response and spectroscopic measurements) are described.

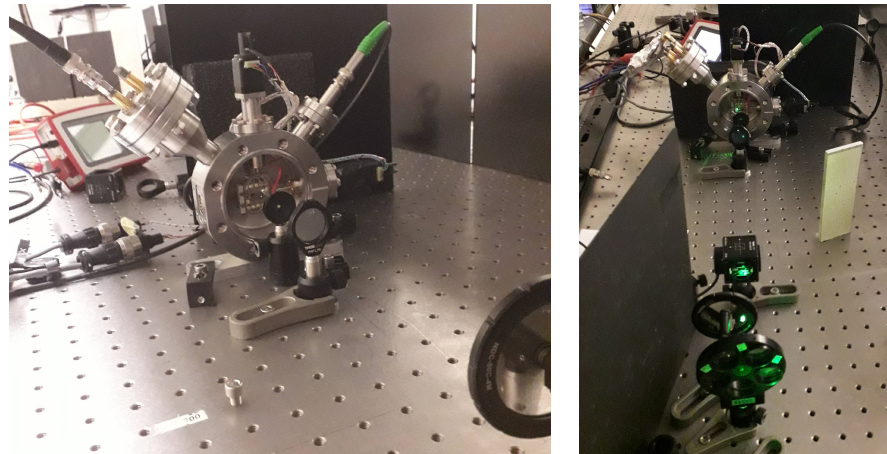


Figure 4.16: Views of the laser setup: the chamber where the devices are placed (a) and the sets of lenses used to focus the beam (b).

NOISE MEASUREMENTS SETUP The system built for measuring excess noise (F) and multiplication (M) was based on a transimpedance amplifier front end to convert the current of the photo-detector into a more convenient voltage signal.

In particular, the setup to measure both F and M was realized by feeding the output of the TIA into a spectrum analyzer (Agilent EXA Signal Analyzer N9010A) and an oscilloscope (Lecroy HDO6104) at the same time. A block diagram of the measurement system is shown in Figure 4.17. The device under test (DUT) was kept in a chamber. This was equipped with a movable support thanks to which it was

possible to execute remotely controlled spatial scans of the device. All the measurements here reported were characterized by the fact that the light spot was always focused in the center of the sample opening.

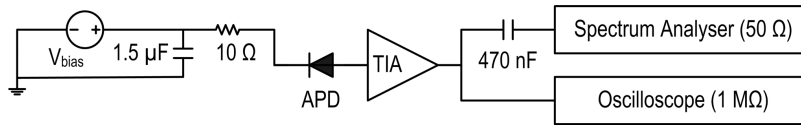


Figure 4.17: Noise setup. The signal from the TIA is fed both to the spectrum analyzer and to the oscilloscope to obtain the signal in both time and frequency domains.

To reduce the noise due the power supplies either the HP E3631A and the Keysight B2961A were filtered in an appropriate way, with an ad-hoc RC filter and the Keysight low noise filter N129A, respectively.

Then, downstream from the pin diode there was the TIA and as mentioned above its output signal was fed into the oscilloscope (whose input resistance was set as $1\text{ M}\Omega$) and the spectrum analyzer. As it can be seen in Fig. 4.17, the input stage of the analyzer is AC-coupled through a capacitor as it is not compliant with the DC levels that can be present at the output of the TIA. The chosen capacitor has a value of 470 nF .

The TIA was used to convert the diode current into a proportional voltage measurable with the spectrum analyzer, in order to recover information about the noise. In fact, the noise generated under illumination is different from the noise in the dark and this difference contains information about the noise associated with the the avalanche gain process which multiplies the photocurrent.

Moreover, the TIA was characterized by a feedback resistance of $10\text{ k}\Omega$ and a capacitance of 11 pF . Those values were chosen in order not to saturate the TIA with the maximum photon flux used and to have a frequency cut above 1.5 MHz considering the fact that its input capacitance is of 55 pF (cable, setup and device).

In Figure 4.18, several signals recorded from the spectrum analyzer can be seen. The blue signal is the noise floor of the instrument HP E3631A, the red one is the noise coming from the biased TIA without the suitable filter, while the green one is the noise measured adding the aforementioned RC filter on the power supply line for the DUT. As it can be seen, the green signal is significantly less noisy than the red one, showing that the filter is working properly.

TIME RESPONSE MEASUREMENTS SETUP A first trial to measure the time response of our devices was performed by using the ytterbium doped fiber laser described in section 4.1.2. The aim of the measurements was to record the response of the devices to the ultra-short laser pulses (10 ps).

The setup build to test the time response consists of an oscilloscope (Tektronix DPO71254C), which is able to read directly the signal

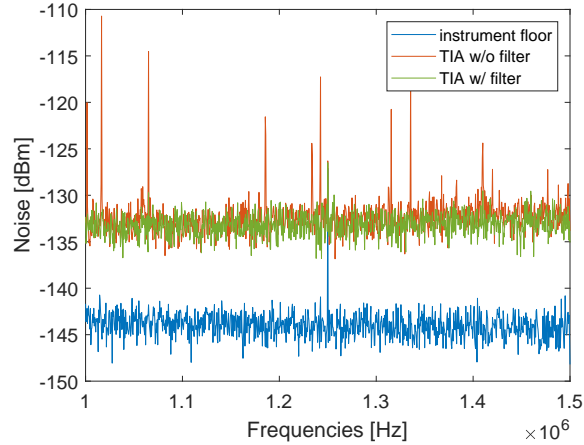


Figure 4.18: Noises detected with the spectrum analyzer: in blue the instrument floor, in red the output of the TIA without filtering the bias, in green the same signal with the addition of the filter.

through a 1 dB attenuator. In some occasions, when a certain amount of gain was necessary, the custom version of the PIT amplifier would be inserted between the devices and the oscilloscope (in place of the attenuator). The oscilloscope has to be fast enough to identify the single pulses, thus the one chosen features an analogue bandwidth of 12.5 GHz and a sampling frequency of 50 GS/s. As in the case of the noise measurements a low-noise power supply and its filter were utilized to provide a clean voltage sourcing. The power supply is the Keysight B2962A and its low noise filter is the N1294A-022 Low Noise Filter.

The optical arrangement and housing of the devices was identical to the one employed for the noise measurements.

SPECTROSCOPIC MEASUREMENTS SETUP In order to evaluate the capabilities of our detector in spectroscopy applications we tried to solve the K_α and K_β lines of the iron-55 (^{55}Fe) at 5.9 keV and 6.49 keV, respectively. However, at the present state it is impossible too see its spectrum as the devices still present too much noise and too little collection, thus as preliminary measurements a triggered source of radiation was used. This one was employed to identify more easily the events related to the source.

Initially, a 540 nm pulsed laser with a repetition rate of 200 kHz was used. The data were collected by means of an oscilloscope, which was triggered by the signal coming from a fast reference photodiode on which a part of the laser beam was diverted. The block diagram of the electronics is shown in Fig. 4.19.

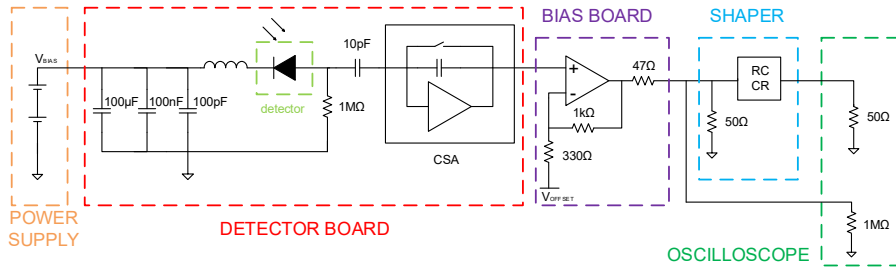


Figure 4.19: Block diagram of the setup for the spectroscopic measurements.

4.2.2.2 Synchrotron beamlines setup

XRD2 SETUP To assess the response to photons of high energy, the devices were tested under irradiation with hard X-rays generated by the XRD2 wiggler beamline at Elettra [52] (12.4 keV and $1.7 \cdot 10^{13} \text{ph} \cdot \text{s}^{-1}$ over an area of $300 \mu\text{m} \times 90 \mu\text{m}$).

For tests under illumination the devices were mounted on a dedicated, 4-channel printed circuit board and accommodated in the aforementioned UHV-compatible chamber, which was placed downstream in the focal plane of the XRD2 line. The photocurrents generated in the devices were measured utilizing the aforementioned AH501B.

Thanks to incorporated perpendicular movement stages it was possible to perform remotely controlled spatial mesh scans of the devices through the beam with a spot-size of approximately $100 \mu\text{m} \times 100 \mu\text{m}$ and a typical photon flux in the order of $10^{12} \text{ph} \cdot \text{s}^{-1}$. Various mesh scans were performed in order to evaluate the homogeneity of the generated photocurrent over the entire surface of the device. The scans were acquired with a step of $30 \mu\text{m}$.

Furthermore, such photocurrent maps were used to align the center of the DUT with the incident radiation to perform position-invariant IV measurements and waveform acquisitions. These were carried out by using an oscilloscope (Keysight DSOS404A) with 4-GHz bandwidth, a sample rate of $20 \text{GSa} \cdot \text{s}^{-1}$ and a 10-bit resolution.

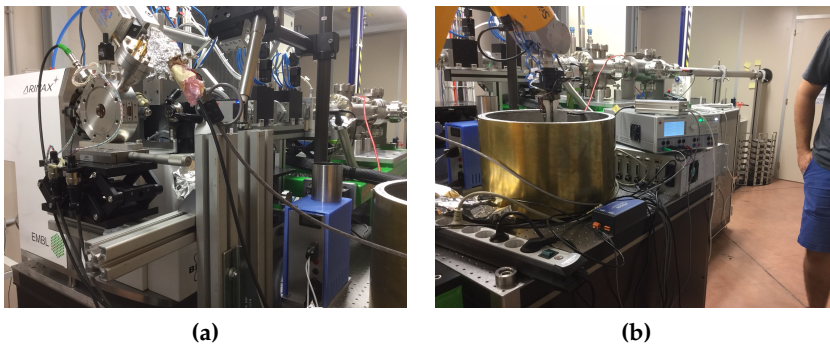


Figure 4.20: Some elements positioned at the XRD2 beamline. (a) The chamber sited at the end of the beamline, where the focus is found. (b) A view of the beamline and the instrumentation used.

Some preliminary timing measurements were performed by taking advantage of the bunch structure of Elettra. Although the experimental setup had not been optimized for precise timing measurements, the acquired data allowed to extract some quantitative metrics for the APD response.

The synchrotron facility was operating in its normal filling mode, providing 432 equidistant bunches per revolution (each bunch is characterized by a length of approximately 150 ps and outdistanced from the following one by 2 ns) and including a dark gap, which was used as trigger for the oscilloscope. The characteristic impedance of the impedance-matched coaxial cabling, which connects the device to the oscilloscope, in combination with the capacitance of the device turns into a low-pass filter with a time constant of approximately 1.5 ns, which acts as an integrator for the substantially shorter bunch signals.

CIPO SETUP The setup employed at this beamline called for the movable chamber shown on the left side of Fig. 4.21 and the picoammeter AH501B to measure the currents, in order to perform xy-scans and invariant position IV. The measurements were carried out in vacuum, thus the chamber had to be placed opportunely at the end of the beamline with a pump helping to obtain the vacuum level required to perform the measurements without damaging the performances of the beamline. The right side of Fig. 4.21 shows how the chamber had been attached to the beamline.

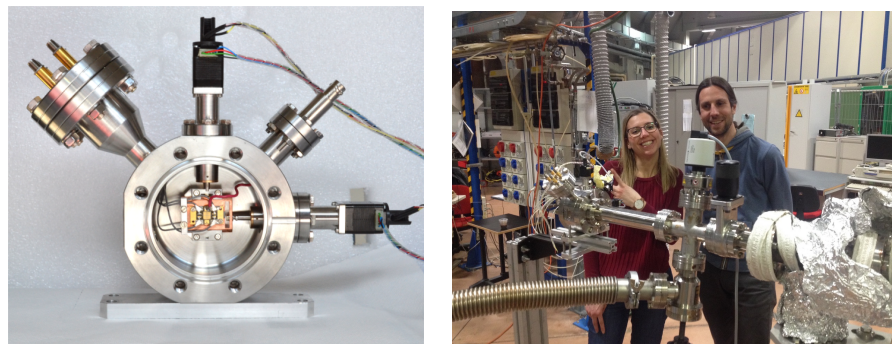


Figure 4.21: Arrangements built at the end of the CiPo beamline: the chamber (left) placed on the focus of the beamline and with a cross pipe inserted in front of it to obtain the vacuum (right).

BEAR SETUP An additional PCB was designed in order to interface the sample holder on the BEAR beamline, which was adapted to the load-lock system of the UHV chamber, and the PCB on which the devices were bonded. An exploded view and an illustrative photo are shown in Fig. 4.22. The devices at this stage were still glued on a smaller PCB which allowed the connection of only 4 out of the 12 fabricated devices.

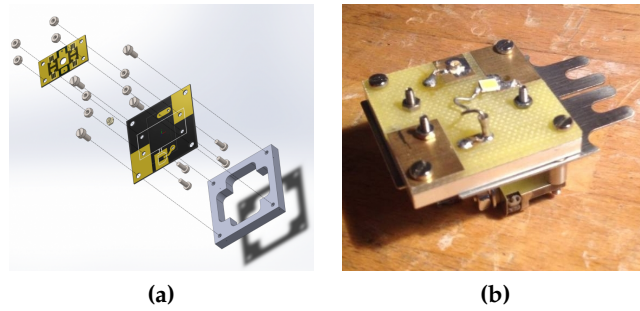


Figure 4.22: Design (a) and illustrative photo (b) of the PCB prepared to interface the sample holder used in the BEAR beamline and the one where the devices are glued to read their signals.

Moreover, the measuring circuit was designed to ensure that no currents originating from the surface charge compensation following photoemission, which is very probable in the photon energy range of 500-1000 eV, drained on different grounds was summing up with the photo-current from the device, affecting the measurements. As bias power supply and amperometer a Keithley 6430 was used.

TWINMIC SETUP The setup placed at TwinMic necessitated of a specific sample holder. Figure 4.23 shows the sample holder fabricated by the mechanical workshop of Elettra. This holder was placed inside the vacuum chamber of the beamline. The signal and the power supply were brought out by means of cables build specifically for this purpose. The power supply used was the ultra-low-noise Keysight B2962A, while to acquire the signals the picoammeter described above was used. As it can be observed from Fig. 4.23a the slits in the PCB are useful both for reducing the coupling capacitance and, in this case, to measure the direct beam and focus the optics. Without these slits every time we had to change energy we would have needed to remove the device, mount a dummy one, focus, remount the device, find again the right area and measure, which becomes less precise and more time consuming.

Figure 4.23b shows an old PCB where the slits were not present and the devices were already glued on it. A maximum of 4 signals can be extracted at once.

4.2.2.3 Americium setup

The setup used to perform spectroscopic measurements with the Americium source is as the one mentioned in section 4.2.2.1 (which describes the setup for the laser used for this same aim). The setup used with the americium source is shown in Fig. 4.24. In this configuration the low-noise power supply (Keysight B2962A) was used both to power the bias module of the CUBE and the devices. A function

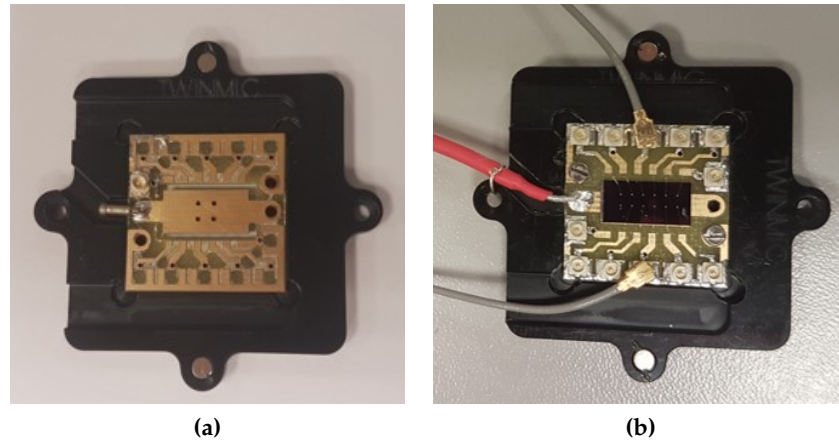


Figure 4.23: Device holder built ad-hoc for the TwinMic beamline (in black) where the PCB is embedded.

generator was used to produce the 50-kHz-signal to reset the CUBE, while the waveforms were acquired with the aforementioned 10-bit oscilloscope. The radioactive source, characterized by a diameter of 8 mm was placed 5 mm apart from the detectors.



Figure 4.24: Americium 241 setup.

Due to the wide angle of incidence the variability of the measured currents may be larger with respect to the results obtained with a source whose spot is collimated and centered in the middle of the single device taken into account.

The acquisition required a large amount of time as an event was happening every 2 seconds, thus to acquire 1000 events approximately 30 minutes were necessary.

4.3 VIRTUAL INSTRUMENTATION

In order to control and acquire the data with the above-mentioned systems, some ad-hoc software tools have been developed. These are virtual instrumentation developed in LabVIEW. These softwares allow

to perform automated planned measurements both with the motorized system for mapping the devices and with the setup with spectrum analyzer for noise measurements. A screenshot of the main panel of one of these program is shown in Fig. 4.25.

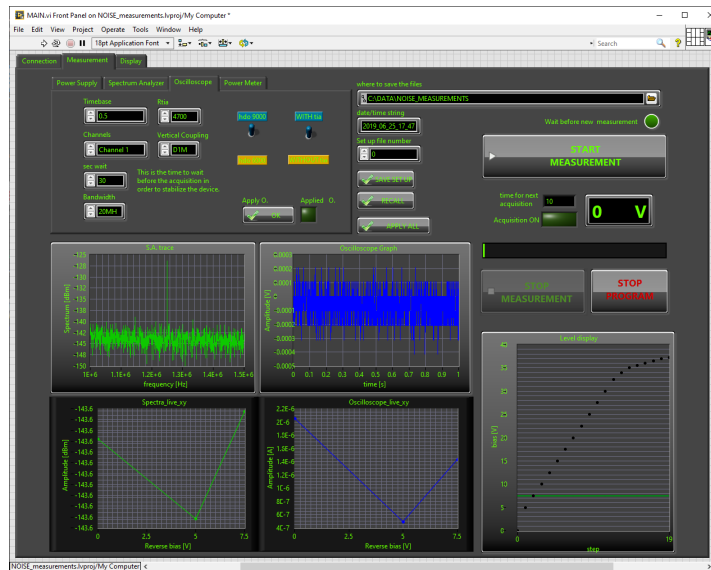


Figure 4.25: Main panel of the virtual instrument developed in LabVIEW to control the electronics to perform IV scans.

EXPERIMENTAL RESULTS

Several simulations were run and several devices were fabricated: each of the devices has been characterized by different concentrations in the separation layers between the absorption and the multiplication layer, different number of steps in the multiplication region, different absorption region widths or different diameter of the mesas. All of the above characteristics were utilized to study distinct aspects of our structure, which are presented in this chapter. In particular, the discussion on the optimization of the doping concentration in the p-doped separation layer is introduced in section 5.2. The influence of the number of steps on the APDs performance is shown in section 5.3, where time response, noise and spectroscopic measurements will be presented. Section 5.4 depicts the response of the devices to soft and hard X-ray irradiation. Moreover, some other minor considerations are disseminated throughout the chapter.

5.1 EBHDM SIMULATIONS

The EBHD model, presented in Ch. 2, which is assuming abrupt doping profiles, was applied on a realistic structure: the staircase SAM-APD, inspired by [45].

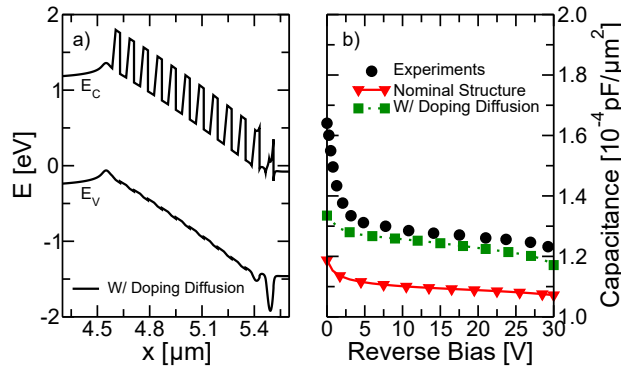


Figure 5.1: (a) Band diagram of the multiplication region of our device when a bias of 0 V is applied. (b) Comparison between experimental (circles) and simulated CV characteristics of the staircase SAM-APD in [45]. The nominal structure with abrupt doping profiles is compared with a case considering out-diffusion of the n+ bottom layer.

In this specific case, the nominal structure simulated consists of an absorption region, separated from the multiplication region by a δ -p doping layer. The multiplication region, whose total length is 1 μm ,

is a periodic repetition of a structure composed of 20 nm $\text{Al}_x\text{Ga}_{1-x}\text{As}$ (x from 0 to 0.45), 25 nm of $\text{i-Al}_{0.45}\text{Ga}_{0.55}\text{As}$, and 35 nm of i-GaAs . Finally, a 200-nm n-GaAs layer is placed between this structure and the $\text{n}^+\text{-GaAs}$ substrate.

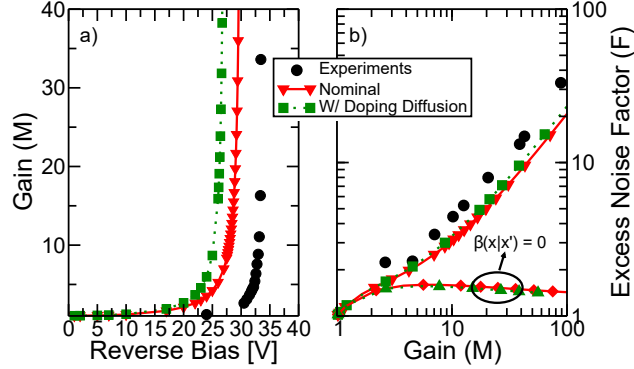


Figure 5.2: (a) Simulated and measured gain versus voltage and (b) excess noise factor versus gain for the staircase APD. The experimental results are taken from [45] and [4]. The structure in [4] slightly differs from the one in [45], but the EBHDM, with the model parameters of Table I in [22], gives the same $F(M)$ curve for both of these devices.

The data utilized in order to run the EBHD model were extrapolated by Sentaurus TCAD [28]. An example of an output of these simulation is depicted in Fig. 5.1a, which shows a band diagram of the above-mentioned structure. The conduction band steps are quite pronounced, while the ones in the valence band are rather small. Since the energy barriers seen by the electrons are quite thick (45 nm) and include a graded region, tunneling is not accounted for in the model used. Other simulated CV curves extracted from TCAD are reported in Fig. 5.1b: the out-diffusion of dopants from the bottom n^+ region towards the multiplication layer, thus assuming a smaller depletion width, was assumed to match experiments with simulations. Default values provided by the simulator [28] were assumed for the dielectric constant of different layers and for the band discontinuities amplitude. We applied the EBHDM by using the E_C and E_V profiles as inputs, like the one in Fig. 5.1a, obtained again from drift-diffusion TCAD simulations by using the Thermionic Emission Current model for transport at the heterojunctions. The model parameters for an arbitrary mole fraction of Al in $\text{Al}_x\text{Ga}_{1-x}\text{As}$ were linearly interpolated from Table I found in [22]. The gain versus voltage and excess noise versus gain curve are reported in Fig. 5.2a and 5.2b. The agreement between simulated and measured gain versus voltage is not perfect, while the excess noise versus gain is reproduced quite well. Due to the large electric field, hole impact ionization has a substantial impact on the results as demonstrated by the comparison with the curves for $\beta(x|x') = 0$, which means that no impact ionization caused by the

holes happens. If the contribution of holes (Fig. 5.2b) is switched off in the model, the excess noise is always below 2 even at high gains. These results confirm that low-noise performance requires high-energy steps compared to the gap of the material where multiplication takes place.

The comparison performed so far was done with the experimental results found in [45] and [4]. In the next sections, further comparisons between the simulations made through the EBHD model and the data acquired with our devices will be discussed.

5.2 DIFFERENT δ -DOPING CONCENTRATIONS

As pointed out in section 1.2.3, the p-doped layer separating the absorption and the multiplication region has an important role in the SAM-APDs. In fact, it ensures that after applying a reverse bias the vast majority of the potential drops mostly in the multiplication region. Section 3.3 shows how to grow such layer and calibrate its effective acceptor density. As the δ p-doped C layers are highly compensated (section 3.3.1) the actual acceptor density is lower than the amount of C delivered by the effusion cell. Compensation takes place in thin GaAs:C layers as well, although to a lesser extent. The maximum achievable planar acceptor densities in δ p-doped C layers and in 50-nm GaAs:C layers grown were found to be $2.5 \cdot 10^{12} \text{ cm}^{-2}$ and $1.2 \cdot 10^{13} \text{ cm}^{-2}$, respectively.

According to table Table 3.1 and as depicted in Fig. 3.12 several devices were grown changing the acceptor concentration of the separation layer. The characteristics of the six different samples are summarized in Table 5.1: they all feature a δ layer with the exception of device F, the one with the highest density, which features a 50-nm-thick layer (as mentioned above, this happens because such concentration is not reachable with the δ configuration). From here on, all the cases will be referred generally as δ p-doped layers, unless otherwise specified.

Device	A	B	C	D	E	F
Density [cm^{-2}]	$8.8 \cdot 10^{10}$	$5.0 \cdot 10^{11}$	$1.3 \cdot 10^{12}$	$1.6 \cdot 10^{12}$	$2.5 \cdot 10^{12}$	$6.0 \cdot 10^{12}$

Table 5.1: Acceptor densities for the p-doped layer, measured with Hall effect: δ layers were employed for devices of the type from A to E, while a 50-nm-thick layer was employed for device F.

5.2.1 Dark characteristics

A first way to study the effect of the acceptor concentration in the δ p-doped layer was through the capacitance-voltage (CV) characteristics, which provide information about the electric field and potential distribution inside the devices. These measurements were performed with a precision LCR meter (HP4284A) at 1 MHz.

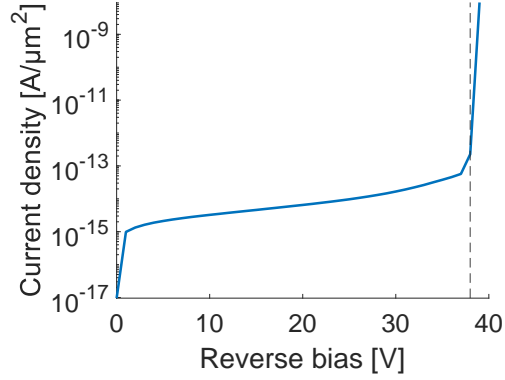


Figure 5.3: Dark current density value for a device of the E type.

Before testing for their CV, the devices were tested in dark by measuring their current-voltage (IV) characteristics. This step allowed to select devices with the lowest leakage. An example of IV is reported in Fig. 5.3: it shows typical current density values.

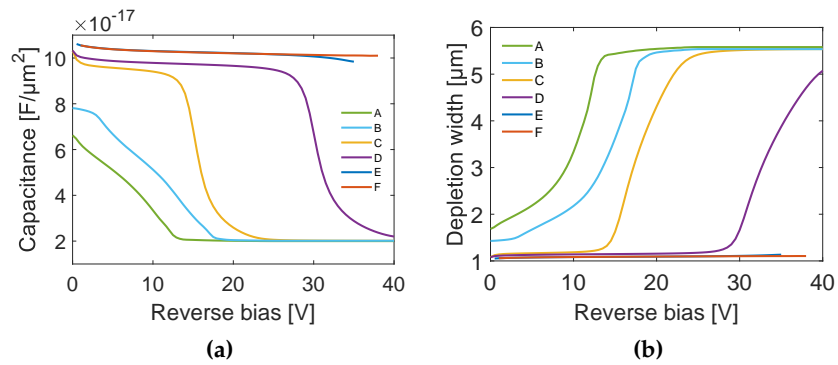


Figure 5.4: Capacitance and corresponding depletion width versus reverse bias for different devices.

Figure 5.4a shows the capacitance per area as a function of the applied voltage, while Fig. 5.4b shows the depletion width calculated as

$$d = \frac{\varepsilon_r \varepsilon_0 A}{C} \quad (5.1)$$

where A is the area of the mesa, C is the measured capacitance, $\varepsilon_r = 12.6$ [19] and $\varepsilon_0 = 8.854 \cdot 10^{-12}$ F/m are the equivalent relative permittivity of the active region (calculated as the mean value of the permittivity as a function of the depletion width) and the permittivity of vacuum, respectively.

It can be seen that for the two highest carbon concentration in the δ p-doped layer (samples E and F) the capacitance is almost constant over the entire range of the reverse biases, up to breakdown. In these conditions, the depletion width corresponds to the thickness

of the multiplication region. This means that this amount of carbon atoms is able to prevent the formation of a large electric field in the absorption region by confining the drop of the applied potential inside the multiplication region only, and it also allows the devices to undergo breakdown and work as expected.

Conversely, in the samples with lower doping levels the capacitance drops at a certain bias, meaning that the applied potential depletes not only the multiplication region but also part of the absorption region. In particular, the depletion region of most of the devices with lower doping reached at some voltage a depletion width of $5.5 \mu\text{m}$, which is the full thickness of the grown structure confined within the n-p contact layers. The voltage at which this drop occurs increases with the dose of the δ p-doped layer. To confirm this interpretation, we reproduced the CV curves of samples C, D, E and F with TCAD simulations [28]. Fig. 5.5 shows that experimental and simulated data are in good agreement; in particular, the concentration of acceptors in the δ p-doped layer obtained from the simulations fairly approximates the values measured by Hall effect (Table 5.1) when a similar trend is met.

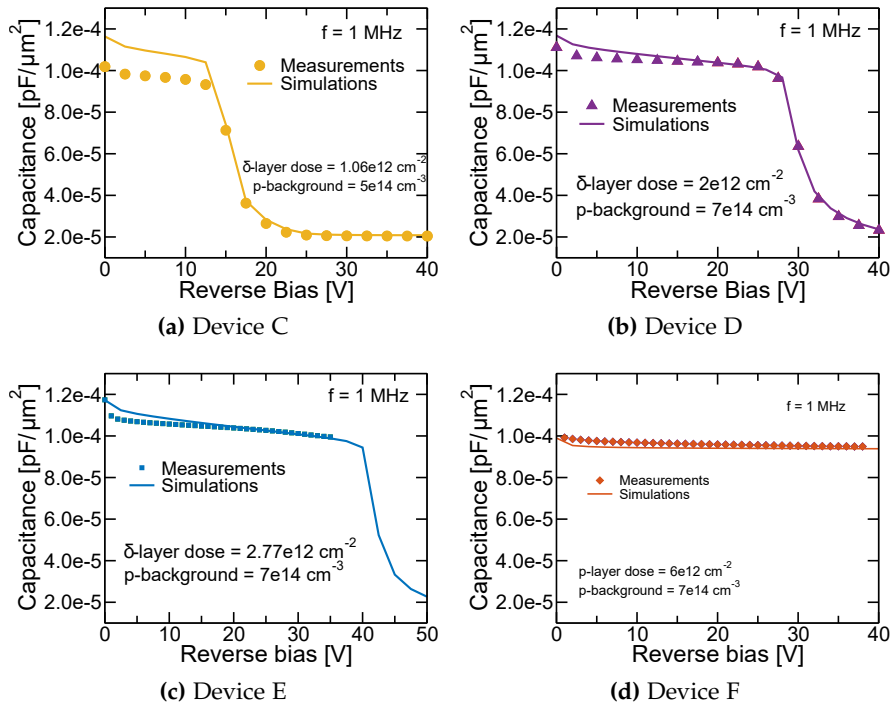


Figure 5.5: Comparison between experimental and simulated CV curves for devices characterized by different concentrations of carbon in the separation layer between the absorption and multiplication region. In the simulation, the δ -layer dose is equal to the actual concentration of acceptors realized in the sample, while the p-background is the residual acceptor concentration present in the absorption region.

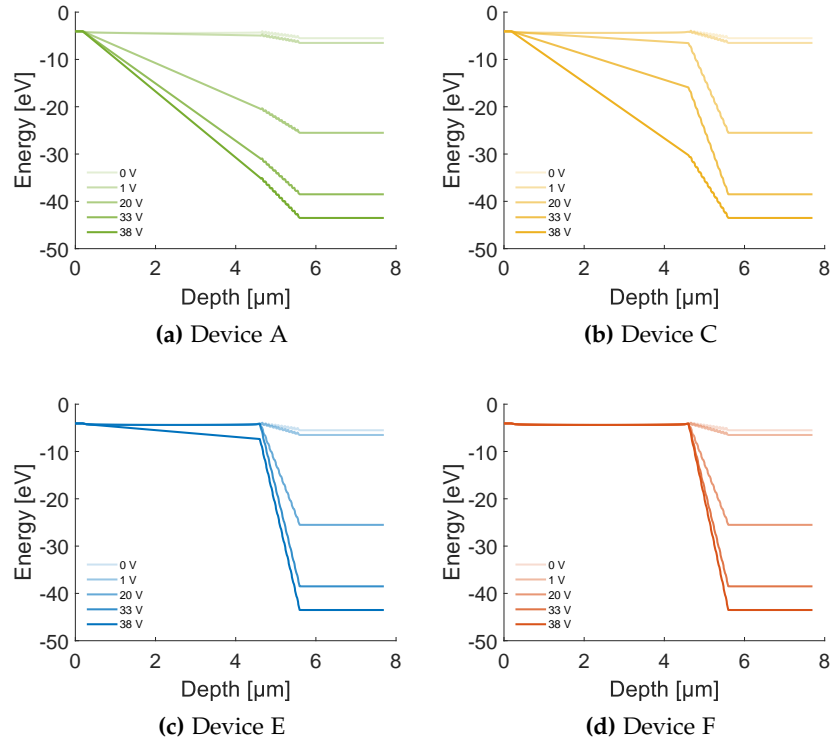


Figure 5.6: Conduction band diagrams of devices A, C, E and F for 5 different reverse biases.

The band profiles of the prototype structure under study was also simulated with the SimWindows32 Simulator [61]. Fig. 5.6 reports the conduction band profiles simulated at different biases for samples of the types A, C, E and F, to illustrate the dependence of the depleted zone on the acceptor level in the δ p-doped layer. A similar behavior can be noticed also for the valence bands, which are not reported here. In these curves, the bands corresponding to the absorption region expand to a depth of approximately $4.5 \mu\text{m}$, from there on the multiplication region starts. It can be seen that for the highest doping (device F), the first part of the curves (corresponding to the absorption region) is flat for all the biases and it presents the same value, while for lower doping levels, this does not occurs and their slope becomes noticeably accentuated implying the creation of a potential drop in the absorption region. This could explain why the CV characteristics (Fig. 5.4) of the devices with lowest doping (device A and B) do not start at a capacitance value corresponding to a $1\text{-}\mu\text{m}$ -thick depleted zone (i.e. the multiplication region), but they are already affected by the partial potential drop in the absorption region. At higher biases this effect is amplified and at 33 V the absorption region is fully depleted for both samples A and C. Conversely, in sample E the depletion is confined to the multiplication region for almost all biases. In fact, near the breakdown (i.e. 38 V) the conduction band is slightly tilted,

which allows the device to work properly (as it will be shown in the following paragraphs).

In conclusion, for device **A** the drops increase starting from 0 V with the biases, meaning that the doping of the separation layer is ineffective in shielding the external bias and in keeping the vast majority of the field just in the multiplication layer. For devices of the **C**-type the drop does not appear until higher biases are applied, suggesting that the presence of the δ layer starts to show its efficacy, though not over the entire range of operation. Finally, for devices **E** and **F** the potential drop does not appear with the exception of the voltage near the breakdown for device **E**.

The small differences in the band profiles of the **E**- and **F**-type prototypes influence also the high-bias capacitance of such devices. The main difference can be appreciated by having a closer look at their CV curves, shown in Fig. 5.7. The two CV curves are almost coincident up to approximately 25 V, above which a small drop of sample **E** capacitance is noticeable (a drop which corresponds to a 40 nm increase in the depletion width) with respect to sample **F**.

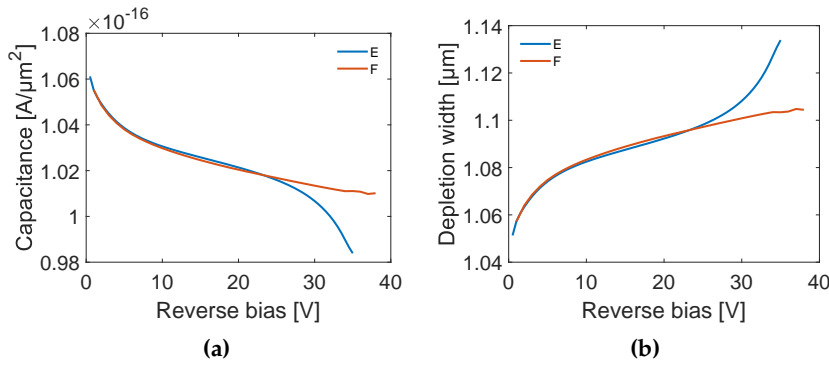


Figure 5.7: (a) Experimental CV characteristics of samples with a δ separation layer with a planar acceptor density of $2.5 \cdot 10^{12} \text{ cm}^{-2}$ (**E**) and a 50-nm separation layer with a planar acceptor density of $6.0 \cdot 10^{12} \text{ cm}^{-2}$ (**F**). (b) The respective depletion widths.

As a further analysis looking closer into the shape of the CV curves, it is possible to calculate the profile of the p-dopant concentration inside the device, $P(w)$, by using the equation for general nonuniform distributions [9, 62]

$$\frac{d(1/C_A^2)}{dV} = \frac{2}{q\epsilon_r\epsilon_0P(w)} \quad (5.2)$$

where C_A is the capacitance per unit area of the mesa, V is the applied bias, q is the elementary charge and w is the depletion width related to C_A . Since we are probing values of w in the proximity of the width of the multiplication region, we are sensitive to the charge distribution around the p-doped layer.

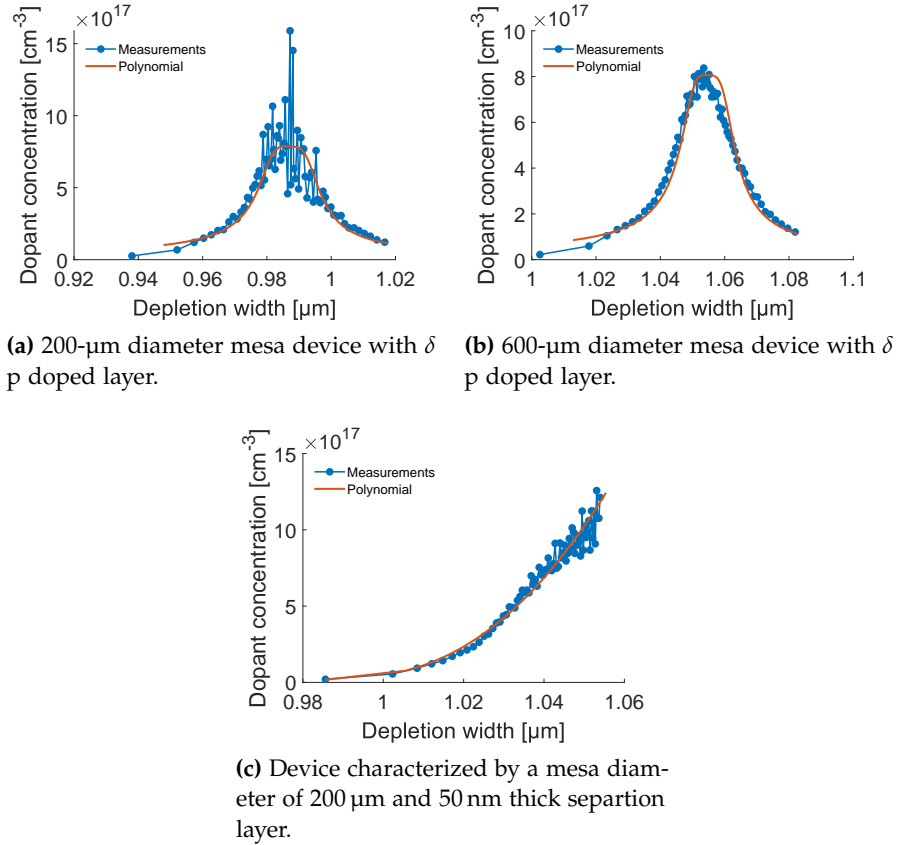


Figure 5.8: Dopant concentration as function of depletion width for two devices of the E-type, characterized by having diameters of 200 μm (a) and of 600 μm (b), and one of the F type (c) having a diameter of 200 μm .

Figure 5.8 shows the results of this extrapolation, where the dopant concentration is plotted as a function of the depletion width: the blue dots represent the values obtained from the measured capacitances, while the red line shows the results obtained with a polynomial fit of the inverse of the capacitance optimized with the least squares method, by using Equation 5.2. The polynomial fit was introduced in order to obtain (after differentiation) noiseless reference curves, which show the profile also where the measured data become noisy. From these analyses it follows that in the case of the 50-nm separation layer (Fig. 5.8c) the dopant concentration as a function of the depletion region grows monotonically. This trend testifies how the layer shields the absorption region in a way that the field has no measurable effect beyond the p-layer, at least within the voltages of operation. On the other hand, in the δ case the carrier concentration has a bell shape due to the drop in capacitance, which starts to occur in the devices with a just sufficient carbon concentration (Fig. 5.8a and 5.8b) meaning that in this case we start depleting beyond the δ -layer in the absorption region as seen in Fig. 5.7. It is possible to compare the area under the curve with the dose of carbon atoms, which is nominally inserted

in this layer ($2.5 \cdot 10^{12} \text{ cm}^{-2}$). The areas have a value of $2.4 \cdot 10^{12} \text{ cm}^{-2}$ and $2.1 \cdot 10^{12} \text{ cm}^{-2}$ calculated from Fig. 5.8a and 5.8b, respectively.

5.2.2 Light response

The fabricated devices were tested under light to assess their response to incoming photons. Two different light sources were used to test the influence of the δ p-doped layer: the IOM-CNR BEAR beamline at the synchrotron Elettra (Trieste, Italy) [50] in the energy range 500-800 eV and a green ($\lambda = 532 \text{ nm}$) tabletop laser, both described in section 4.1.

The photon energy range was selected in order to ensure that photogeneration took place entirely within the absorption region, thus studying just the sole multiplication effect, without having it combined with charges generated in the multiplication region. In fact, the absorption length is 200 nm and 586 nm at 500 eV and 800 eV, respectively, calculated using [63] whose reference is [64], while it is approximately 160 nm for the laser (section 4.1.2).

For both light sources the response to photons was calculated as the difference between the dark and the photocurrent. Moreover, to compare the responses, as different light sources and different fluxes were employed, the gain M was defined as the signal (I_{ph}) normalized by its value at 20 V (I_{ph0}):

$$M = \frac{I_{ph}}{I_{ph0}} \quad (5.3)$$

where the reference value was chosen as the multiplication does not take place yet; thus we can consider $M = 1$ as the point at which the device has just reached full charge collection.

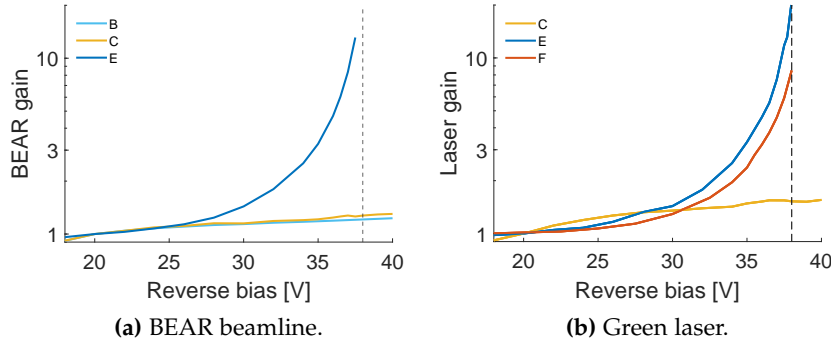


Figure 5.9: Gains of devices with different areal density of the δ p-layer measured at the BEAR beamline averaged over seven different energies in the 500-800 eV range (left), and with the green laser (right). The breakdown voltage of device E (38 V) is marked by a dashed line.

Devices B, C and E were tested at the BEAR beamline and Fig. 5.9a reports the gains of such devices. These curves are averaged over seven

different energies in the 500-800 eV range. It can be noticed that the multiplication for the low-doping structures is minimal, while with a sufficient doping it is clearly visible and reaches a value of 13.1 at 37.5 V.

The gain of the devices **C**, **E** and **F** was measured also under laser light. Looking at the data (Fig. 5.9b), device **E** shows the same behaviour as the one observed on the BEAR beamline, exhibiting a gain of 11.8 at a reverse bias of 37.5 V and a maximum gain of 21 at 38 V. Gains measured with the two light sources coincide numerically within 10%; this is probably due to the fact that in both cases electrons undergo the same multiplication processes being generated in the first few 100 nm of the absorption region. In the case of device **F**, instead the gain results to be 8.5 at 38 V.

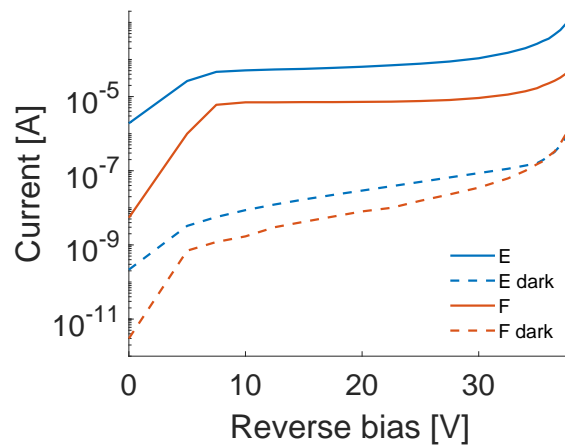


Figure 5.10: Currents for device **E** (blue) and **F** (red) as a function of the applied reverse bias. The dashed lines are the respective dark currents.

The gain of device **F** is slightly lower with respect to device **E**, as can be seen in Fig. 5.9, and also in the case of photocurrent and dark current curves of both devices (Fig. 5.10) it results that the absolute values of the photocurrent are higher in the case of device **E** even though the photon flux during the acquisition was slightly lower (1400 μW vs. 1600 μW). This could be explained as device **E** presents a residual field in the absorption region, which allows the created electrons to drift more easily toward the multiplication region, providing a better collection above 25 V, where the CV curves start to differentiate (Fig. 5.7). When lower biases are applied, no field forms, thus the charge carriers move by diffusion only.

As can be noticed, even in this regime device **F** still exhibits a smaller charge collection efficiency and thus a smaller photocurrent. One factor which contributes to this problem could be the different potential barrier created by the p-doped separation layer in the conduction band. In fact, it can be seen in the simulated band profile in Fig. 5.11 that for device **F**, characterized by a higher p-doping level, electrons

need to overcome a larger potential barrier with respect to those of device **E**, which presents a lower doping. This behavior can be noticed at all biases.

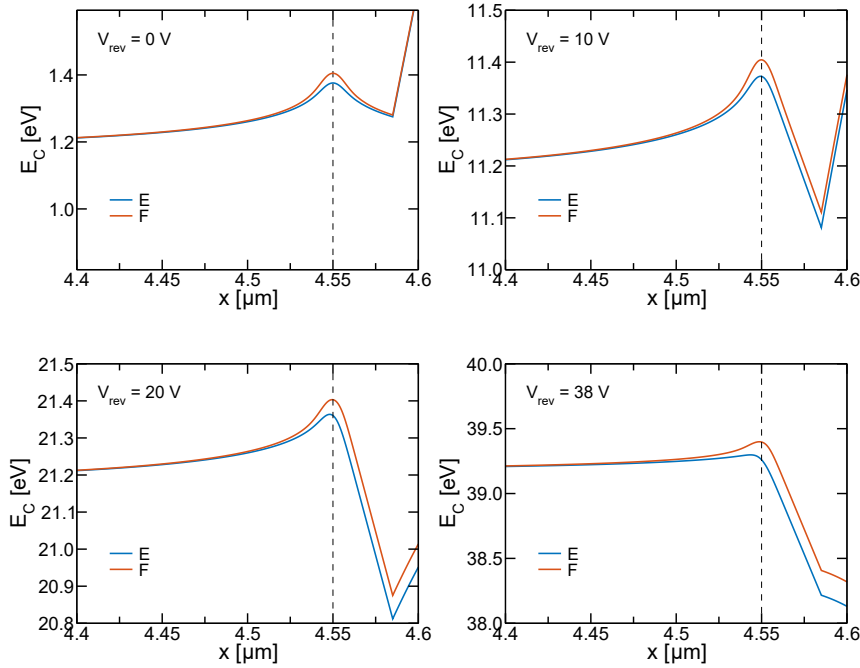


Figure 5.11: A detail of the simulated conduction band profile of the SAM-APD structure taken in the surroundings of the layer which separates the absorption and multiplication regions at different biases. Such position is indicated by the vertical dashed line. The device **F** (red curves) possesses always higher values with respect to **E**, meaning that the electrons need a higher energy to reach the multiplication region in the first case compared to the latter one.

In conclusion, devices of the **E**-type, having a planar $2.5 \cdot 10^{12} \text{ cm}^{-2}$ concentration of carbon atoms in the δ p-doped separation layer, are the optimal ones. This concentration is enough to confine the potential drop in the multiplication region enabling the multiplication process, and still it lets a small residual field be established, which seems beneficial for the collection efficiency, whereas a higher concentration results as an obstacle. Considering all of the above, the samples which will be taken into consideration during the following of this thesis are the **E**-type ones.

5.3 DIFFERENT NUMBER OF STEPS

There are different parameters that can be modified in order to improve the performances of the SAM-APDs under study. Once the optimum separation layer had been found, the number of steps of the multiplication layer were investigated. Some simulations using the

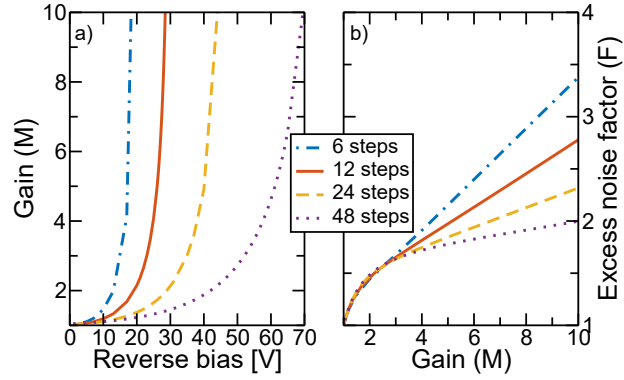


Figure 5.12: Simulation of the gain as a function of the reverse bias (left) and the excess noise factor as a function of the gain (right) for devices characterized by 6, 12, 24 and 48 steps.

EBHD model described in Ch. 2 were run varying this parameter. The calculations were carried out for devices characterized by 6, 12 and 24 repetitions of the main stage which, as described in section 3.3, is composed by 25 nm of GaAs, 25 nm of $\text{Al}_{0.45}\text{Ga}_{0.55}\text{As}$, and 25 nm of linearly graded $\text{Al}_x\text{Ga}_{1-x}\text{As}$.

As it can be seen in Fig. 5.12 the simulations suggested that the noise associated to the multiplication process expressed through the excess noise factor (F) decreases for a given value of gain (M), when the number of steps is increased.

5.3.1 Noise measurements

Initially, the devices needed to be tested under dark conditions to assess their reliability and to check if they worked properly.

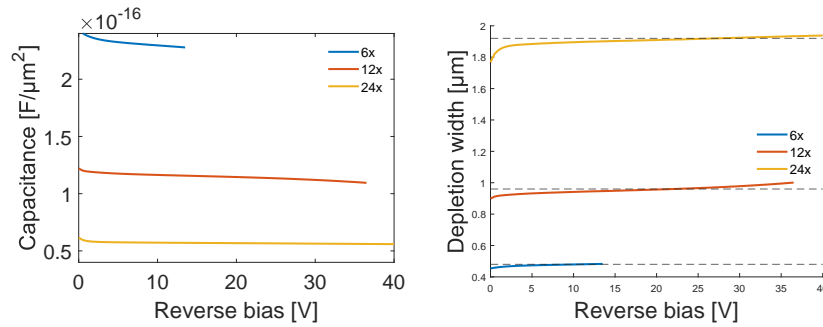


Figure 5.13: Measured capacitance (left) and depletion width (right) as a function of the reverse bias for devices with 6, 12 and 24 steps.

Figure 5.13 shows the measured capacitance normalized for the devices' areas and the corresponding depletion widths calculated accordingly through equation 1.13. As the single step is made of 80 nm, the thicknesses of the multiplication region are 480 nm, 960 nm

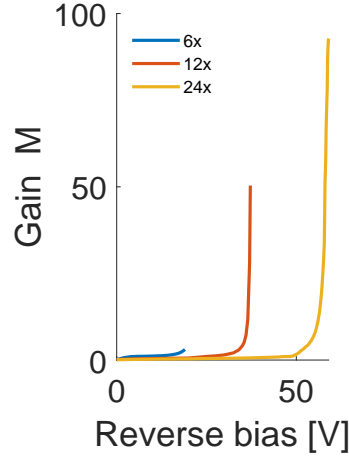


Figure 5.14: Gain as a function of the bias for devices characterized by different number of steps.

and 1920 nm for the 6-, 12- and 24-step devices, respectively, as can be seen also from the depleted widths in Fig. 5.13b.

As described in section 4.2.2.1 the system built for measuring gain and excess noise factor was based on a transimpedance amplifier, which converts the current of the photo-detector into a more convenient voltage signal. For these measurements the device under test was kept in a stainless-steel and UHV-compatible dark chamber whereas the APD was illuminated by the CW Millenia tabletop laser (section 4.1.2). Again the green laser was selected such that the photo-induced charge generation was limited to the absorption region only [65], so as to have ideal conditions of charge injection close to the entrance window in the absorption region during noise characterization.

Currents and noise power spectra measured while the device was illuminated by the laser were used to calculate M and F . Figure 5.14 shows the gain as a function of the bias. The gain is defined, as already expressed in eq. 5.3, as

$$M = \frac{I_{ph}}{I_{pho}} \quad (5.4)$$

where I_{ph} is the difference between the measured photocurrent and the current measured under dark conditions and I_{pho} is the photocurrent at unity gain.

The noise generated under illumination is expected to differ from the noise under dark conditions; this difference can be used to characterize the noise associated with the avalanche gain process which multiplies the photocurrent [66]. In fact, the excess noise factor F can be defined through the ratio between the power spectral density of

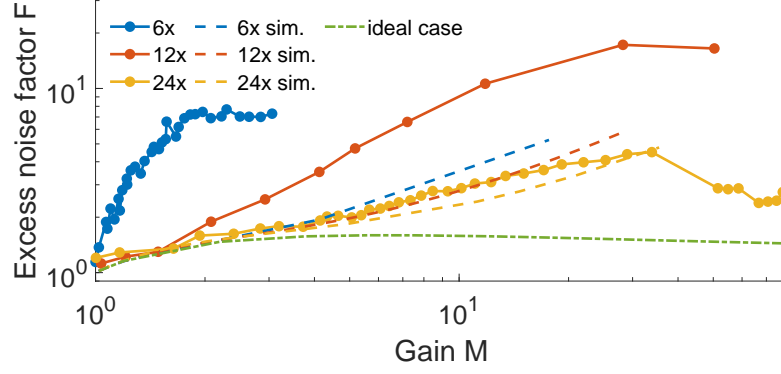


Figure 5.15: Excess noise factor as a function of the gain for devices characterized by a different number of steps: 6 (blue), 12 (red) and 24 (yellow). The dashed curves represent the simulation performed with the EBHD model, while the continues and dotted ones are the measured data. The green dotted line represents instead a simulation of an ideal case with total suppression of the hole multiplication.

the photogenerated current ($S_{ii,ph}$) and the power spectral density of the shot noise ($S_{ii,shot}$):

$$\frac{S_{ii,ph}}{S_{ii,shot}} = \frac{2qIRFM^2}{2qIR} = FM^2 \quad (5.5)$$

where q is the elementary charge, I is the photocurrent at unity gain and R is the load resistance.

Processing this expression and considering that the signal is entering the 50Ω input resistor of the spectra analyzer, F can also be expressed as

$$F = \frac{S_{ii,ph} - S_{floor}}{2qB \frac{R_f^2}{R_{in}} M^2} \quad (5.6)$$

where B is the spectrum analyzer bandwidth, M is the gain calculated as mentioned above (equation 5.3), $S_{ii,ph}$ is the spectra acquired under illumination, S_{floor} is the noise floor spectra, R_f is the feedback resistance of the TIA and R_{in} is the input resistance of the spectrum analyzer.

In order to validate the excess noise estimations obtained through the laser measurements, the resulting values of F were compared with the ones obtained by simulating the nominal structure with the Energy Balance History-Dependent (EBHDM) model (presented in [22] and explained in Ch. 2 with nominal device parameters as in [4]).

Figure 5.15 compares these results by plotting F as a function of M . By applying a multiplicative factor it was possible to position the measured curves such as the excess noise factor would be set as unity where no multiplication takes place, or rather where M is equal to 1, as it results from the definition of the excess noise factor. This is necessary

because there are probably other noise sources amplified during the multiplication process, which are not considered in equation 5.6. In fact, we considered only the shot noise, but additional possible noise sources could influence the process (e.g. the laser fluctuations, the trap effect in the absorption region due to the use of GaAs). Unfortunately, a way to quantify this noise was not found simultaneously with the data acquisition.

Quantitatively the simulations and the measurements do not match completely and the simulations underestimate the measurements especially for the samples with 6 and 12 steps. However, in all the cases they follow the expected behavior; in fact, F decreases for a specific gain as the number of steps increases. As the gain increases it can be observed that the excess noise factor reaches a maximum value and then it drops in all of the three cases. In the device with 24 steps this behavior is more evident. This could be related to a more efficient suppression of the hole multiplication as the field in the multiplication region increases with M . Indeed, in the ideal case (Fig. 5.15, green curve) where no holes undergo impact ionization and only electrons are multiplied the non-monotonic trend can be seen.

5.3.2 Time response

As described in section 4.2.2.1 the setup to acquire the time response measurements used the second harmonics ($\lambda = 532$ nm) of the infrared fiber ytterbium-doped laser (whose specifications may be found in section 4.1.2).

The time responses were recorded for two devices of each set characterized by a different number of steps, over a range of biases from 0 V to the breakdown voltage. Some of these curves are shown in Fig. 5.16: the offset due to the dark current, which is increasing as the applied voltage increased, was subtracted.

The parameter used to compare such curves was their rise time, which was calculated as the time it took for the response pulse to pass from 10% to 90% of their maximum. It resulted that the 6-step devices have a rise time of approximately 1 ns, the 12-step of 100 ps and the 24-step ones of 80 ps (values are summarized in Table 5.2).

It can be notice that these two last values are unexpectedly similar, probably because they are not much higher than the shortest rise time achievable with such oscilloscope (bandwidth 12.5 GHz), which based on the first-order model of a low-pass system is 28 ps. Moreover, these values are somehow further limited by the cables (U.FL cables have guaranteed reliability up to 6 GHz) and other setup non-idealities. It must be also pointed out that such values were calculated based on few points laying within the range of 10% to 90% of the maximum and this could also influence the uncertainty of the outcome results. Thus, it can be concluded that the time responses for such devices

The first-order model leads to a rise time given by $\Delta t_{.1-.9} = \frac{0.35}{f_{co}}$, where f_{co} is the cut-off frequency of the oscilloscope.

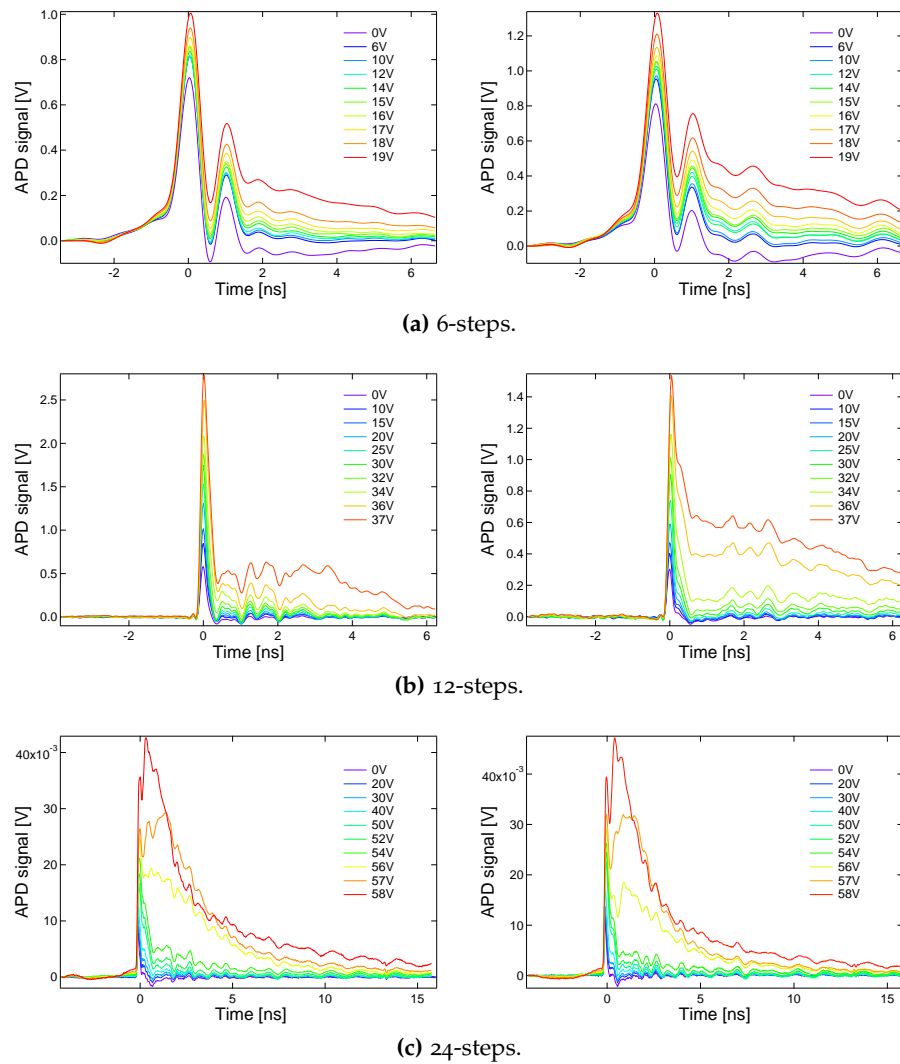


Figure 5.16: Time response of devices characterized by 6, 12, 24 steps. The color scale varying from violet to red shows different applied biases.

are on the limit of possibilities of the instrumentation and must be considered only as an upper limit.

Some assumptions can also be made about the shape of the time responses: it can be noticed (Fig. 5.16) that the peaks have a width of some ns or tens of ns, perhaps owing to the holes generated during the II mechanism near the n-contact that still have to reach the p-contact as the Ramo theorem suggests. Moreover, a smaller peak which is not influenced by the multiplication is visible at lower biases. It is very sharp and does not change in width neither in amplitude, which suggests that it is generated likely in the absorption region and in particular as the time of arrival is very short in the p-GaAs/GaAs interface. At higher biases it gets covered by the peak, which instead is multiplied. In the case of the 24-step devices is more evident that the rising edge can be associated to electrons traveling across the absorption region until they reach the multiplication region, while

the falling edge, following an RC discharge shape can be due to the electrical characteristic of the diode.

The main peaks are generated in depleted areas of the semiconductor where the field is higher and they increase as the applied voltage increases meaning that they are somehow multiplied. Thus, the area subtended by each response from Fig. 5.16 acquired with the oscilloscope was integrated. By using equation 5.3 and substituting the currents of such formula for the aforementioned areas in volts, the gain as a function of the bias was calculated. Figure 5.17 shows the trend of the gains calculated in this way: their values are in qualitative agreement with the ones obtained by using a continuous laser. In fact, as the number of steps is increased the maximum gain grows. Table 5.2 at the end of this section will summarize such comparison.

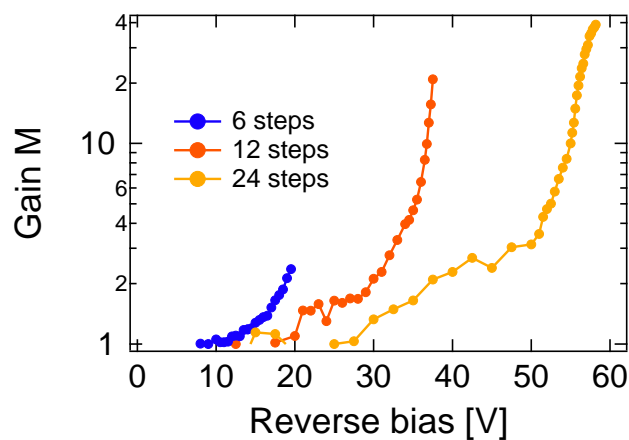


Figure 5.17: Gain as a function of the reverse bias, extrapolated from the areas under the time waveforms.

5.3.3 Spectroscopic measurements

In order to evaluate the capabilities of our detector in spectroscopic applications some preliminary tests have been carried out. The setup was the one described in section 4.2.2.1 and the charge sensitive amplifier used was the CUBE (section 4.2.1.2). The pulsed green tabletop laser (pulse width 100 fs, repetition rate 200 kHz, $\lambda = 540$ nm) described in section 4.1.2 was selected to emulate an X-ray single photon source; as previously noted, this wavelength is absorbed within few hundreds of nm and it could be used as an external trigger by diverting part of the laser beam to a commercial silicon-based photodiode. The incident power of the laser during this measurements was $28 \mu\text{W}$.

500 single responses to these ultra-short pulses for each reverse bias and for each type of device (with 6, 12 and 24 steps) were collected. Figure 5.18 shows an example of the signals at the CUBE electronics output, which are then fed to the shaper and finally recorded by the

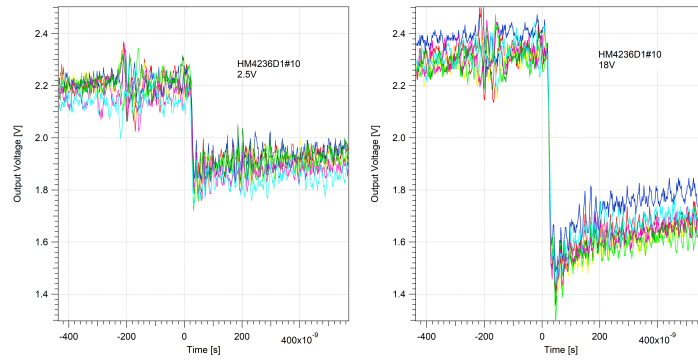


Figure 5.18: Examples of a few signals acquired before the shaper with a 6-step device for different biases: 2.5 V (left) and 18 V (right).

oscilloscope. Considering that the area below the curve of each single response is proportional to the charge deposited by a single event (in this case, a single pulse of photons), the histograms of such areas were calculated and plotted in Fig. 5.19.

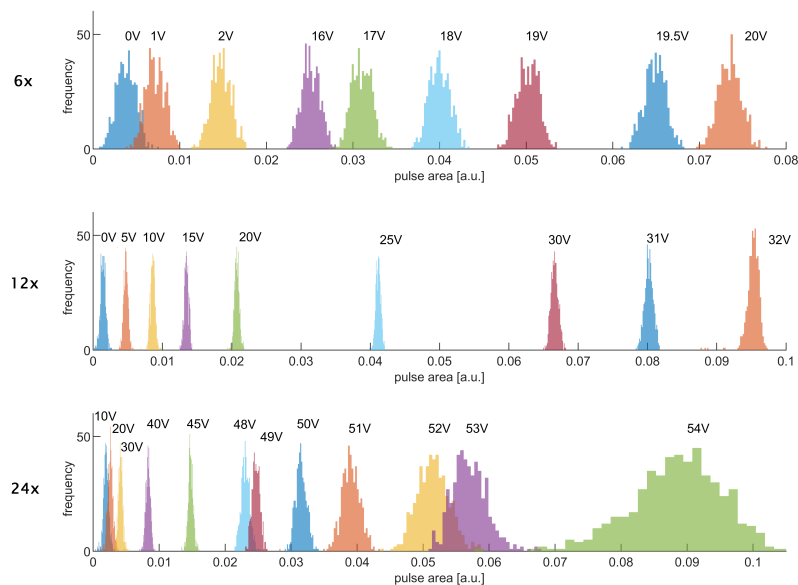


Figure 5.19: Histograms of the area of the pulses resulting from the shaper expressed in arbitrary units, normalized both in area and frequency to highlight the variation of the standard deviation, for devices with 6, 12 and 24 steps, respectively. The different colors are used to indicate distributions taken at a given reverse bias. The 6-step device is limited by the noise of the set up, in fact, the FWHM is almost constant for all biases; instead in the 12- and 24-step devices the multiplication noise becomes more evident, an increase in the FWHM can be noticed, strongly for the latter.

It can be noted that the device characterized by 6 steps is limited by the noise of the set up, in fact, the FWHM is almost constant for all

biases; in the device with 12 steps the multiplication noise becomes more evident, a minimum increase in the FWHM can be noticed; finally, the histograms of the device with 24 steps depend strongly on the gain of the device as it can be seen by the FWHM at higher biases which are evidently larger.

For each distribution of the pulse area at a given reverse bias the mean value was calculated. Figure 5.20 shows the gain as a function of the reverse bias voltage calculated through the mean value of the area below the response curve (by using equation 5.3, substituting currents for areas). The unity gain was set at the reverse bias voltage at which the dependence of the area on the reverse bias saturated, the full charge collection regime was reached, but the multiplication did not start yet.

Also with these measurements it is possible to see that the gain increases with the number of steps. This trend is in agreement with the results obtained from two previous types of measurements, as summarized in Table 5.2.

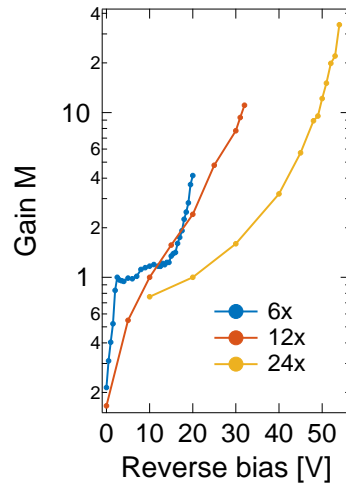


Figure 5.20: Gain as a function of the reverse bias extrapolated from the area under the acquired shaper responses for devices with different number of steps.

Steps	Capacitance [10^{-16} F μm^{-2}]	CW laser		Pulsed laser		CUBE		Rise time
		M_{max}	@	M_{max}	@	M_{max}	@	
6	2.2	3.1	19 V	2.7	19.5 V	4.14	20 V	1 ns
12	1.1	50.4	37.2 V	20.7	37.5 V	11.1	32 V	< 100 ps
24	0.55	92.8	59 V	39.1	58.2 V	34.1	54 V	< 80 ps

Table 5.2: Summary of the maximum gain obtained using different sources and setups for devices characterized by different numbers of steps. The results are extrapolated from measurements performed with continuous and pulsed lasers in different configurations: noise, time response and spectroscopic configurations. The last column summarizes the rise time obtained.

SUMMARY: DIFFERENT NUMBER OF STEPS Table 5.2 compares the results obtained so far with different setups for different numbers of steps in the multiplication region. The trend is the same in all the cases (an increase in the gain as the number of steps grows can be observed), however, there is a quantitative discrepancy among the results. The gain from the time response is systematically smaller than the one obtained under the continuous laser. This behavior could be due to a worse collection efficiency of electrons generated by the ultra-short laser pulses. Being generated in a short time range, they are also spatially near and create a dense bunch of electrons. This at some biases could create a significant local electric field shielding the external bias (space-charge effect), thus partially preventing further increasing in the multiplication effect.

5.4 X-RAY RESPONSE

Responses to X-rays to analyze a specific aspect of our devices have been already shown in this chapter (section 5.2.2), as they were used to prove and study the efficacy of the δ layer. Here, other results obtained both with soft and hard X-rays are presented.

5.4.1 *Soft X-rays*

TWINMIC Some devices characterized by 24 steps (type F) were tested at the TwinMic beamline. The utilized light source and setup were described in section 4.1.1.1 and 4.2.2.2, respectively. These measurements consisted of spectroscopic analysis, performed with the detectors already available at the beamline, and photo-generated current measurements, performed with our devices.

An example of spectroscopic measurement carried out at such beamline, showing the distribution of the different materials in our device, is reported in Fig. 5.21. This measurement was performed with a beam characterized by an energy of 1750 eV, over an area $200 \times 200 \mu\text{m}^2$, with a spot size of $3 \mu\text{m}$. As expected gallium and arsenic are spread all over our structure, made of GaAs, equally; the oxygen (which is a component of the Al_2O_3 dielectric layer) is distributed everywhere but on the opening of the mesa. Aluminum, instead, presented some visualization problems; in fact, the aluminum bonding tampers with the counting and in the area where it is placed its signal is stronger than the one from the rest of the device. Thus a logarithmic scale was employed, and from this it is possible to notice that aluminum is present everywhere, with a higher concentration in the bonding area and in the lateral side of the staircase where it is expected to be.

The distribution of the materials together with the map of the photocurrent of a given device helped us analyze how some sections absorbed photons differently, in order to quantify the different collec-

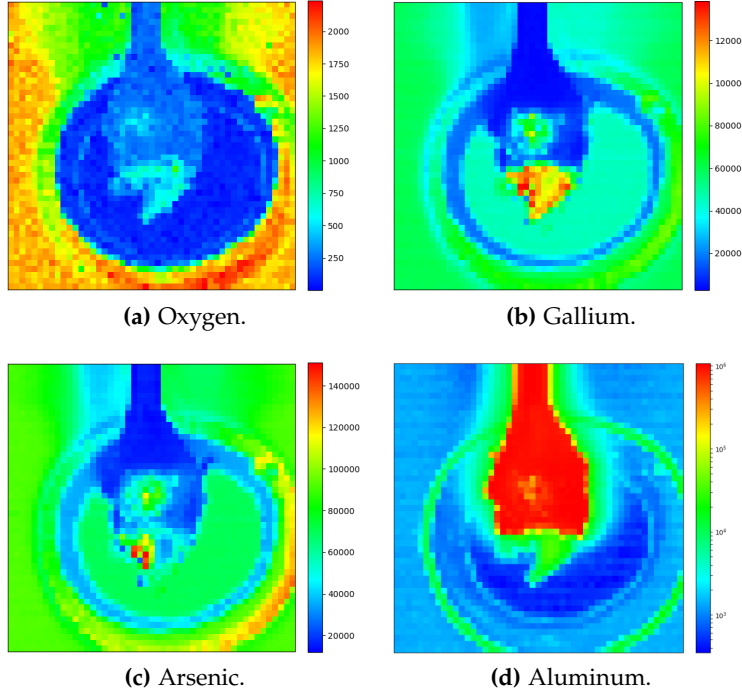


Figure 5.21: Fluorescence maps: distribution of particular materials across our device.

tion efficiencies in the area where the device collection is at its best. Figure 5.22 shows an example of photocurrent measured during a scan at an energy of 1500 eV: as expected the area with the highest collection is placed in the center of the mesa where there is no bonding and no alumina blocking the photons.

Now, calling N_0 the number of incoming photons, $N(x)$ the photons coming out after a thickness x of material, $T(x)$ the relative transmittance and λ the attenuation length, for the Beer-Lambert law it results that

$$N(x) = T(x)N_0 = N_0e^{-\frac{x}{\lambda}}, \quad (5.7)$$

thus, the absorbed photon density is

$$a(x) = -\frac{d}{dx}N(x) = \frac{N_0}{\lambda}e^{-\frac{x}{\lambda}}. \quad (5.8)$$

Figure 5.23 reports the distribution of absorbed photons in the case of a GaAs bulk.

Calling E_{ph} the energy of the photons (assumed to be much higher than the bandgap of GaAs) and ϵ the pair generation energy (for GaAs it can be approximated to 4.2 eV at room temperature), the density of the generated pairs is

$$n(x) = \frac{E_{ph}}{\epsilon}a(x) = \frac{E_{ph}}{\epsilon} \frac{N_0}{\lambda}e^{-\frac{x}{\lambda}} \quad (5.9)$$

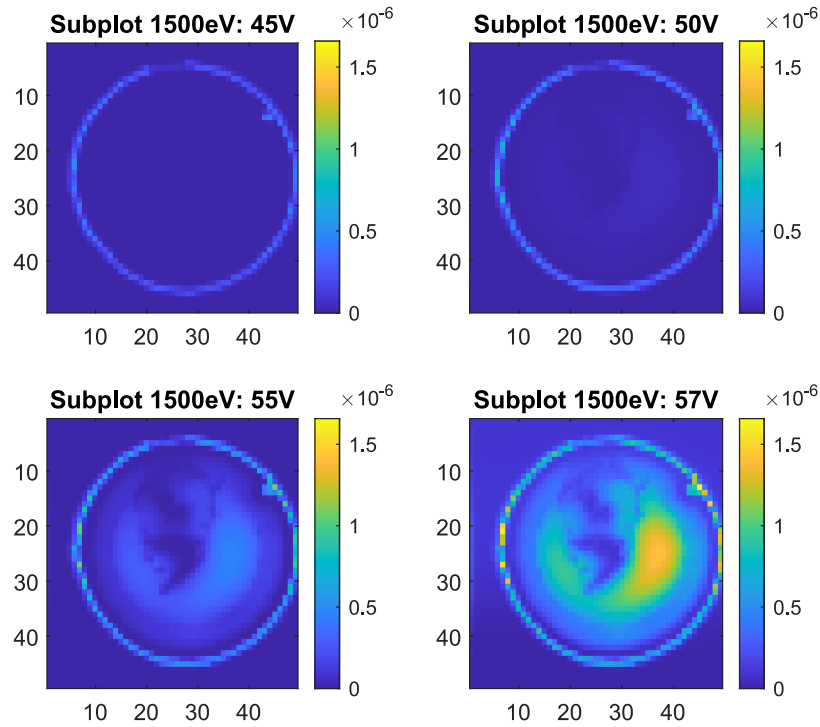


Figure 5.22: Current maps acquired at different biases with an energy beam of 1500 eV. The color scale represents the amount of measured current, where in yellow the highest values appear. On the xy axis the number of steps are shown.

which presents an exponential shape that is basically zero at the entrance of the multiplication region (meaning that the generation of electron-hole pairs happens mostly within the absorption region, meeting the ideal injection condition).

However, in our case it must be considered that incoming photons have to pass through 50 nm of gold and 10 nm of chromium before reaching the absorption region. Thus the transmissions are lowered by a certain factor which can be calculated again by using the Beer-Lambert law. Specifically, during the planned experiment two photon energies were used, 1500 eV and 1750 eV, with different penetration depths.

To calculate the absorption efficiency the mean value of the signal over the area where it was maximum (e.g. see Fig. 5.22), removing the dark current component, was calculated and processed considering the flux of incoming photons, the energy of such photons, the pair generation energy and the different absorption coefficients which can be found at different energies. The result was that with the higher energy the collection efficiency improves from 4% to 16%. This shows how the absorption region plays a fundamental role in the collection efficiency; in fact, the closer to the multiplication region the charge is generated the higher the efficiency is, probably owing to recombination issues in such region: thus, a lower recombination may improve the

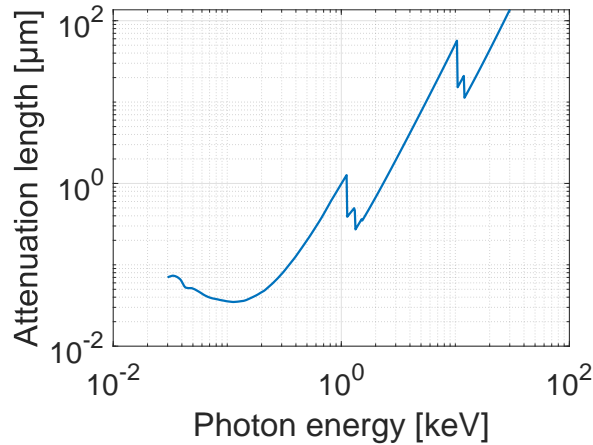


Figure 5.23: Attenuation length as a function of the photon energy for a GaAs bulk.

signal to noise ratio, both by reducing the noise and by increasing the signal. This experiment was designed to study the impact of the absorption region in the collection efficiency of the device. In fact, in the literature it is suggested that a relevant effect of trapping of electrons and holes in GaAs could happen [67].

BEAR Some other measurements were performed at the soft X-ray beamline BEAR. In particular, some 12-step devices (type **E**) were characterized. Figure 5.24a reports the photocurrent for different energies

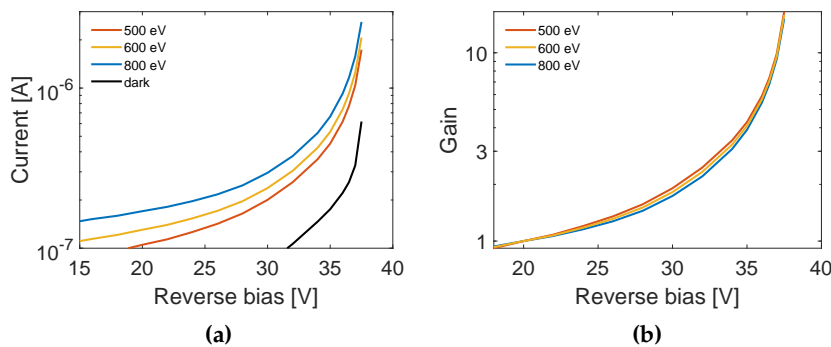


Figure 5.24: Dark current and photocurrent for three photon energies of the BEAR beamline in the 500-800 eV range of an **E**-type device (left); corresponding gains for the same photon energies (right).

of the beam and the dark current of such devices. The plot shows that in the experiments with higher photon energy, the photocurrent is larger. Figure 5.24b reports instead the gains calculated from the data plotted in the left part: gains for different photon energies are overlapping. This is reasonable since all the photogenerated carriers are created in the absorption region, as mentioned above, and subse-

quently multiplied in the multiplication region in the same way. This behavior occurred also for lower energies, as the ones provided by the lasers.

5.4.2 Hard X-rays

XRD2 To assess the response to photons of high energy, the devices were tested under irradiation with hard X-rays generated by the XRD2 wiggler beamline at Elettra Sincrotrone Trieste [52] (12.4 keV and $1.7 \cdot 10^{13} \text{ ph} \cdot \text{s}^{-1}$ over an area of $300 \times 90 \mu\text{m}^2$). The beamline and the set up are thoroughly described in sections 4.1.1.1 and 4.2.2.2.

During this experiment the employed devices were of the E-type, however, they were characterized by a larger area of the mesa. The diameter of such devices was $600 \mu\text{m}$. A bigger area was handy as the spot provided from the beamline could not be made much smaller without altering too much the incoming beam. Differently from the experiments with low energy, when working with 12.4 keV photons a certain amount of photons will reach the multiplication region, thus, the ideal condition of charge injection is not reached in this case and the overall generated noise will be higher.

To test the devices under illumination they were mounted on a dedicated circuit board and accommodated in the UHV-compatible chamber, which was placed downstream in the focal plane of the XRD2 line, where the photocurrents generated in the devices were measured utilizing the AH501 4.2.1.

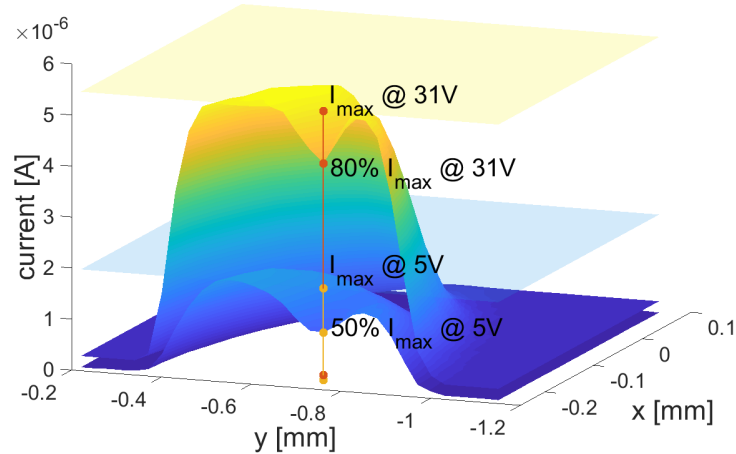


Figure 5.25: Current maps at 5 V (surface below) and 31 V (surface above) for the device with a mesa diameter of $600 \mu\text{m}$. The currents outside the mesa are due to the sum of the dark current with a residual response of the die caused by tails of the beam.

Owing to the movement stage it was possible to perform remotely controlled spatial mesh scans of the devices through the beam with a spot of approximately $100 \times 100 \mu\text{m}^2$ and a typical photon flux in the order of $10^{12} \text{ph} \cdot \text{s}^{-1}$. Various mesh scans were performed in order to evaluate the homogeneity of the generated photocurrent over the entire surface of the device. The scans were acquired with a step of $30 \mu\text{m}$. In particular, some current maps were acquired using different bias voltages. Figure 5.25 shows such maps specifically. The one measured at 5 V (surface below) shows how the charge collection is low in the center of the mesa with respect to its edge: the lowest value is 50% of the maximum value and the transition is quite smooth, meaning that the electric field established under this bias in the central part of the mesa is not high enough to drive the electrons created in that part down to the multiplication region before they recombine. Applying 31 V (avalanche region) the photocurrent surface appears flatter and more uniform, and the lowest value acquired is 80% of the maximum value, which shows that under this bias the field is already able (because of both its higher absolute values and its increased uniformity) to drive a large part of the electrons created in the center of the mesa down to the multiplication region. The overall lower current in the central part of the mesa with respect to the edge is due to the higher absorption of the gold contact.

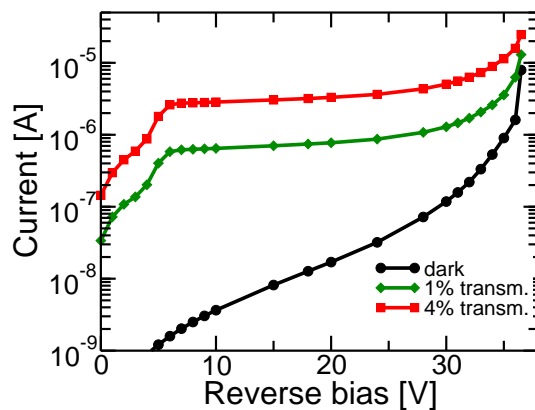


Figure 5.26: Measurements performed in air with a hard X-ray beam: black circles, the dark current; green diamonds, 1% of the transmitted beam through an Al filter; red squares, transmission 4%.

Furthermore, such photocurrent maps were used to align the center of the device under test with the incident radiation to record position invariant IV measurements and to perform time measurements. Figure 5.26 reports the IV curves for both dark current and responses to different photon fluxes, which were adjusted at different values by means of Al absorbers. In order to avoid radiation damage to the device the power provided by this synchrotron beamline was kept

at least an order of magnitude below the ones emitted by the laser source. In any case for both sources we observed the same expected behavior showing an increase in current with the increase of incident power.

Such IV curves under illumination follow quantitatively the expected progression of a SAM APD: recombination ($V_{bias} < 4V$), unity gain ($4V < V_{bias} < 7V$), punch through ($V_{bias} \approx 7V$), where all charges generated in the absorption region are transferred into the multiplication region, then the avalanche region ($7V < V_{bias} < 38V$) and eventually breakdown ($V_{bias} > 38V$), above which the device can operate in Geiger mode.

Moreover, during these measurements at 12.4 keV the radiation hardness was tested. In fact, the DUTs were exposed to a 6 mW flux for approximately 10 hours and further measurements showed that they do not exhibit any perceivable damage or variation in the performances.

Some preliminary timing measurements were performed by taking advantage of the bunch structure of Elettra. Although part of the experimental setup could not be optimized for precise timing measurements, the acquired data allowed us to see that our devices are fast enough to see Elettra's bunch structure. Unfortunately, quantitative metrics for the APD response could not be extracted from the acquisition owing to the significant spectral limitation introduced by some elements of the setup (e.g. cable loss, device capacitance in combination with the characteristic impedance, etc.).

During these measurements, the synchrotron facility was operating in its normal filling mode, providing 432 equidistant bunches per revolution (each bunch is characterized by a length of approximately 150 ps and a pitch between two adjacent bunches is 2 ns) and including a dark gap (interval of unfilled bunches), which was used as trigger for the oscilloscope.

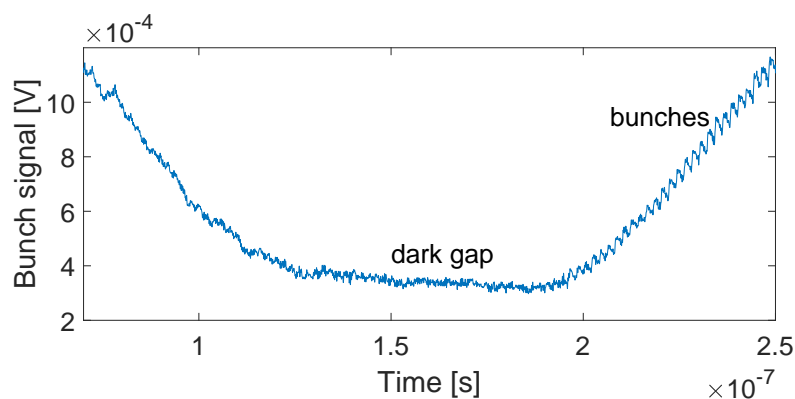
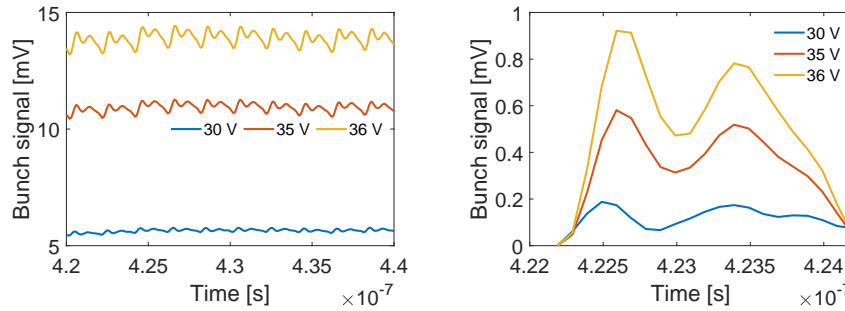


Figure 5.27: Dark gap detail of a time trace acquired at the XRD2 beamline by the oscilloscope.

Due to the limitations already mentioned, it can be seen that after the dark gap the single bunches create a pileup in the waveform (Fig. 5.27), as the device's response to the single bunch is convoluted with the much slower response of the limiting part of the setup. For this reason a waveform in which after each bunch the signal returns to 0 is not obtained and instead the pileup effect can be noted.



(a) A series of measured bunches after the dark gap. (b) Detail of a single bunch in comparison, where the offsets were removed.

Figure 5.28: Time traces acquired at the XRD2 beamline by the oscilloscope for different bias voltages.

However, looking at the curves acquired by the oscilloscope for different biases (Fig. 5.28a), it is still possible to appreciate a periodic undulation, which represents the response to each bunch superimposed to all the neighboring ones. Figure 5.28b shows a detail of such traces where the offsets were removed: it can be seen that as the bias increases the signals show the intrinsic gain of the structure.

MUCLS One device characterized by 24 steps was also measured at the compact synchrotron source located in Munich (section 4.1.3). Since the detectors do not possess a very good collection efficiency yet and still present some recombination issues of unknown causes (some reasons will be hypothesized in the next section), we chose the device with the highest gain amongst the devices categorized by a different number of steps.

These measurements were performed with hard X-rays characterized by a photon energy of 15 keV and a flux of 10^7 ph/s. The device allocated in the CUBE board was connected to an RF amplifier and through a cable of 5 m and an RC filter connected to the input of an oscilloscope.

From the acquired traces it was possible to notice that for low biases photons were hardly visible; however, there was a change in the offsets between dark and light data. The data set was processed and since it took some time for the oscilloscope to write the trace into memory and the offset changed in the meantime, some adjustment was made for each trace. A median filter was applied to remove the

remaining discontinuities. Histograms for the light and the dark data for each bias voltage were taken and from the Gaussian fits the mean values and the standard deviation were extracted. These are reported in Fig. 5.29. The gain is lower with respect to the one measured in other situations using the CUBE (e.g. with the laser): this could have happened as only 15% of the hard X-ray photon are actually absorbed within the device (the rest passes through it) and also because the low photon flux combined with the low collection efficiency did not trigger a larger response that could be seen by the oscilloscope. Qualitatively both gain and noise increase as the bias increases.

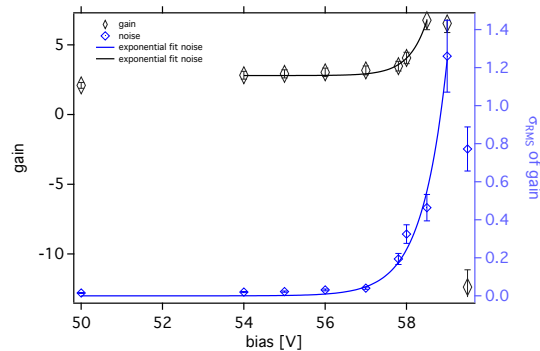


Figure 5.29: Gain and noise as a function of the bias for a device with 24 steps under a 15-keV beam provided by the MuCLS.

5.5 AMERICIUM MEASUREMENTS

A series of measurements performed with an ^{241}Am radioactive source at the INFN-Trieste was performed. The source was described in section 4.1.4 and the used setup in section 4.2.2.3: this source was chosen in order to release at once a large amount of charge almost entirely in the absorption region of our device; in fact, during the decay of this Am isotope a particle with an energy of 5.4 MeV and a photon of 59 keV are emitted. The former one was exploited for this kind of spectroscopic characterization.

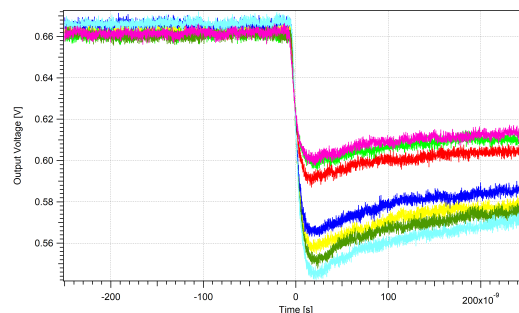


Figure 5.30: Examples of some signals generated by an americium alpha particle impinging on a 12-step detector, biased at 40 V.

Figure 5.30 shows some signals acquired during these tests. The background noise, which is mainly due to the electronics, is drastically reduced with respect to the one measured with the laser. This happened thanks to some adjustments, which were made on the bias board and the reduced decoupling capacity used. However, a higher variability of the curves with respect to the ones obtained with the preliminary laser measurements was registered, probably owing to the parallax effect, which also happens in air. Thus the particles with angles other than 90 degree with respect to the surface of the device are losing more energy in the air (since the path is longer) and have subsequently less energy when impinging on the detector. In fact, a particle releases its energy gradually interacting with the detector; therefore, the energy is deposited in a much more widespread area than what happens for a single photon, in some cases also creating pairs in the multiplication zone itself. Fortunately, increasing the distance of the source from the detectors ensures that the entire generation of electron-hole pairs occurs in the absorption region only as the ideal injection suggests. Nevertheless, given the aforementioned lack of collimation, particles entering the device with different angles of incidence deposit rather different amounts of charge.

Since the energy of the particles is very high, it was possible to use the events themselves as a trigger for the acquisitions. Each measurement consisted in the collection of 1000 traces (as the one showed in Fig. 5.30), from which the value of the step was calculated. Such acquisition took a considerable amount of time as there was an average counting rate of one event every 2 seconds; thus, to acquire a sequence of 1000 events approximately 30 minutes were required.

To verify the performances of the detectors a more delicate data analysis was necessary owing to the random nature of the events (e.g. the events could also occur near the reset and have a high variability of the incident angle). The results obtained are summarized in

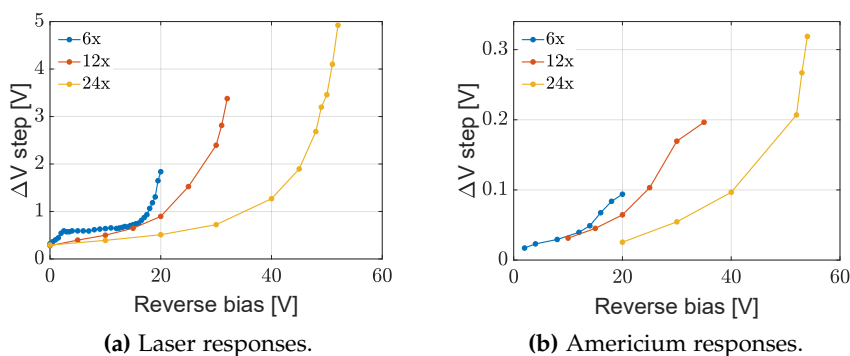


Figure 5.31: Mean value trend of the the step as a function of the bias for devices characterized by 6, 12 and 24 steps: on the left the responses obtained by using a laser with a power of $60 \mu\text{W}$, on the right the responses obtained by using the ^{241}Am radioactive source.

Fig. 5.31b: it is possible to observe a certain similarity in the trend with those of Fig. 5.31a acquired with the laser, instead. Even in the alpha particles case, although with less precision owing to the much more complicated type of matter interaction, a loss of signal (between 90% and 95%) with respect to what was expected occurred. Several hypothesis could explain such behavior: one considers the possibility that the surfaces where the electrodes had been deposited was not perfectly cleaned and could present defects in the band structure leading to recombination; another considers the possibility that the residual field in the absorption layer was not sufficiently high to grant the charges not to recombine in such area; and the last considered that the potential barrier introduced by the δ separation layer was too high and thus difficult to overcome for the electrons travelling towards the multiplication region.

5.6 DIELECTRIC LAYER

Some observations upon the dielectric layer were already carried out in section 3.3.2. Here a simple scan of one of the first samples developed, characterized by 12 steps (E-type) a mesa diameter of $800\ \mu\text{m}$ and a dielectric layer of silicon oxide acquired with a simple green table-top laser is reported. Figure 5.32 shows how the signal absorbed laterally in the device is higher due to the higher transmission in this region for photons of that energy. The scan shows two peaks, as the beam passing through the silicon oxide. In fact, it can be calculated that the transmission of photons (at $2.33\ \text{eV}$ or otherwise $\lambda = 532\ \text{nm}$) results in being 3.5% and 67.5% for the Au ($50\ \text{nm}$)/Cr ($10\ \text{nm}$) layer and for the $150\ \text{nm}\ \text{SiO}_2$ layer, respectively. A similar behavior can be noticed also in the case of the alumina.

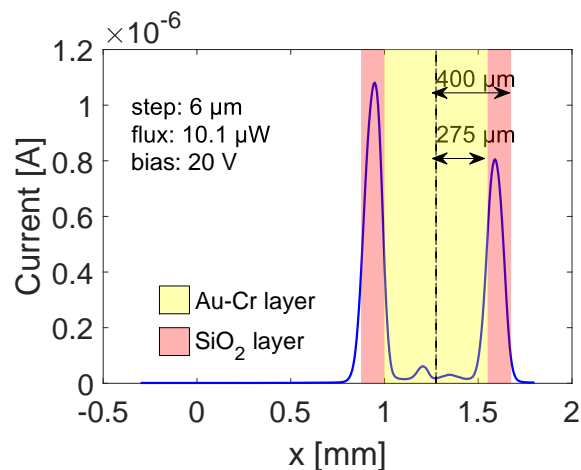


Figure 5.32: Horizontal scan revealing the overlap of metal electrodes and silicon oxide: the metal is placed in the yellow area and the silicon oxide lies in the red area.

CONCLUSIONS

The activity carried on over the past three years is part of a larger project for the development of X-ray detectors based on III-V semiconductors. Such activity is framed in a PRIN, a project of national interest, whose ultimate goal is the development of fast and sensitive avalanche photodiodes with low multiplication noise in order to fill the widening incompatibility between the requirements of next-generation light sources, which develop high energetic, high brilliance radiation and the relatively modest ability of available detectors to record the results of associated experiments.

This has led to the research of new materials: GaAs/AlGaAs heterojunctions based APD were chosen.

During these three years several devices have been grown and have been fabricated. A new history dependent model able to simulate impact ionization inside these devices was developed and it was used to optimize them. Benchmark setups were developed to test them and to compare them with simulation.

Some features, which affected the detector were tuned. The influence of the p-doped layer, which separates the absorption and multiplication region was investigated. Six different samples were fabricated in the form of p-doped δ sheets or layers of 50 nm. This difference was introduced because above a certain value, high acceptor concentrations were not achievable due to compensation of the GaAs:C layer.

Several tests were carried out: firstly, dark characteristics were acquired from which it was possible to notice that only above a certain concentration the multiplication process could be achieved. For devices with a low doping level a drop in capacitance occurred within the measured range at a voltage, which was found to decrease, decreasing the doping level. Such behavior was also confirmed by the CAD simulations, which were able to reproduce the measured CV curves for doping densities very close to the experimental ones. Moreover, the analysis of the simulated potential profiles confirmed the interpretation indicating the device with the planar doping concentration of $2.5 \cdot 10^{12} \text{ cm}^{-2}$ as the most suited for applications as radiation detector.

The response to light of the developed devices was measured by utilizing light sources characterized by having low energies; that ensured electron-hole pairs generation entirely within the absorption region, achieving the ideal injection condition. It was noticed that for low doping levels (lower than $2.5 \cdot 10^{12} \text{ cm}^{-2}$) the multiplication process did not take place, while a gain was experienced by devices

with a doping level equal to or above the one just mentioned. The absence of gain for lower doping is probably due to the fact that no field is established in the staircase region and thus no electrons are multiplied.

This field seems to be beneficial for the collection efficiency of the devices, as shown by comparing the absolute values of the photocurrent, while it does not influence significantly the multiplication process. Moreover, a higher concentration of dopant in the p-doped separation layer could result in an obstacle for the electrons, which are then less likely to reach the multiplication region.

After finding the optimal p-doping concentration in the separation layer, the influence of the number of steps in the multiplication region was investigated. Samples characterized by 6, 12 and 24 steps were fabricated. The simulations suggested that increasing the number of steps leads to a lower-noise detector. This was confirmed by the experiments, which were carried out: such devices, in fact, were tested from the point of view of the noise, of the timing and of the spectroscopic response. The gains extracted from these different experiments and under different light sources were compared. Qualitatively, in all the three cases, as predicted by simulations, the maximum gains rose increasing the number of steps. The rise time, instead, decreased increasing such number: thus, devices with 24 steps proved to be the fastest. However, the value is limited by the utilized instrumentation.

Various X-ray responses (from soft to hard X-rays) were analyzed. The Elettra synchrotron's beamlines at Trieste were used for this purpose. At the BEAR beamline the efficacy of the δ layer was tested, helping in finding the optimal concentration. At TwinMic the influence of the absorption region was investigated. It was noticed that such region plays a fundamental role in the low collection efficiency, probably owing to recombination processes. In fact, the closer the generation process gets to the multiplication region the better collection we obtain.

As the devices are intended for hard X-rays, some experiments were carried out with that kind of radiation. At XRD2 the devices were tested with a 12.4 keV beam. Radiation hardness was proved, and the trend expected for an APD was followed by the IV curves. At such beamline also some preliminary timing measurements were performed, which showed that our devices are fast enough to see the Elettra's bunches. As high energy source, also the MuCLS, the compact synchrotron light source of Munich, was used. However, in such case the low photon flux rendered the results hard to be interpreted, also owing to an intrinsic problem of recombination occurring inside the devices.

Finally, to test and verify the spectroscopic performances of the detector both a laser and an americium source were employed. Such experiments confirmed what was seen with the other characterization

techniques, both in terms of the trend of the gains and also regarding the recombination issue which eliminates lots of charge.

There are still lots of aspects which can be further investigated with such devices. To cite some of them, which could be performed in the near future as devices with suitable characteristics have been already fabricated: we could carry out a deeper analysis of the recombination and its dependence on the thickness of the absorption region and, the analysis of the devices with an higher step in the multiplication region, obtained by introducing the InGaAs alloy.

Part I

APPENDIX

FORMULA VALIDATION

A.1 LOCAL MODEL

A.1.1 Derivation of equation 2.2

Let us consider the avalanche process in a region of length W where photogeneration does not occur. In this case, the avalanche process may be generated from hole injection in $x = W$ or electron injection in $x = 0$. Let us assume to be in a DC stationary condition, in which avalanche generation is triggered in the depletion region W , characterized by the electric field E , by the injection of a hole current in $x = W$ and an electron in $x = 0$ [11]. From the continuity equation, and neglecting all generation and recombination phenomena apart from the avalanche multiplication, it results

$$\frac{dJ_n}{dx} = \alpha J_n + \beta J_p = -\frac{dJ_p}{dx} \quad (\text{A.1})$$

whose terms are mainly linked to drift currents if high electric fields are considered. Taking into account that the current density $J = J_n(x) + J_p(x)$ is constant, just one single equation can be obtained (e.g. electron current density) knowing the boundary conditions ($J_n(0)$ and $J_p(W)$) and it is possible to solve the linear differential equation of the first order (remark 2.1)

$$\frac{dJ_n}{dx} = (\alpha - \beta)J_n + \beta J \quad (\text{A.2})$$

whose general solution is

$$J_n(x) = e^{\int_0^x (\alpha - \beta) dx'} \left[J_n(0) + \int_0^x \beta J e^{-\int_0^{x'} (\alpha - \beta) dx''} dx' \right] \quad (\text{A.3})$$

thus the total current density J is given by

$$\begin{aligned} J &= J_n(W) + J_p(W) \\ &= e^{\int_0^W (\alpha - \beta) dx'} \left[J_n(0) + \int_0^W \beta J e^{-\int_0^{x'} (\alpha - \beta) dx''} dx' \right] + J_p(W). \end{aligned} \quad (\text{A.4})$$

Solving with respect to J

$$\begin{aligned} J &= \frac{e^{\int_0^W (\alpha - \beta) dx''} J_n(0) + J_p(W)}{1 - \int_0^W \beta(x') e^{\int_0^{x'} (\alpha - \beta) dx''} dx'} \\ &= M(0)J_n(0) + M(W)J_p(W) \end{aligned} \quad (\text{A.5})$$

where $M(0)$ and $M(W)$ are the electrons and hole multiplication factors, respectively.

If we add the contribution of the photogeneration process then equation A.5 turns into

$$J = M(0)J_n(0) + M(W)J_p(W) + \int_0^W G_o(x)M(x) dx \quad (\text{A.6})$$

which is equation 2.2.

A.1.2 Derivation of equation 2.10

Let us consider the solution of equation 2.9

$$M(x) = M(W)e^{\int_x^W (\alpha-\beta) dx'} \quad (\text{A.7})$$

and let us substitute it in equation 2.7, obtaining

$$\begin{aligned} M(W)e^{\int_x^W (\alpha-\beta) dx'} = 1 + \int_0^x \beta M(W)e^{\int_{x'}^W (\alpha-\beta) dx''} dx' + \\ + \int_x^W \alpha M(W)e^{\int_{x'}^W (\alpha-\beta) dx''} dx' \end{aligned} \quad (\text{A.8})$$

from which it is possible to obtain $M(W)$ considering it in $x = W$. This can again be substituted in equation A.7, giving

$$M(x) = \frac{e^{\int_x^W (\alpha-\beta) dx'}}{1 - \int_0^W \beta(x')e^{\int_{x'}^W (\alpha-\beta) dx''} dx'} \quad (\text{A.9})$$

A.1.3 Equation 2.16

The procedure to extrapolate equation 2.16 from 2.15 involves the integration by parts of

$$Si = 2q \int_0^W \frac{dJ_n}{dx} M^2(x) dx \quad (\text{A.10})$$

whose solution is

$$Si = 2q \left[[J_n M^2(x)]_0^W - \int_0^W 2J_n M(x) \frac{dM}{dx} dx \right]. \quad (\text{A.11})$$

Remembering that $\frac{dM}{dx} = -(\alpha - \beta)M(x)$, and under the hypothesis of $J_n(0) = J_p(W) = 0$ (that results in $J = J_n(W)$) we can write:

$$\int_0^W \frac{dJ_n}{dx} M^2(x) dx = JM^2(W) + 2 \int_0^W (\alpha - \beta) M^2(x) dx \quad (\text{A.12})$$

Considering that $(\alpha - \beta)J_n = \frac{dJ_n}{dx} - \beta J - G_o$ (equation 2.4):

$$\begin{aligned} \int_0^W \frac{dJ_n}{dx} M^2(x) dx = 2J \int_0^W \beta M^2(x) dx + \\ + 2 \int_0^W G_o M^2(x) dx - JM^2(W) \end{aligned} \quad (\text{A.13})$$

Knowing that $M(x') = M(W)e^{\int_{x'}^W (\alpha-\beta) dx''}$ and using equation A.6 under the boundary conditions then

$$\begin{aligned}
Si &= 2q \left[2 \int_0^W G_o(x)M(x) dx \int_0^W \beta(x)M^2(x) dx + \right. \\
&\quad \left. + 2 \int_0^W G_o(x)M^2(x) dx - \int_0^W G_o(x)M(x) dx M^2(W) \right] \\
&= 2q \int_0^W G_o(x)M^2(x) \underbrace{\left[\frac{2 \int_0^W \beta(x')M^2(x') dx'}{M(x)} + 2 - \frac{M^2(W)}{M(x)} \right]}_{F(x)} dx
\end{aligned} \tag{A.14}$$

that by comparison with equation 2.15b gives the excess noise factor $F(x)$ of equation 2.16.

A.2 NON-LOCAL MODEL

A.2.1 History-dependent model with local coefficients

The gain and the excess noise factor obtained with the local model coincide with the ones obtained for the nonlocal model by using the local ionization coefficients ($\alpha(x|x') = \alpha(x')$ e $\beta(x|x') = \beta(x')$). In the next paragraphs what just stated will be shown.

Gain From equations 2.26 and 2.27 we know that

$$P_{se}(x|w) = \exp \left[- \int_x^w \alpha(x|x') dx' \right] \tag{A.15a}$$

$$P_{sh}(x|0) = \exp \left[- \int_0^x \beta(x|x') dx' \right] \tag{A.15b}$$

$$p_e(x|x') = \alpha(x|x') \exp \left[- \int_x^{x'} \alpha(x|x'') dx'' \right] \tag{A.15c}$$

$$p_h(x|x') = \beta(x|x') \exp \left[- \int_{x'}^x \beta(x|x'') dx'' \right] \tag{A.15d}$$

which must be inserted in equations 2.32 and 2.33 applying the local hypothesis $\alpha(x|x') = \alpha(x')$ and $\beta(x|x') = \beta(x')$; thus obtaining N_e and N_h (the dependence from x' has been overlooked for simplicity)

$$N_e = e^{-\int_x^W \alpha dx'} + \int_x^W (2N_e + N_h) \alpha e^{-\int_x^{x'} \alpha dx''} dx' \tag{A.16a}$$

$$N_h = e^{-\int_0^x \beta dx'} + \int_0^x (2N_h + N_e) \beta e^{-\int_{x'}^x \beta dx''} dx' \tag{A.16b}$$

Performing the derivative in x of A.16a as suggested by remark A.1

$$\begin{aligned}
\frac{dN_e}{dx} &= e^{-\int_x^W \alpha dx'} - \alpha(2N_e + N_h) + \alpha \int_x^W (2N_e + N_h) \alpha e^{-\int_x^{x'} \alpha dx''} dx' \\
&= -\alpha(N_e + N_h)
\end{aligned}$$

(A.17)

Analogously, from A.16b:

$$\begin{aligned}\frac{dN_h}{dx} &= -e^{-\int_0^x \beta dx'} - \beta(2N_h + N_e) - \beta \int_0^x (2N_h + N_e) \beta e^{-\int_{x'}^x \beta dx''} dx' \\ &= \beta(N_h + N_e).\end{aligned}$$

(A.18)

Remark A.1: $\frac{d}{dx} \int_x^W N \alpha e^{-\int_x^{x'} \alpha dx''} dx'$

To calculate the derivative of equations A.16 it is necessary to solve the derivative of the integral appearing in the equations. The proof of equation A.16a will be carried on as an example. Let imposing $N = 2N_e + N_h$. The derivative $\frac{d}{dx} \int_x^W N \alpha e^{-\int_x^{x'} \alpha dx''} dx'$ can be written as the limit of the incremental ratio:

$$\lim_{\Delta x \rightarrow 0} \frac{\int_{x+\Delta x}^W N \alpha e^{-\int_{x+\Delta x}^{x'} \alpha dx''} dx' - \int_x^W N \alpha e^{-\int_x^{x'} \alpha dx''} dx'}{\Delta x}$$

And considering that $\int_{x+\Delta x}^W = \int_x^W - \int_x^{x+\Delta x}$, using the fundamental theorem of calculus, the limit can be re-written as:

$$\begin{aligned}\lim_{\Delta x \rightarrow 0} \frac{\int_x^W N \alpha e^{-\int_x^{x'} \alpha dx''} dx' \left(e^{-\int_x^{x+\Delta x} \alpha dx'} - 1 \right) - N \alpha \Delta x}{\Delta x} = \\ \alpha(x) \int_x^W N(x') \alpha(x') e^{\int_x^{x'} \alpha(x'') dx''} dx' - N(x) \alpha(x)\end{aligned}$$

which is the result used to obtain equation A.17.

Knowing that $M = (N_e + N_h)/2$ thus

$$\frac{dM}{dx} = -(\alpha - \beta)M \quad (\text{A.19})$$

whose solution is

$$M(x) = M(W) e^{\int_x^W (\alpha - \beta) dx'}, \quad (\text{A.20})$$

it results that

$$\frac{dN_h}{dx} = \beta(N_h + N_e) = 2\beta M = 2\beta M(W) e^{\int_x^W (\alpha - \beta) dx'} \quad (\text{A.21})$$

Applying and solving the integral:

$$N_h(W) = N_h(0) + \int_0^W 2\beta M(W) e^{\int_{x'}^W (\alpha - \beta) dx''} dx'. \quad (\text{A.22})$$

Boundary conditions

$$N_e(W) = 1$$

$$N_h(0) = 1$$

Remembering the boundary conditions given by equation 2.34 we

can substitute equation A.22 in $M(W) = (N_e(W) + N_h(W))/2$ obtaining:

$$M(W) = \frac{1}{1 - \int_0^W 2\beta e^{\int_{x'}^W (\alpha-\beta) dx''} dx'} \quad (\text{A.23})$$

that combined with equation A.20 leads to

$$M(x) = \frac{e^{\int_x^W (\alpha-\beta) dx'}}{1 - \int_0^W \beta(x') e^{\int_{x'}^W (\alpha-\beta) dx''} dx'} \quad (\text{A.24})$$

that is equal to the expression used in the local model (equation 2.10).

Excess noise factor In the local model the excess noise factor is expressed by 2.16 hereinafter reported

$$F(x) = 2 + \left[2 \int_0^W \beta e^{2 \int_{x'}^W (\alpha-\beta) dx''} dx' - 1 \right] \frac{M(W)}{e^{\int_x^W (\alpha-\beta) dx'}} \quad (\text{A.25})$$

that can be re-arranged by using

$$F(W) = 2 + \left(2 \int_0^W \beta e^{2 \int_{x'}^W (\alpha-\beta) dx''} dx' - 1 \right) M(W) \quad (\text{A.26})$$

as

$$F(x) - 2 = (F(W) - 2) e^{-\int_x^W (\alpha-\beta) dx'} \quad (\text{A.27})$$

which is going to be used as the comparison term to verify that under the conditions $\alpha(x|x') = \alpha(x')$ and $\beta(x|x') = \beta(x')$ the local model and the nonlocal model, respectively, give the same results.

As pointed out in section 2.2.1 the excess noise factor can be expressed by using equations from 2.45 to 2.48:

$$\begin{aligned} N_e &= e^{-\int_x^W \alpha dx'} + \int_x^W (2N_e + N_h) \alpha e^{-\int_x^{x'} \alpha dx''} dx' \\ N_h &= e^{-\int_0^x \beta dx'} + \int_0^x (2N_h + N_e) \beta e^{-\int_x^{x'} \beta dx''} dx' \\ \overline{n_e^2} &= e^{-\int_x^W \alpha dx'} + \int_x^W (2\overline{n_e^2} + \overline{n_h^2} + 2N_e^2 + 4N_e N_h) \alpha e^{-\int_x^{x'} \alpha dx''} dx' \\ \overline{n_h^2} &= e^{-\int_0^x \beta dx'} + \int_0^x (2\overline{n_h^2} + \overline{n_e^2} + 2N_h^2 + 4N_e N_h) \beta e^{-\int_x^{x'} \beta dx''} dx' \end{aligned}$$

Deriving as remark A.1 suggests

$$\frac{dN_e}{dx} = -\alpha(N_e + N_h) \quad (\text{A.28a})$$

$$\frac{dN_h}{dx} = \beta(N_h + N_e) \quad (\text{A.28b})$$

$$\frac{d\overline{n_e^2}}{dx} = -\alpha(\overline{n_e^2} + \overline{n_h^2} + 2N_e^2 + 4N_e N_h) \quad (\text{A.28c})$$

$$\frac{d\overline{n_h^2}}{dx} = \beta(\overline{n_e^2} + \overline{n_h^2} + 2N_h^2 + 4N_e N_h) \quad (\text{A.28d})$$

Performing the derivative on equation 2.44

$$F(x) = \frac{\overline{n}_h^2 + \overline{n}_e^2 + 2N_e N_h}{4M^2(x)}$$

it will result that

$$\frac{dF}{dx} = \frac{1}{4M^2} \underbrace{\frac{d}{dx}(\overline{n}_e^2 + \overline{n}_h^2 + 2N_e N_h)}_a - \underbrace{\frac{1}{2M^3}(\overline{n}_e^2 + \overline{n}_h^2 + 2N_e N_h)}_b \underbrace{\frac{dM}{dx}}_c \quad (\text{A.29})$$

whose terms can be rearranged as:

$$\begin{aligned} a &= -(\alpha - \beta)(\overline{n}_e^2 + \overline{n}_h^2 + 2N_e^2 + 2N_h^2 + 6N_e N_h) \\ b &= \frac{2}{M} F \\ c &= -(\alpha - \beta)M \end{aligned}$$

Remembering

$$F = \frac{\overline{n}_e^2 + \overline{n}_h^2 + 2N_e N_h}{4M^2}$$

$$2(N_e + N_h)^2 = 8M^2$$

Then

$$\frac{d(F - 2)}{dx} = (\alpha - \beta)(F - 2) \quad (\text{A.30})$$

whose solution is

$$F(x) - 2 = [F(W) - 2]e^{-\int_x^W (\alpha - \beta) dx'} \quad (\text{A.31})$$

So equation A.31 coincides with equation A.27.

It is necessary to verify that the expression for $F(W)$ is the same of equation A.26, thus:

$$F(W) = \frac{\overline{n}_e^2(W) + \overline{n}_h^2(W) + 2N_e(W)N_h(W)}{4M^2(W)} \quad (\text{A.32})$$

and considering that $\overline{n}_e^2(W) = 1$, $\overline{n}_h^2(W) = 1$ and $M(W) = \frac{N_h(W)+1}{2}$, thus $N_h(W) = 2M(W) - 1$ one can write:

$$F(W) = \frac{\overline{n}_h^2(W) - 1}{4M^2(W)} + \frac{1}{M(W)} \quad (\text{A.33})$$

with the process explained in remark A.2 the following can be obtained

$$F(W) = 2 + M(W) \left[2 \int_0^W \beta e^{2 \int_{x'}^W (\alpha - \beta) dx''} dx' \right] \quad (\text{A.34})$$

which corresponds to A.26, proving that collapsing the dependence on x and x' on the sole dependence on x , the history dependent model tends to the local one.

Remark A.2

Since

$$\overline{n_h^2}(W) = \overline{n_h^2}(0) + \int_0^W \frac{d\overline{n_h^2}}{dx} dx$$

with $\overline{n_h^2}(0) = 1$, from eq. A.28d, by using equations A.26 and A.28b and considering $M^2 = M^2(W) \exp 2 \int_{x'}^W (\alpha - \beta) dx'$

$$\begin{aligned} \frac{d\overline{n_h^2}}{dx} &= \beta 4M^2(W) e^{2 \int_{x'}^W (\alpha - \beta) dx''} \\ &\cdot \left[2 + (F(W) - 2) e^{2 \int_{x'}^W (\alpha - \beta) dx''} \right] + 2N_h \frac{dN_h}{dx} \end{aligned}$$

whose solution is

$$\begin{aligned} \overline{n_h^2}(W) &= 1 + \\ &\int_0^W \beta 4M^2(W) e^{2 \int_{x'}^W (\alpha - \beta) dx''} \\ &\cdot \left(2 + (F(W) - 2) e^{2 \int_{x'}^W (\alpha - \beta) dx''} \right) dx' + 2 \underbrace{\int_1^{N_h(W)} N_h dN_h}_d. \end{aligned}$$

Given that

$$2d = N_h^2(W) - 1 = (2M(W) - 1)^2 - 1 = 4M^2(W) - 4M(W)$$

then

$$\begin{aligned} F(W) &= \frac{1}{4M^2(W)} \left[4M^2(W) - 4M(W) + \right. \\ &\quad \left. + \int_0^W \beta 4M^2(W) e^{2 \int_{x'}^W (\alpha - \beta) dx''} \right. \\ &\quad \left. \cdot \left(2 + (F(W) - 2) e^{-2 \int_{x'}^W (\alpha - \beta) dx''} \right) dx' \right] + \frac{1}{M(W)}. \end{aligned}$$

Remembering that $\int_0^W \beta e^{\int_{x'}^W (\alpha - \beta) dx''} dx' = 1 - \frac{1}{M(W)}$, through some steps, eq. A.34 can be obtained:

$$\begin{aligned} F(W) - F(W) \left(1 - \frac{1}{M(W)} \right) &= 2 \int_0^W \beta e^{2 \int_{x'}^W (\alpha - \beta) dx''} dx' \\ &\quad + 1 - 2 + \frac{2}{M(W)}. \end{aligned}$$

B.1 FABRICATION: A STEP-BY-STEP DESCRIPTION

The fabrication procedure is composed of different phases and processes that have been explained in Chapter 3. Hereinafter, a non formal explanation that can help in the work performed in the clean rooms of FNF at the IOM-CNR facility in Trieste will be presented.

Considering the available wafer either of two ways can be followed: if the employed wafer is a single-side-polished one Ga-bonded to the MBE substrate holder (Fig. B.1a), start from section B.1.1, otherwise, if it is the case of a double-side-polished wafer mounted with clips to a Ga-free MBE holder (Fig. B.1b), from section B.1.2.

If it is not otherwise stated, the processes and the following actions are to be considered performed at room temperature.

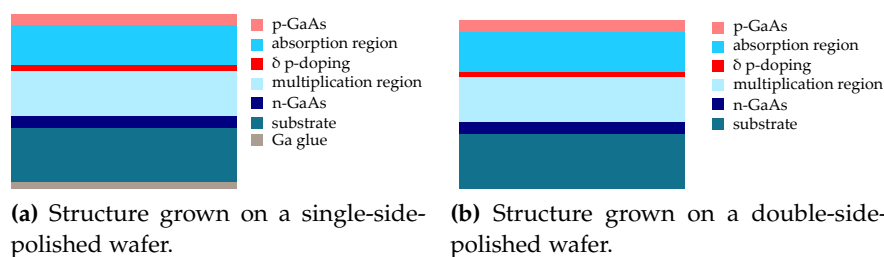


Figure B.1: Structures grown on wafers.

B.1.1 Back side cleaning & polishing

Once the single-side-polished wafer has been grown with MBE techniques, it is necessary to clean the back side of the sample (the one not polished) from the gallium (Ga) which is used as glue to hold the wafer onto the substrate holder in the MBE. In order to do so, the sample is positioned on the spin coater and its front side is covered with S1818 resist. This is dropped off on the sample and the procedure is launched with a rotation of 2500 rpm for one minute. Immediately afterwards the sample is baked at 115 °C on a hot plate for two minutes (Fig. B.2). This layer is quite thick (2.5 μm) and it is used just as protection layer.

Once the sample has cooled down, it is immersed in a solution (1:1) of water and HCl (37%). The sample needs to be positioned with its bottom side pointed upward in order to maximize the area to etch. Furthermore placing the sample in a watch glass disk allows the front

Before pouring the resist use the nitrogen gas (positioned near the spin coater) to clean the sample.

Add HCl to water; the process is very exothermic.

side to touch just the wafer edges, lowering the chances to damage the surface of the wafer.

It is recommended to use Teflon tweezers.

The sample can be removed from the HCl solution when there are not any more bubbles. If unsure about the completeness of the process, it is better to leave it longer in the HCl solution.

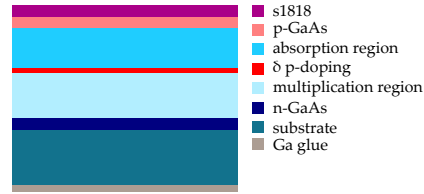


Figure B.2: Sample equipped with a protecting layer prior to removal of the Ga glue.

Still leaving the front side covered, the sample back surface is polished firstly with water on rough sand paper, then with diamond paste. Diamond paste grits are ranging from coarse to fine: the one used for the final polishing has a grit of 1 μm . The recipe is reported in Table B.1.

Before the next step (the mesa lithography process) it is necessary to remove the photoresist, which was put only to protect the sample. This is done with acetone.

The wafer has to be immersed in acetone, then rinsed with it, and afterwards with isopropanol, and dried

Rag	Material	Time	Frequency
sandpaper 1200 C	distilled water		by hand
sandpaper 2500 C	distilled water	until smooth and uniform surface	200 rpm
white nylon	diamond paste 6 μm	10-15 min	350 rpm
red	diamond paste 3 μm	15 min	300 rpm
red	diamond paste 1 μm	10 min	250-300 rpm
red	isopropanol		150 rpm

Table B.1: Polishing recipe.

B.1.2 Mesa lithography

Let us continue with the processing for the single-side-polished wafer or start the first step in the case of a double-polished one. The sample is placed on the spinner; however, this time the spin coating procedure

is characterized by a speed of 4000 rpm for one minute, resulting in a layer 2 μm thick (Fig. B.3a). Afterwards it is baked at 115 $^{\circ}\text{C}$ for one minute on a hot plate.

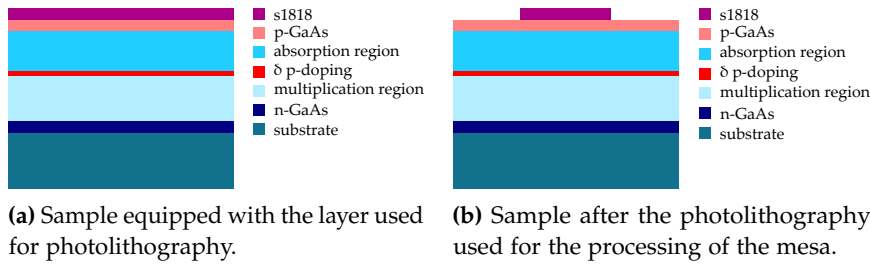


Figure B.3: Mesa lithography steps.

Then, the resist is exposed through a mask aligner (Karl Suss MJB3 Mask Aligner) for 15 s using a mask as in Figure B.4 (bigger dots on the right side). The S1818 resist is a positive photoresist, meaning that the material exposed with UV light is the one which is going to be removed. In these resists, exposure to the UV light changes the chemical structure of the resist so that it becomes more soluble in the developer.

Turn on the machine at least an hour before use in order to warm it up. It is necessary to turn on the nitrogen, the compression, and wait a little to turn on the vacuum.

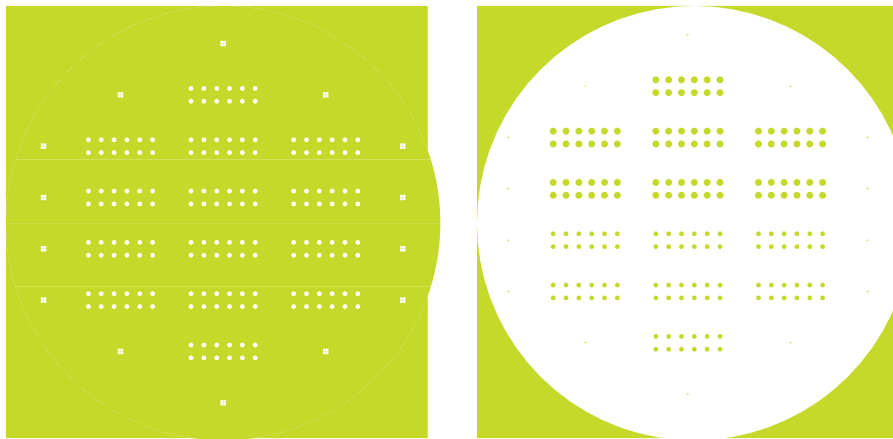


Figure B.4: Two masks. The mask on the left is the one for the opening used for the metalization of the p-contact (diameter 150 μm), while on the right the openings for the alumina layer (smaller dots, diameter length 150 μm) and for the mesa (bigger dots, diameter 200 μm) appear.

The exposed resist is then developed by MF-319 developer solution (developed for about a minute, check under the microscope to see if some residuals are still on the sample) and then rinsed in water and dried. The mask, therefore, contains an exact copy of the pattern, which remains on the wafer, as a stencil for subsequent processing. The result can be seen in Fig. B.3b.

B.1.3 Etching mesa

Before this process the back side of the sample has to be checked in order to make sure that no resist remains on it.

The etching process then begins with the preparation of the etching solution $\text{H}_3\text{PO}_4:\text{H}_2\text{O}_2:\text{H}_2\text{O}$ (3:1:50). The sample has to be submerged in it for a certain period of time taking into consideration that the etching rate is approximately 100 nm/min. However, it can differ significantly from case to case because the velocity depends from the concentration of the peroxide solution (H_2O_2), which is not stable and whose concentration in the bottle where it is stored decreases with time. Furthermore, temperature has to be considered as it plays a big role in the process. Therefore, it would be better to test each time the etching rate. Moreover, this action is necessary if working with PIN diodes, while, in the case of the staircase structure at a certain point while submerged a rainbow strip pattern will appear. This is due to the interference on the multilayer staircase structure and when it disappears again it means that the n-substrate has been reached and that the etching process is over.

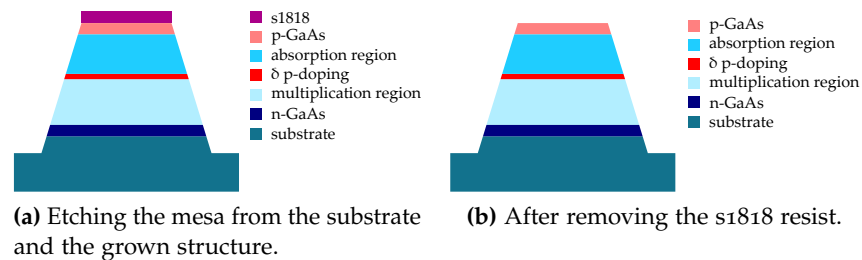


Figure B.5: Results of the etching of the mesa.

At the end of the process something as in Fig. B.5 can be observed, after rinsing the sample with water (Fig. B.5a) and with the removal of the resist (Fig. B.5b).

The height of the device depends on the structure which was grown through MBE. In the standard one described in Ch. 3 it is about 6 μm

B.1.4 Al_2O_3 layer

To reduce the leakage currents, coating the sample with a dielectric layer is necessary: the process is done with the evaporator. In this phase two resists are needed:

- lift of resist (LOR), which has to be spun at 2500 rpm and then baked at 180 °C in a closed hot plate for 5 min (thickness 3.5 μm)
- S1818 photoresist, which is spun at 4000 rpm and then baked at 115 °C (thickness 2 μm).

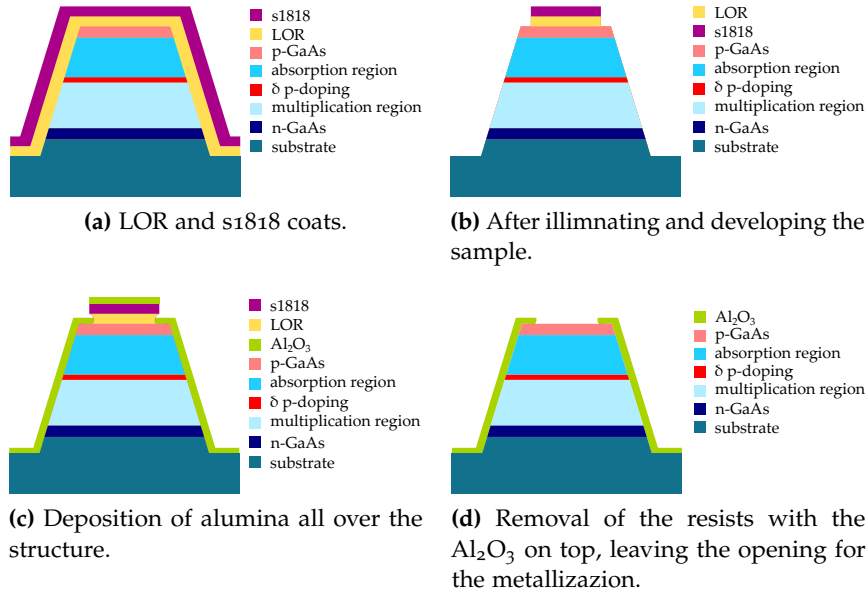


Figure B.6: Al_2O_3 deposition steps.

After the coating with these two resists (Fig. B.6a), the sample is exposed under the light and developed with the MF-319 developer (Figure B.6b). The utilized mask is characterized by small circles having a diameter of $150\ \mu\text{m}$ (Fig. B.4, small dots on the right-hand-side mask).

The evaporation process follows, and the result is a layer of Al_2O_3 (350 nm) all over the structure as in Fig. B.6c. The part above the resist is then removed by placing the wafer first in acetone and then in MF-319. This last procedure can be repeated once or twice if necessary. Figure B.6d shows the final structure.

B.1.5 P-contact metalization

This procedure is preceded by oxygen cleaning, which has to be done immediately after the Al_2O_3 deposition, either in RIE or in the sputtering machine. In the RIE the sample is positioned and the reactive ion etching process takes place. The used gases are O_2 , Ar and CF_4 in the ratio of 3:3:25. The procedure takes place for 2 min at 100 W and with a bias of 100 V.

Again as described in section B.1.4 the two resists, LOR and s1818, are deposited, exposed under the light and developed with the MF-319 developer using the mask appearing on the left side of Fig. B.4 (with opening diameter $150\ \mu\text{m}$) resulting in Fig. B.7a.

Then the metalization process can start. The metalization of the p-contact, which is carried on in the evaporator, consists in the deposition of a layer of 10 nm of Cr followed by 50 nm of Au (the chromium is used for better adhesion). The device then appears as in Figure B.7b.

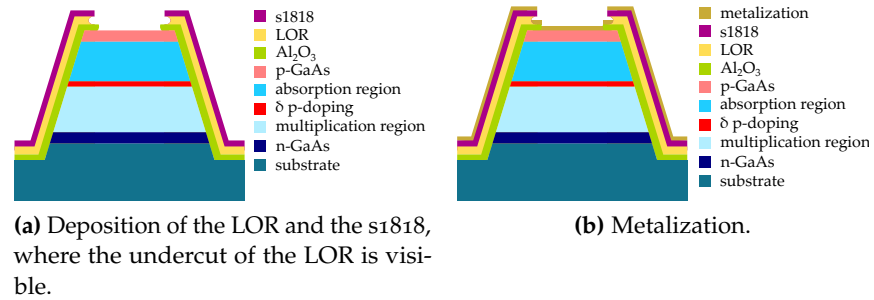


Figure B.7: P-contact metalization.

B.1.6 N-contact metalization

The n-contact metalization does not need to be performed with a mask because it is done on the whole back-plane of the sample. The two resists and the metallic layer are left on the sample in order to protect the front side during the process. The multilayer is composed of GeAu/Ni/Au with a thickness in nanometers of 40/10/50, respectively. Figure B.8 shows the device after this procedure.

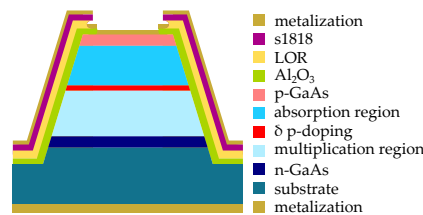


Figure B.8: Bottom n-metalization.

B.1.7 Final structure

The two resists are then removed by submerging the device in acetone for a couple of minutes and then in MF-319. Again this process can be repeated if necessary. This last step allows the metal in excess to be removed from the whole wafer, leaving just the p-contact. The final structure looks like in Figure B.9.

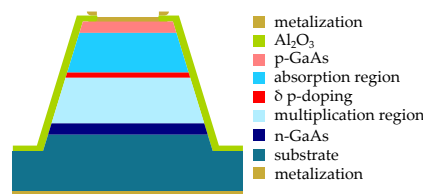


Figure B.9: Final structure.

BIBLIOGRAPHY

- [1] R.J. McIntyre. "A new look at impact ionization - Part I: A theory of gain, noise, breakdown probability, and frequency response." In: *IEEE Trans. Electron Devices* 46.8 (Aug. 1999), pp. 1623 –1631. DOI: [10.1109/16.777150](https://doi.org/10.1109/16.777150).
- [2] M.C. Teich, K. Matuso, and B.E.A Saleh. "A New Look at Impact Ionization - Part II: Gain and Noise in Short Avalanche Photodiodes." In: *IEEE Trans. Electron Devices* 46.8 (Aug. 1999), pp. 1632 –1639. DOI: [10.1109/16.777151](https://doi.org/10.1109/16.777151).
- [3] J.H. Hubbell. "Photon mass attenuation and energy-absorption coefficients." In: *Int. J. Appl. Radiat. Isot.* 33.11 (Nov. 1982), pp. 1269 –1290. DOI: [doi.org/10.1016/0020-708X\(82\)90248-4](https://doi.org/10.1016/0020-708X(82)90248-4).
- [4] J. Lauter, A. Forster, H. Luth, K.D. Muller, and R. Reinartz. "AlGaAs/GaAs avalanche detector array-1 GBit/s X-ray receiver for timing measurements." In: *IEEE Trans. Nucl. Sci.* 43 (June 1996), pp. 1446 –1451. DOI: [10.1109/23.507080](https://doi.org/10.1109/23.507080).
- [5] F. Capasso. "Staircase Solid-State Photomultipliers and Avalanche Photodiodes with Enhanced Ionization Rates Ratio." In: *IEEE Trans. Electron Devices* ED-30 (Apr. 1983), pp. 381 –390. DOI: [10.1109/tns.1983.4332303](https://doi.org/10.1109/tns.1983.4332303).
- [6] R.J. McIntyre. "Multiplication noise in uniform avalanche diodes." In: *IEEE Trans. Electron Devices* ED-13.1 (1966), pp. 164–168. DOI: [10.1109/T-ED.1966.15651](https://doi.org/10.1109/T-ED.1966.15651).
- [7] B.E.A. Saleh and M.C. Teich. *Fundamentals of photonics*. John Wiley & Sons, 2019.
- [8] P. Russo and R.H. Menk. *Handbook of X-ray Imaging*. CRC Press, 2017. Chap. 1.
- [9] S.M. Sze and K.K. Ng. *Physic of Semiconductor Devices*. John Wiley & Sons, 2007.
- [10] D.A. Neamen. *Semiconductor Physics and Devices - Basic Principles, Fourth Edition*. McGraw-Hill, 2012.
- [11] G. Ghione. *Semiconductor Devices for High-Speed Optoelectronics*. Cambridge University Press, 2009.
- [12] W. Frensley and N. Einspruch. *Heterostructures and Quantum Devices*. Vol. 24. Academic Press, 1994. Chap. 1.
- [13] F. Capasso. "Enhancement of electron impact ionization in a superlattice: A new avalanche photodiode with a large ionization rate ratio." In: *Appl. Phys. Lett* 40 (Jan. 1982), pp. 38 –40. DOI: [10.1063/1.92910](https://doi.org/10.1063/1.92910).

- [14] W.T. Tsang, ed. *Semiconductors and Semimetals*. Vol. 22. Part D. Academic Press Inc., 1985, pp. 1–172.
- [15] M.C. Teich, K. Matuso, and B.E.A Saleh. “Excess Noise Factor for Conventional and Superlattice Avalanche Photodiodes and Photomultiplier Tubes.” In: *IEEE J. Quantum Electron.* QE-22 (Aug. 1986), pp. 1184–1193. DOI: [10.1109/JQE.1986.1073137](https://doi.org/10.1109/JQE.1986.1073137).
- [16] G. Bertuccio and D. Maiocchi. “Electron-hole pair generation energy in gallium arsenide by x and γ photons.” In: *J. Appl. Phys.* 92 (2002), pp. 1248–1255. DOI: [10.1063/1.1490158](https://doi.org/10.1063/1.1490158).
- [17] G. Lutz. *Semiconductor Radiation Detectors*. Springer, 2007.
- [18] G. Lioliou, X. Meng, J.S. Ng, and A.M. Barnett. “Temperature dependent characterization of gallium arsenide X-ray mesa p-i-n photodiodes.” In: *J. Appl. Phys.* 119.124507 (2016). DOI: [10.1063/1.4944892](https://doi.org/10.1063/1.4944892).
- [19] M. Levinshtein, M. Rumyantsev, and M.S. Shur. *Handbook series on Semiconductor Parameters*. Vol. 1. World Scientific Publishing, 1996.
- [20] R.H. Bube. *Photoelectronic properties of semiconductors*. Cambridge University Press, 1992.
- [21] A. Van der Ziel. *Noise in solid state devices and circuits*. John Wiley & Sons, 1986.
- [22] C. Nichetti et al. “An Improved Nonlocal History-Dependent Model for Gain and Noise in Avalanche Photodiodes Based on Energy Balance Equation.” In: *IEEE Trans. Electron Devices* 65.5 (2018). DOI: [10.1109/TEDE.2018.2817509](https://doi.org/10.1109/TEDE.2018.2817509).
- [23] S. Selberherr. *Analysis and Simulation of Semiconductor Devices*. McGraw-Hill, 1995.
- [24] W.L. Hayat M.M. and Sargeant and B.E.A Saleh. “Effect of Dead Space on Gain and Noise in Si and GaAs Avalanche Photodiodes.” In: *IEEE J. Quantum Electron.* 28.5 (1992), pp. 1360–1365. DOI: [10.1109/3.135278](https://doi.org/10.1109/3.135278).
- [25] G.M. Williams, M. Compton, D. Ramirez, M.M. Hayat, and A. Huntington. “Multi-Gain-Stage InGaAs Avalanche Photodiode With Enhanced Gain and Reduced Excess Noise.” In: *IEEE Electron Devices Soc.* 1 (Feb. 2013), pp. 54–65. DOI: [10.1109/JEDS.2013.2258072](https://doi.org/10.1109/JEDS.2013.2258072).
- [26] P. Palestri, L. Selmi, G.A.M. Hurkx, J.W. Slotboom, and E. Sangiorgi. “Energy dependent electron and hole impact ionization in Si bipolar transistors.” In: *IEDM Tech. Dig.* (Dec. 1998), pp. 885–888. DOI: [10.1109/IEDM.1998.746496](https://doi.org/10.1109/IEDM.1998.746496).

- [27] J.W. Slotboom, G. Streutker, M.J.V. Dort, Woerlee P.H., A. Pruijmboom, and D.J. Gravesteijn. "Non-local impact ionization in silicon devices." In: *IEDM Tech. Dig.* (Dec. 1991), pp. 127–130. DOI: [10.1109/IEDM.1991.235484](https://doi.org/10.1109/IEDM.1991.235484).
- [28] *Sentaurus Device User Guide*. English. Version L-2016.03. Synopsys. Mountain View, CA, USA, 2016.
- [29] B.K. Ng, J.P.R. David, S.A. Plimmer, G.J. Rees, R.C. Tozer, M. Hopkinson, and G. Hill. "Avalanche multiplication characteristics of $\text{Al}_{0.8}\text{Ga}_{0.2}\text{As}$ diodes." In: *IEEE Electr. Devices Lett.* 48 (Oct. 2001), pp. 2198–2204. DOI: [10.1109/16.954454](https://doi.org/10.1109/16.954454).
- [30] B.K. Ng, R.C. David J.P.R. and Tozer, M. Hopkinson, G. Hill, and G.J. Rees. "Excess noise characteristics of $\text{Al}_{0.8}\text{Ga}_{0.2}\text{As}$ avalanche photodiodes." In: *IEEE Photon. Technol. Lett* 14.4 (Apr. 2002), pp. 522–524. DOI: [10.1109/68.992598](https://doi.org/10.1109/68.992598).
- [31] P. Yuan, C.C. Hansing, K.A. Anselm, C.V. Lenox, H. Nie, A.L. Holmes, B.G. Streetman, and J.C. Campbell. "Impact ionization characteristics of III-V semiconductors for a wide range of multiplication region thicknesses." In: *IEEE J. Quantum Electron.* 36 (Feb. 2000), pp. 198–204. DOI: [10.1109/3.823466](https://doi.org/10.1109/3.823466).
- [32] G.E. Bulman, V.M. Robbins, K.F. Brennan, Karl Hess, and G.E. Stillman. "Experimental determination of impact ionization coefficients in (100) GaAs." In: *IEEE Electr. Devices Lett.* 4 (June 1983), pp. 181–185. DOI: [10.1109/EDL.1983.25697](https://doi.org/10.1109/EDL.1983.25697).
- [33] M.A. Herman and H. Sitter. *Molecular Beam Epitaxy Fundamentals and Current Status*. Springer, 1996.
- [34] G. Biasiol and L. Sorba. *Molecular Beam Epitaxy: Principles and applications*. Crystal growth of materials for energy production and energy-saving applications, Edizioni ETS, Pisa, 2001, pp. 68–83.
- [35] J. Orton and T. Foxon. *Molecular Beam Epitaxy A Short History*. Oxford University Press, 2015.
- [36] M. Henini. *Molecular Beam Epitaxy From research to mass production*. Elsevier, 2012.
- [37] T. Farrell and J.V. Armstrong. "In-situ laser reflectometry of the epitaxial growth of thin semiconductor films." In: *Applied Surface Science* 86 (Feb. 1995), pp. 582–590. DOI: [10.1016/0169-4332\(94\)00388-2](https://doi.org/10.1016/0169-4332(94)00388-2).
- [38] Inc. SVT Associates. *In-Situ 4000 White Paper Solving the problems of pyrometry and thickness measurement during MBE and MOCVD*. datasheet. 2011.
- [39] Inc. SVT Associates. *In-Situ 4000 Process Monitor Measurement of GaN Growth Rate as a Function of Substrate Temperature*. datasheet. 2011.

- [40] J. Singh. *Semiconductor Optoelectronics Physics and Technology*. Springer-Verlagf Wien, 1984.
- [41] M.J. Madou. *Fundamentals of MICROFABRICATION The Science of Miniaturization*. CRC Press LLC, 2002.
- [42] Rohm and Haas Electronic Materials. *MICROPOSIT S1800 SERIES PHOTORESIST*. datasheet. 2006.
- [43] MicroChem. *LOR Lift-off resist*. datasheet. 2002.
- [44] G. Harman. *Wire Bonding in Microelectronics*. McGraw-Hill, 2010.
- [45] J. Lauter, D. Protic, A. Forster, and H. Luth. "AlGaAs/GaAs SAM-avalanche photodiode: An X-ray detector for low energy photons." In: *Nucl. Instr. and Meth. A* 356 (Mar. 1995), pp. 324–329. DOI: [10.1016/0168-9002\(94\)01237-7](https://doi.org/10.1016/0168-9002(94)01237-7).
- [46] D.L. Sato, F.J. Szalkowski, and H.P. Lee. "Uniform and delta doping of carbon in GaAs by solid-source molecular beam epitaxy using electron beam evaporation: Evidence for atomic pairing." In: *Appl. Phys. Lett.* (Dec. 1995), pp. 127–130. DOI: doi.org/10.1063/1.113323.
- [47] M. Murakami. "Development of refractory ohmic contact materials for gallium arsenide compound semiconductors." In: *Science and Technology of Advanced Materials* 3.8 (Mar. 2002), pp. 1–27. DOI: [10.1016/S1468-6996\(01\)00150-4](https://doi.org/10.1016/S1468-6996(01)00150-4).
- [48] A. Baranska, A. Szerling, P. Karbownik, K. Hejduk, M. Bugajski, A. Laszcz, K. Golaszewska-Malec, and W. Filipowski. "Ohmic contact for room-temperature AlGaAs/GaAs quantum cascade lasers (QCL)." In: *Optica Applicata* 43 (2013), pp. 5–15. DOI: [10.5277/oa130101](https://doi.org/10.5277/oa130101).
- [49] S. Mobilio, F. Boscherini, and C. Meneghini. *Synchrotron Radiation Basics, Methods and Applications*. Springer, 2015.
- [50] *BEAR beamline*. 2020. URL: <https://www.elettra.trieste.it/it/lightsources/elettra/elettra-beamlines/bear/bear.html>.
- [51] *CiPo beamline*. 2020. URL: <https://www.elettra.trieste.it/lightsources/elettra/elettra-beamlines/cipo/cipobeamline/all.html>.
- [52] *XRD2 beamline*. 2020. URL: <https://www.elettra.trieste.it/lightsources/elettra/elettra-beamlines/xrd2/xrd2-specifications/all.html>.
- [53] *XRD2 beamline*. 2020. URL: <https://www.elettra.trieste.it/elettra-beamlines/twinmic.html>.

- [54] A. Gianoncelli, G. Kourousias, L. Merolle, M. Altissimo, and A. Bianco. "Current status of the TwinMic beamline at Elettra: a soft X-ray transmission and emission microscopy station." In: *Journal of Synchrotron Radiation* 23.6 (2016), pp. 1526–1537. DOI: [10.1107/S1600577516014405](https://doi.org/10.1107/S1600577516014405).
- [55] *Millennia Vs Diode-pumped, cw Visible Laser - User's Manual*. English. Spectra-Physics The Solid-State Laser Company. Mountain View, CA, USA, Nov. 2001.
- [56] E. Ettl, M. Dierolf, K. Achterhold, C. Jud, B. Gunther, E. Braig, B. Gleich, and F. Pfeiffer. "The Munich Compact Light Source: initial performance measures." In: *J. Synchrotron Rad.* 23 (2016), pp. 1–6. DOI: [10.1107/S160057751600967X](https://doi.org/10.1107/S160057751600967X).
- [57] *AH501B 4-Channel Bipolar Picoammeter with Bias Voltage*. English. 1.1. Sincrotrone Trieste S.C.p.A. Strada Statale 14 - km 163,5 in AREA Science Park, Dec. 2011.
- [58] M. Johnson. *Photodetection and Measurements - Maximizing performance in optical systems*. McGraw-Hill, 2003.
- [59] XG Lab. *PIN list and PAD layout of the CUBE ASIC*. Version 2.3. datasheet. 2019.
- [60] Mini-Circuits. *Surface Mount Monolithic Amplifier - Gali 51+*. datasheet.
- [61] D. W. Winston.
- [62] C. Nichetti et al. "Gain and noise in GaAs/AlGaAs avalanche photodiodes with thin multiplication regions." In: *Journal of Instrumentation* 14 (Jan. 2019), pp. C01003–C01003. DOI: [10.1088/1748-0221/14/01/C01003](https://doi.org/10.1088/1748-0221/14/01/C01003).
- [63] *X-Ray Interactions With Matter*. 2020. URL: https://henke.lbl.gov/optical_constants/.
- [64] B.L. Henke, E.M. Gullikson, and J.C. Davis. *X-ray interactions: photoabsorption, scattering, transmission, and reflection at E=50-30000 eV, Z=1-92, Atomic Data and Nuclear Data Tables*. Vol. 54. 2. Lawrence Berkeley Laborator, 1993.
- [65] T. Steinhartova et al. "Influence of δ p-doping on the behaviour of GaAs/AlGaAs SAM-APDs for synchrotron radiation." In: *Journal of Instrumentation* 12 (Nov. 2017), pp. C11017–C11017. DOI: [10.1088/1748-0221/12/11/C11017](https://doi.org/10.1088/1748-0221/12/11/C11017).
- [66] K. Lau, C. Tan, B.K. Ng, K. Li, R. Tozer, J.P.R. David, and G. Rees. "Excess noise measurement in avalanche photodiodes using a transimpedance amplifier front-end." In: *Meas. Sci. and Tech.* 17 (June 2006), pp. 1941–1946. DOI: [10.1088/0957-0233/17/7/036](https://doi.org/10.1088/0957-0233/17/7/036).

- [67] G. Bertuccio, A. Pullia, J. Lauter, A. Forster, and H. Luth. "Pixel X-ray detectors in epitaxial gallium arsenide with high-energy resolution capabilities (Fano factor experimental determination)." In: *IEEE Trans. on Nucl. Sci.* 44.1 (1997), pp. 1–5. DOI: [10.1109/23.554815](https://doi.org/10.1109/23.554815).